06647-1-T

THE UNIVERSITY OF MICHIGAN

COLLEGE OF ENGINEERING
DEPARTMENT OF AERONAUTICAL AND ASTRONAUTICAL ENGINEERING
HIGH ALTITUDE ENGINEERING LABORATORY

Technical Report

Satellite Measurement of Atmospheric Structure by Stellar Refraction

F. F. FISCHBACH
M. E. GRAVES
P. B. HAYS
R. G. ROBLE

N65-29774
(ACCESSION NUMBER)
(THRU)
(CODE)
(PAGES)
(CATEGORY)
(NASA CR OR TMX OR AD NUMBER)
FACILITY FORM 602

Administered through:

April 1965

OFFICE OF RESEARCH ADMINISTRATION • ANN ARBOR

THE UNIVERSITY OF MICHIGAN

COLLEGE OF ENGINEERING
Department of Aeronautical and Astronautical Engineering
High Altitude Engineering Laboratory

Technical Report

SATELLITE MEASUREMENT OF ATMOSPHERIC
STRUCTURE BY STELLAR REFRACTION

F. F. Fischbach
M. E. Graves
P. B. Hays
R. G. Roble

ORA Project 06647

April 1965

TABLE OF CONTENTS

LIST OF FIGURES

LIST OF FIGURES (Continued)

LIST OF FIGURE (Concluded)

THE UNIVERSITY OF MICHIGAN PROJECT PERSONNEL

Both Full and Part Time

Childs, David L., B.S.E., Assistant in Research

Fischbach, Frederick F., M.S., Project Supervisor

Gallaher, Helen C., Secretary

Graves, Maurice E., S.M., Assistant Research Meteorologist

Hays, Paul B., Ph.D., Associate Research Engineer

Jones, Leslie M., B.S.E., Laboratory Director

Kuehnlein, Margie S., Secretary

Roble, Raymond G., M.S.E., Research Associate

Wescott, John W., M.S.E.E. Associate Research Engineer

ABSTRACT

2977 4

The technique for deducing atmospheric structure from satellite measure-
ments of refracted starlight is critically examined by relating errors in
pressure and temperature to equipment errors. Graphical results are presented,
enabling the evaluation of star-tracking accuracy required to meet any given
pressure or temperature accuracy. Rigorous analyses of starlight transmission
through the atmosphere and background sky brightness are reported, enabling
the calculation of star-tracker signal-to-noise ratios and completing the
specifications necessary to a design.

Occultation geometry has been revised and is presented in graphical form.
Results of a preliminary cloud cover analysis are included.

ACKNOWLEDGMENT

I. INTRODUCTION

A feasibility study of satellite measurements of starlight refraction to deduce atmospheric parameters was begun in 1961. This report is the fourth in a series which describes the progress of the study.

The first report gave a broad outline of the technique and a statement of several problem areas and suggested solutions. In the second report an attempt was made again to describe fully the technique and to include the results of all analyses made to the date of publication. The report was intended to replace the first and not to supplement it.

Shortly after the second report was printed, an analytic solution was found to the equation expressing the density function in terms of a refraction scan. This solution had such signal importance to the ultimate feasibility of the technique that it was described in a brief third report. The analytic inversion enabled a complete, definitive error analysis and an actual data-processing method to be written.

The present report gives the results of several analyses conducted since those reports. Specifically, a complete error analysis is presented, linking star-tracking accuracies with pressure and temperature errors. Also fundamental to star-tracker design is the required sensitivity, a function of signal-to-noise ratio. For this reason studies of starlight transmission and sky background intensities were made. Since clouds constitute an important limitation to the technique, a section is devoted to that problem. Occultation geometry was reexamined rigorously and some changes from the results given in the second report are noted.

Generally, the studies were undertaken to develop specifications for the spacecraft, thus reducing the question of the technique's feasibility to one of determining whether or not the engineering state-of-the-art is such that the requirements can be met. That determination will be the next focus of effort. Hopefully, a preliminary spacecraft design will emerge.

II. AN ANALYSIS OF ERRORS

One of the most vital analyses in the feasibility study is that of the propagation of errors through the data-reduction process. The result of such an error study will be the determination of the errors in the meteorological parameters, density, pressure, and temperature, as functions of the errors in the data-gathering equipment. These functions may then be used in either of two ways: knowledge of maximum acceptable errors in the meteorological parameters enables a specification of the required equipment accuracy, or knowledge of the errors in proposed equipment is sufficient to determine the errors in the meteorological parameters.

In the current study, the former approach is used: the required meteorlogical accuracies will determine equipment specifications. Feasibility of the refraction technique will then depend on the ability to meet these specifications.

Errors have been analyzed by two methods: the first method will be referred to as "theoretical," the second method as "numerical." The theoretical method involves the introduction of an error to the refraction angles which, aided by certain simplifying assumptions, can be propagated analytically to produce an error in the retrieved densities. The error in retrieved densities is also analyzed as a function of data frequency. Pressure and temperature errors as functions of density errors are also computed.

The numerical error analysis involves the simulation of actual satellite data. A set of correct refraction values for an arbitrary atmosphere is computed and subjected to a random scatter of some known standard deviation. The scattered refraction angles are fed to the data processing program, and the atmospheric densities, pressures, and temperatures computed. These computed values are then compared with the original atmosphere to obtain the errors. This process is repeated with several randomly scattered sets of refraction angles having the same standard deviation to establish an rms error.

The entire procedure is repeated for other values of standard deviation and for several data rates. Thus the output yields pressure, temperature, and density errors as functions of star-tracker error and information rate. The numerical analysis requires and uses the exact data reduction scheme.

The results of the two types of analysis may be compared, with the theoretical analysis serving as a guide to the efficacy of the numerical analysis. Since the numerical error analysis is based on the actual data-processing method to be used, it should be regarded as most important; it is not only a demonstration of how data may easily be processed in the time required, but is likewise a proof of the correctness of the inversion from refraction to the meteorological parameters.

A. THEORETICAL ERROR ANALYSIS

The basic inversion relation used to recover density from refraction angle data was given by Hays and Fischbach[8]:

$$\rho = \frac{1}{\pi k} \int_{\eta_0}^{\infty} \frac{R(\eta) \, d\eta}{(\eta^2 - \eta_0^2)^{1/2}} + O\left[\frac{k\rho^2}{2}\right] + \ldots,$$

where η is the impact parameter measured by the satellite:

$$\eta = r \sin z .$$

In the general situation the refraction angle data will be obtained as a number of discrete data points (R_i, η_i) which must be incorporated in a numerical integration scheme in order to obtain the density data. That is,

$$\rho_j = \frac{1}{\pi k} \sum_{i=j}^{\infty} f_{ij}(R) ,$$

where the functions f_{ij} depend upon the specific data reduction scheme.

Since the actual data obtained from the satellite measuring device will be in error, the densities will be in error by the amount

$$\Delta \rho_j = \frac{1}{\pi k} \left\{ \sum_{i=j}^{N} C_{ij} \Delta R_i + \sum_{i=N}^{\infty} C_{ij} R_i \right\} ,$$

where the first term represents the error due to scatter and the last term is due to truncation. The scattering of the refraction angle measurements is a result of two sources: first, the actual measurement of refraction angle is in error; second, the impact parameter η is obtained from R_i and consequently is also in error. For the purposes of the error analysis one can combine these effects in a single error in the refraction angle such that

$$\Delta R_i = \delta R_i \left(1 + \frac{\partial R_i}{\partial \eta} \frac{\partial \eta}{\partial z} \frac{\partial z}{\partial R_i}\right) \, ,$$

where δR_i is the error in the measured value of the refraction angle, and z the zenith angle.

This information can now be used statistically to determine the rms error in density resulting from a given rms instrument error. It is easily shown that

$$\overline{\Delta \rho_j^2} = \frac{1}{\pi k} \left\{ \sum_{i=j}^{N} C_{ij}^2 \overline{\Delta R_i^2} + \overline{\left(\sum_{j=N}^{\infty} C_{ij} R_i\right)^2} \right\}$$

where

$$\overline{\Delta R_i^2} = \overline{\delta R_i^2} \left(1 + \frac{\partial R_i}{\partial \eta} \frac{\partial \eta}{\partial z} \frac{\partial z}{\partial R_i}\right)^2 \, .$$

Here $\overline{\delta R_i^2}$ is the rms instrument angular error which is in general independent of η. For the situation where R_i varies exponentially, $R_i = R_o \exp\left[-(\eta_i - \eta_o)/H\right]$

$$\sqrt{\overline{\Delta R_i^2}} = \sqrt{\overline{\delta R_i^2}} \left[1 + R_i \frac{r_s}{H} (1 - \eta_i/r_s)^{1/2}\right] \, ,$$

where H is the scale height of the refraction angle and r_s the satellite distance from the center of the earth.

A.1 Computational Procedure

Since the refraction angle is a nearly exponential function one can reasonably reduce the refraction data by using an exponential approximation between points:

$$R(\eta) = R_i \exp\left[\left(\log \frac{R_{i+1}}{R_i}\right) \frac{\eta - \eta_i}{\eta_{i+1} - \eta_i}\right] \qquad \eta_i < \eta < \eta_{i+1} \, .$$

4

Thus,

$$
\rho_j = \frac{1}{\pi k} \left\{ \sum_{i=j}^{\infty} \int_{\eta_i}^{\eta_{i+1}} R_i \exp\left[\left(\log \frac{R_{i+1}}{R_i}\right) \frac{\eta - \eta_i}{\eta_{i+1} - \eta_i}\right] \left(\eta^2 - \eta_j^2\right)^{-1/2} d\eta \right\} + \ldots
$$

$$
= \frac{1}{\pi k} \left\{ \sum_{i=j}^{\infty} I_{ij} \right\} ,
$$

letting I_{ij} stand for the integral. But in the case wherein R_i is in error this can be written as the linear relation

$$
\rho_j + \Delta\rho_j = \frac{1}{\pi k} \left\{ \sum_{i=j}^{\infty} I_{ij} + \sum_{i=j}^{\infty} \left(\frac{\partial I_{ij}}{\partial R_i} \Delta R_i + \frac{\partial I_{ij}}{\partial R_{i+1}} \Delta R_{i+1} \right) + \ldots \right\},
$$

where second-order terms are neglected.

The latter portion of this relation can be written as

$$
\Delta\rho_j = \frac{1}{\pi k} \sum_{i=j}^{\infty} C_{ij} \Delta R_i ,
$$

where

$$
C_{ij} = \frac{1}{\pi k (\eta_{i+1} - \eta_i)} \left\{ \frac{\sqrt{\pi}\, e^{-\alpha_i(\eta_j - \eta_i)}}{[\alpha_i(\eta_i + \eta_j)]^{1/2}} \left(\eta_{i+1} - \eta_j - \frac{1}{2\alpha_i} \right) \left[\operatorname{erf}\left[\alpha_i(\eta_{i+1} - \eta_j)\right]^{1/2} \right. \right.
$$

$$
\left. \left. - \operatorname{erf}\left[\alpha_i(\eta_i - \eta_j)\right]^{1/2} \right] + \frac{R_{i+1}}{\alpha_i R_i} \left(\frac{\eta_{i+1} - \eta_j}{\eta_i + \eta_j} \right)^{1/2} - \frac{1}{\alpha_i} \left(\frac{\eta_i - \eta_j}{\eta_i + \eta_j} \right)^{1/2} \right\}
$$

$$+ \frac{1-\delta_{ij}}{\pi k(\eta_i - \eta_{i-1})} \left\{ \frac{\sqrt{\pi}\left(\frac{R_{i-1}}{R_i}\right) e^{-\alpha_{i-1}(\eta_j - \eta_{i-1})}}{[\alpha_{i-1}(\eta_{i-1}+\eta_j)]^{1/2}} \left(\frac{1}{2\alpha_{i-1}} + \eta_j - \eta_{i-1}\right) \cdot \right.$$

$$\left[\text{erf } [\alpha_{i-1}(\eta_i - \eta_j)]^{1/2} - \text{erf } [\alpha_{i-1}(\eta_{i-1}-\eta_j)]^{1/2} \right] + \left(\frac{R_{i-1}}{R_i}\right)\frac{1}{\alpha_{i-1}}\left(\frac{\eta_{i-1}-\eta_j}{\eta_{i-1}+\eta_j}\right)^{1/2}$$

$$\left. - \frac{1}{\alpha_{i-1}}\left(\frac{\eta_i - \eta_j}{\eta_{i-1}-\eta_j}\right)^{1/2} \right\} .$$

where $\text{erf }(x) = \frac{2}{\sqrt{\pi}} \int_0^x e^{-t^2} dt$ and δ_{ij} is the Kronecker Delta Function.

A.2 Pressure and Temperature

The pressure and temperature are determined directly from the density data, and thus an estimation of the rms error for these quantities is easily determined. Pressure is obtained by direct integration of the hydrostatic equation

$$P = \int_h^{h_m} g \, \rho \, dh + P_m \; ;$$

g = gravity,

h_m = height of topmost point,

P_m = pressure at topmost point,

which can be written for numerical analysis as

$$P_k = \sum_{j=k}^{m} D_{jk} \, \rho_j + P_m .$$

The same procedure used in the last section may now be employed to obtain values for D_{jk}. For an atmosphere in which ρ varies nearly exponentially, one can interpolate between data points by the exponential expression

$$g \, \rho(h) = g_i \rho_i \exp \left[-\log \frac{g_{i+1} \, \rho_{i+1}}{g_i \, \rho_i} \frac{h-h_i}{h_{i+1}-h_i} \right] .$$

Introducing this relation into the hydrostatic equation and neglecting second-order quantities gives

$$\Delta P_k = \sum_{j=k}^{m} D_{jk}\,\Delta\rho_j + \Delta P_m \quad,$$

where

$$D_{jk} = \frac{1}{\rho_j}\left\{\left[\frac{h_j-h_{j-1}}{\log\left(\frac{g_i\,\rho_j}{g_{j-1}\rho_{j-1}}\right)}g_j\rho_j - \frac{h_j-h_{j-1}}{\left[\log\left(\frac{g_j\rho_j}{g_{j-1}\rho_{j-1}}\right)\right]^2}(g_j\rho_j - g_{j-1}\rho_{j-1})\right](1-\delta_{jk})\right.$$

$$\left. -\left[\frac{h_{j+1}-h_j}{\log\left(\frac{g_{j+1}\,\rho_{j+1}}{g_j\,\rho_j}\right)}g_j\,\rho_j - \frac{h_{j+1}-h_j}{\left[\log\left(\frac{g_{j+1}\,\rho_{j+1}}{g_j\,\rho_j}\right)\right]^2}(g_{j+1}\rho_{j+1}-g_j\,\rho_j)\right](1-\delta_{jN})\right\}$$

Finally, since the temperature is related to density and pressure through the equation of state, one can write

$$T_\ell = \frac{P_\ell}{R\rho_\ell} \quad,$$

and for small errors

$$\frac{\Delta T_\ell}{T_\ell} = \frac{\Delta P_\ell}{P_\ell} - \frac{\Delta\rho_\ell}{\rho_\ell} = \sum_{j=\ell}^{m}\left(\frac{D_{j\ell}}{P_\ell} - \frac{\delta_{j\ell}}{\rho_\ell}\right)\Delta\rho + \frac{\Delta P_m}{P_\ell}$$

Notice that either a value for P or T may be chosen at the topmost point, since the density is known, and thus

$$P_m = \rho_m R T_m \quad.$$

7

B. NUMERICAL ERROR ANALYSIS

The numerical error analysis consists first of selecting an arbitrary atmosphere and calculating precisely the refraction angles which would be measured by a satellite star-tracker during an occultation. Random errors of specified standard deviations are introduced into the angles, simulating the random errors to be encountered in the actual data. These data are then processed by the computerized data-reduction program which primarily is a quadrature of the integral equation inverting refraction angles to densities. The program calculates pressures and temperatures as well as densities. (The error due to initial pressure or temperature is independent and added later.) To obtain the error, the retrieved pressures, temperatures, and densities are compared with the arbitrary atmosphere.

In order to specify a meaningful rms error, several sets of randomly scattered refraction angles are used for each set of parameters. Two parameters are varied: the standard deviation of angular errors, and the height interval between refraction angles, i.e., data frequency.

The rms errors obtained in this manner have special significance because they represent errors in measurements actually obtained by an operational data-processing scheme. Moreover, the computations are carried out in less time than the simulated occultations would require, a necessity for an operational method.

B.1 Selecting an Arbitrary Atmosphere

Typical atmospheric models are designed to give average conditions, usually with temperature gradient discontinuities, and do not attempt to represent the real atmosphere at any given instant. We have chosen therefore to work with the analytic model atmosphere of Ref. 10, which is based on a continuous density function, and perhaps resembles more closely the atmosphere at some given time and place. (The "correctness" of the model is not an issue; any arbitrary choice would suffice.) Several difficulties arise in its use, however, most important of which is lack of precision, the tabular values being given to only four places. We therefore use as our standard, or input arbitrary atmosphere, values derived as follows:

Density.

The model atmosphere tabular values of "$\log_{10}\rho$," given at 2-km intervals from 0 to 90 km and at 4-, 2-, 4-km intervals (94, 96, 100, 104, 106, 110, etc.) from 90 to 200 km to four significant figures, are assumed exact. For

intermediate values, the IBM 7090 was used to carry out a fifth-order Lagrangian interpolation with these results considered exact. The actual standard, then, is $\log_{10}\rho$, and exponentiation is required to obtain density.

Pressure.

After obtaining exact values of density as described above at 0.1-km intervals from 0 to 200 km, the pressure "standard" is obtained by integration downward at 0.1-km intervals, with an assumed exact pressure of 1.3600×10^{-3} dynes/cm^2 at 200 km. The quadrature used is:

$$\int_{h_1-.1}^{h_1} \rho(h)g(h)dh \simeq .1 \frac{\left[\rho(h_1)g(h_1) - \rho(h_1-.1)g(h_1-.1)\right]}{\ln\left[\rho(h_1)g(h_1)\right] - \ln\left[\rho(h_1-.1)g(h_1-.1)\right]}$$

$$P(h) = P(200) + \int_{h}^{200} \rho(h)g(h)dh$$

Gravity is assumed exactly $g(h) - 9.80665\left(\dfrac{6371}{6371 + h}\right)^2$ m/sec^2. For intermediate values the IBM 7090 subroutine with fifth-order interpolation, is considered exact.

Temperature.

The "standard" for temperature is obtained at any altitude from the density and pressure standards.

$$T = \frac{P}{\rho} \times \frac{M}{R} \quad ,$$

where M is the molecular weight and R the universal gas constant. M is ordinarily considered to vary with altitude above 90 km. If M is treated as a constant, then the derived temperatures are called molecular-scale temperatures. They will be identical with kinetic temperatures below 90 km. Since our technique will never yield temperatures above this altitude, we chose M = 28.966 and used molecular scale temperature throughout, referring only to "temperature." The units employed are grams/cm^3, dynes/cm^2, and °K, thus:

$$T = P/\rho \times 3.4833 \times 10^{-7} \; .$$

The foregoing constitutes the standard arbitrary atmosphere which will be the input to the error analysis scheme. It is intended to be representative of conditions on some mid-latitude night.

B.2 Calculation of Refraction Angle

Given the arbitrary atmosphere above, the next step is to calculate the exact refraction angle of a star's light ray which passes horizontally through the atmosphere and is tangent to it at a height, h, above the surface.

The refraction computation is done on an IBM 7090 computer and is accurate to five significant figures.

To economize in the computation of refraction angle, which is expensive due to the small integration steps required for precision, the computation will be limited to every 1/2 km of tangent ray height. For intermediate points the IBM 7090 subroutine with fifth-order interpolation is used. The accuracy of this interpolation was checked by comparison with the integration at several points and was identical to within .002%.

B.3 Introduction of Error

Our technique is presumed to utilize a star-tracker which basically measures refraction angle as a function of time. Time errors can be made equivalent to refraction angle errors; thus refraction angle errors alone may be used to specify precision. Equally important, in star-tracking as well as in data reduction, is the frequency with which refraction can be measured. Generally speaking, in star-tracker design a trade-off between accuracy and frequency of observation may be made.

Thus our error analysis consists of varying two parameters: the rms value of refraction angle error, and the frequency of measurement. Additionally, several different randomly scattered scans are required for every case in order to show the error bandwidth, rather than the error in a single retrieval, which might be unusually large or small.

We then take the correct interpolated values of refraction angle and subject them to a Gaussian scatter in which the standard deviation may be specified. These sets of refraction angles constitute the simulated data.

B.4 Retrieval of Atmospheric Parameters

While the error analysis proper consists of a variation in standard deviation of scattered refraction angles, a variation of refraction angle frequency, each with a number of random scans to determine the error bandwidth, several determinations must be made within the retrieval program, some of which

also require a variation of parameters.

Of these, the first is determination of integration interval size. After testing the errors with various amounts of scatter, various refraction angle data frequencies, and varying integration intervals, we concluded that the interval should be approximately the size of the input refraction angle intervals. Smaller intervals become expensive with virtually no improvement in accuracy; larger intervals cause loss of precision.

Second is a determination of the character of the refraction angle scatter to be introduced. A Gaussian scatter was chosen and modified such that any point in error more than 3-sigma was rejected and another point selected to replace it. This is a more severe criterion than Chauvenet's, for example, but one in keeping with the physical situation actually involved.

Third, again regarding the scattered refraction angle input data, a determination must be made of the initial, or upper, altitude. It is manifestly uneconomical to allow the star-tracker to dwell on a star long before significant refraction begins. Yet at whatever altitude we choose to begin the refraction scan, some refractive atmosphere lies above and will be neglected, thus making our computed densities slightly low.

Fourth, consider scattered refraction angles. If the standard deviation of scatter is 4 arc-seconds, say, and we are observing a ray with tangent height of about 50 km where refraction equals 3 arc-seconds, our data will contain several negative refraction angles. Our retrieval program is not prepared to cope with them; therefore, we arbitrarily change their value to zero. This introduces a slight positive error into the computed densities.

Since our third problem, truncation of the data, introduces a slight negative skew to the densities, and the fourth problem, negative refraction angles changed to zero, introduces a slight positive skew to the densities, our technique is to pit these two effects against each other and attempt to make them cancel. To accomplish this, several random scans were retrieved in which the parameter, QM, was varied: QM is the number of refraction angles, reading upward in the scan, which are negative prior to truncation. Thus when QM = 0, truncation occurs at the first negative refraction angle; hence none is changed to zero and a considerable portion of the refraction is truncated giving a negative skew. When QM is greater than the number of negative refraction angles in the entire scan carried to extreme altitudes (200 km for our cases), then all negatives become 0, the truncated portion is entirely negligible, and a positive skew is realized. These two limiting cases were tested, as well as several values in between with various amounts of scatter. The optimum value of QM appeared to be about 6 for the several scans tested. However, the most important result was the fact that at 40 km and below, the entire band bounded by the limiting values of QM was considerably smaller than the band caused only by randomness of the scans with all parameters equal. This is taken as proof that the choice of QM is essentially unimportant; hence QM = 6 is to be used without concern.

11
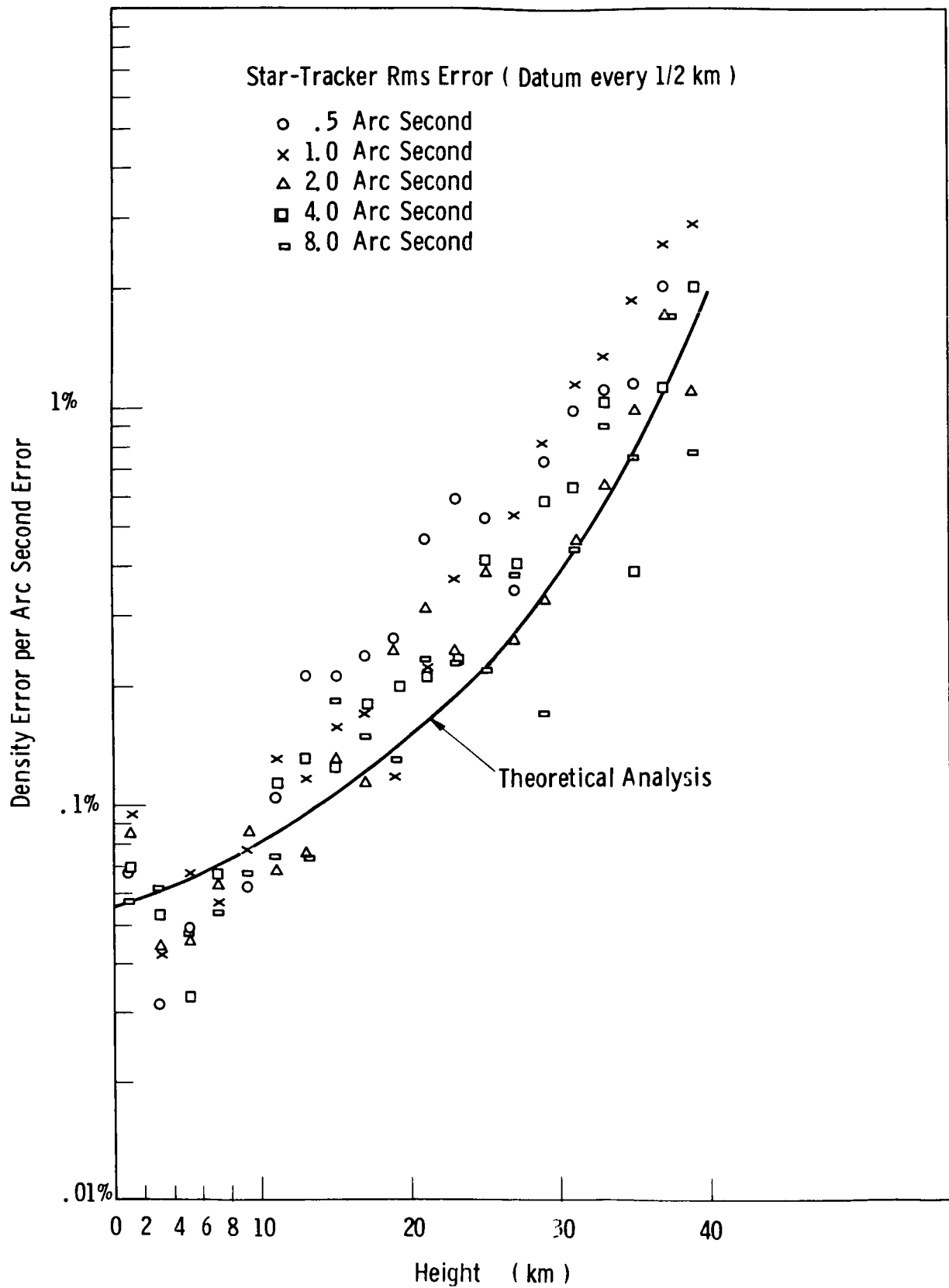
Fig. 1 Density error due to star-tracker error.
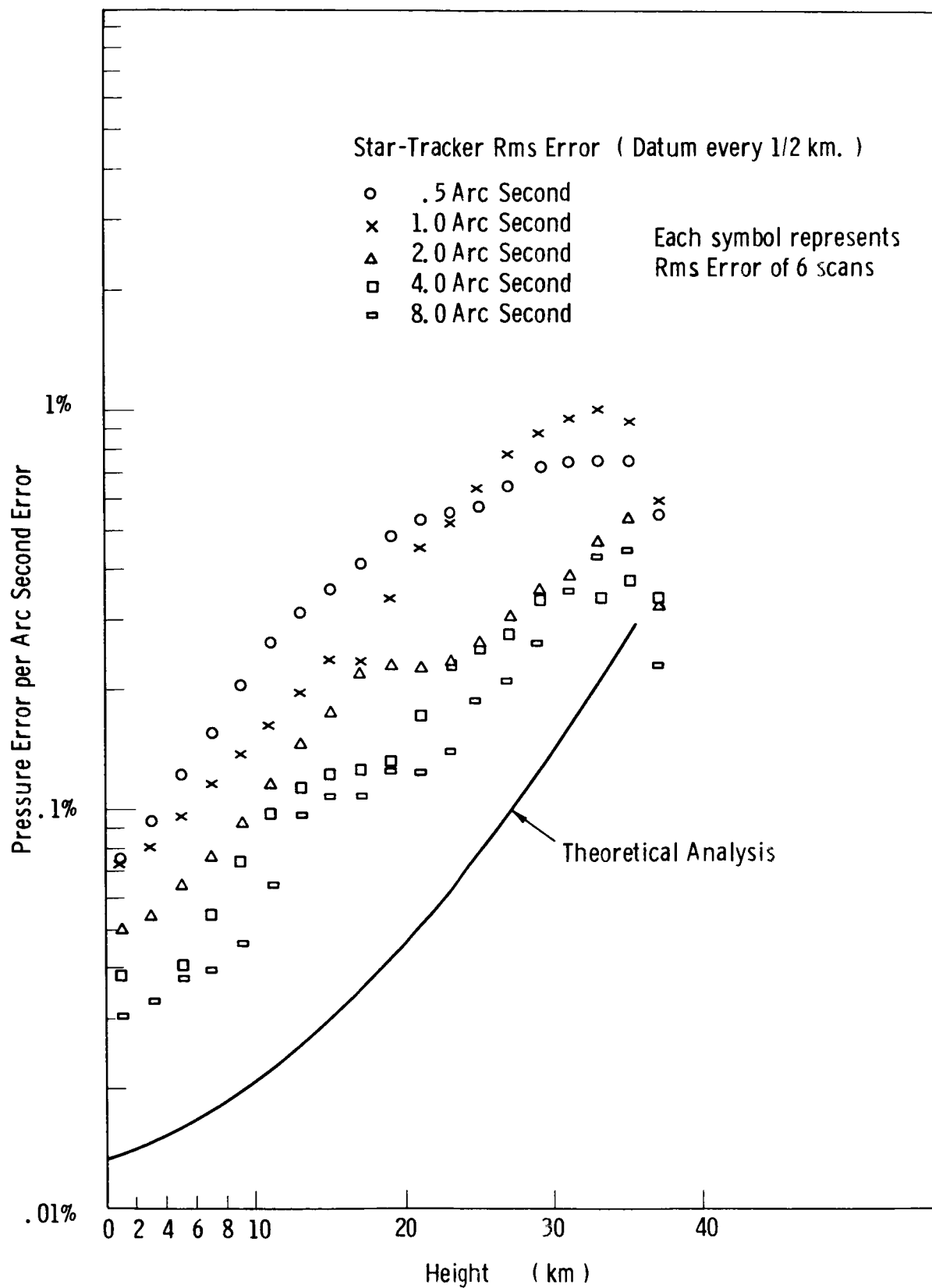
Fig. 2   Pressure error due to star-tracker error.
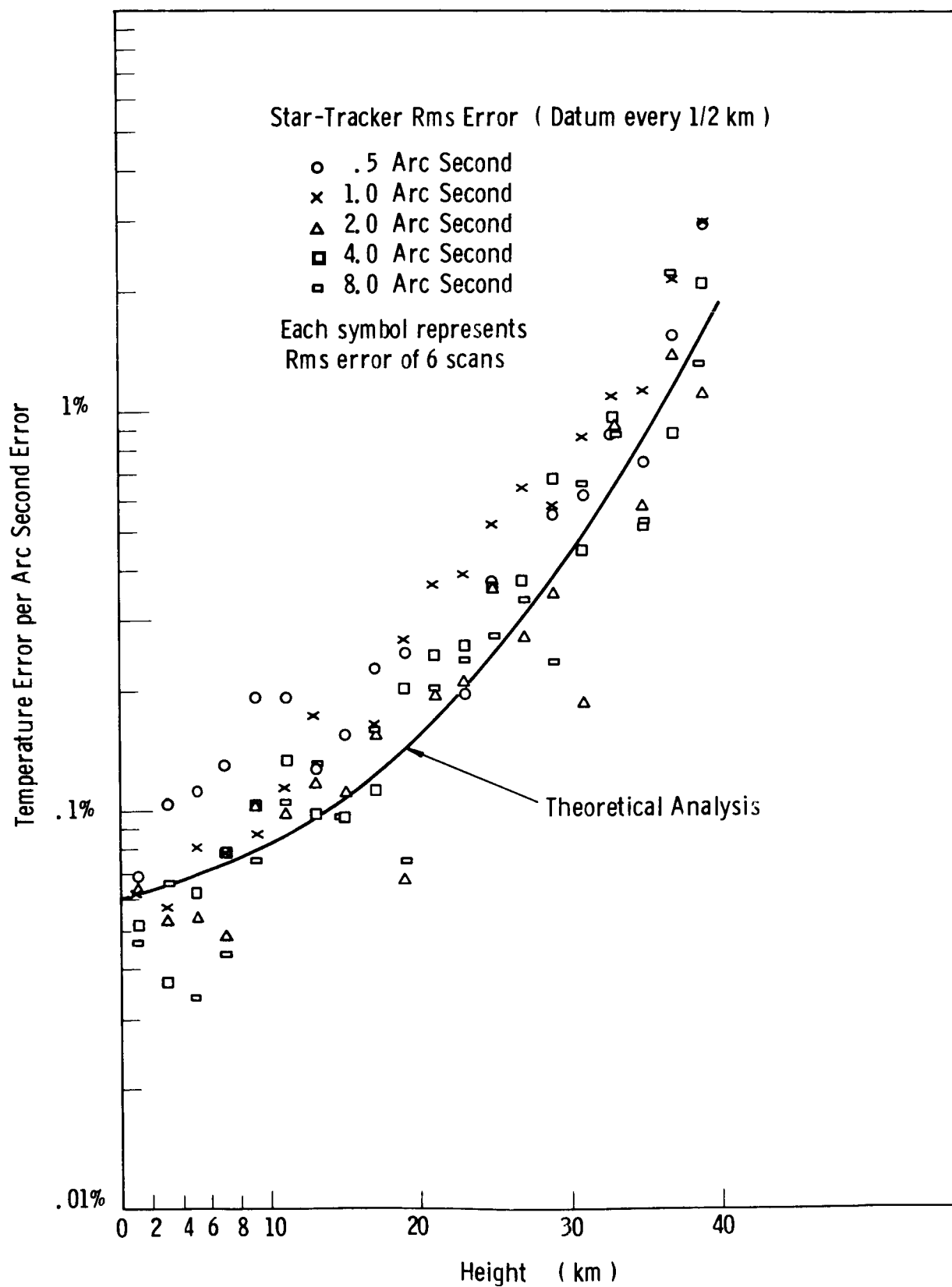
Fig. 3 Temperature error due to star-tracker error.
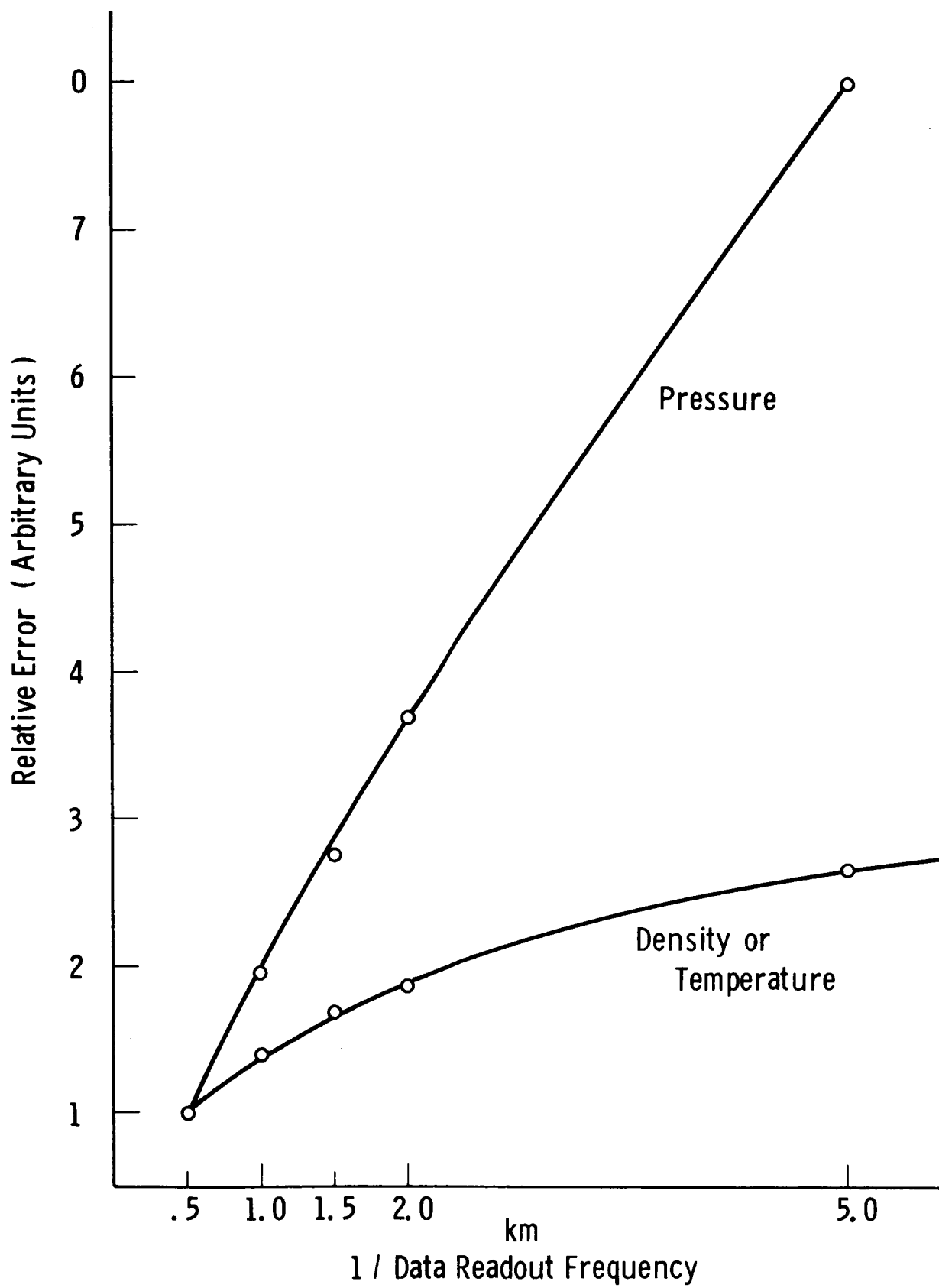
Fig. 4 Effect of data readout frequency on errors due to star-tracker.
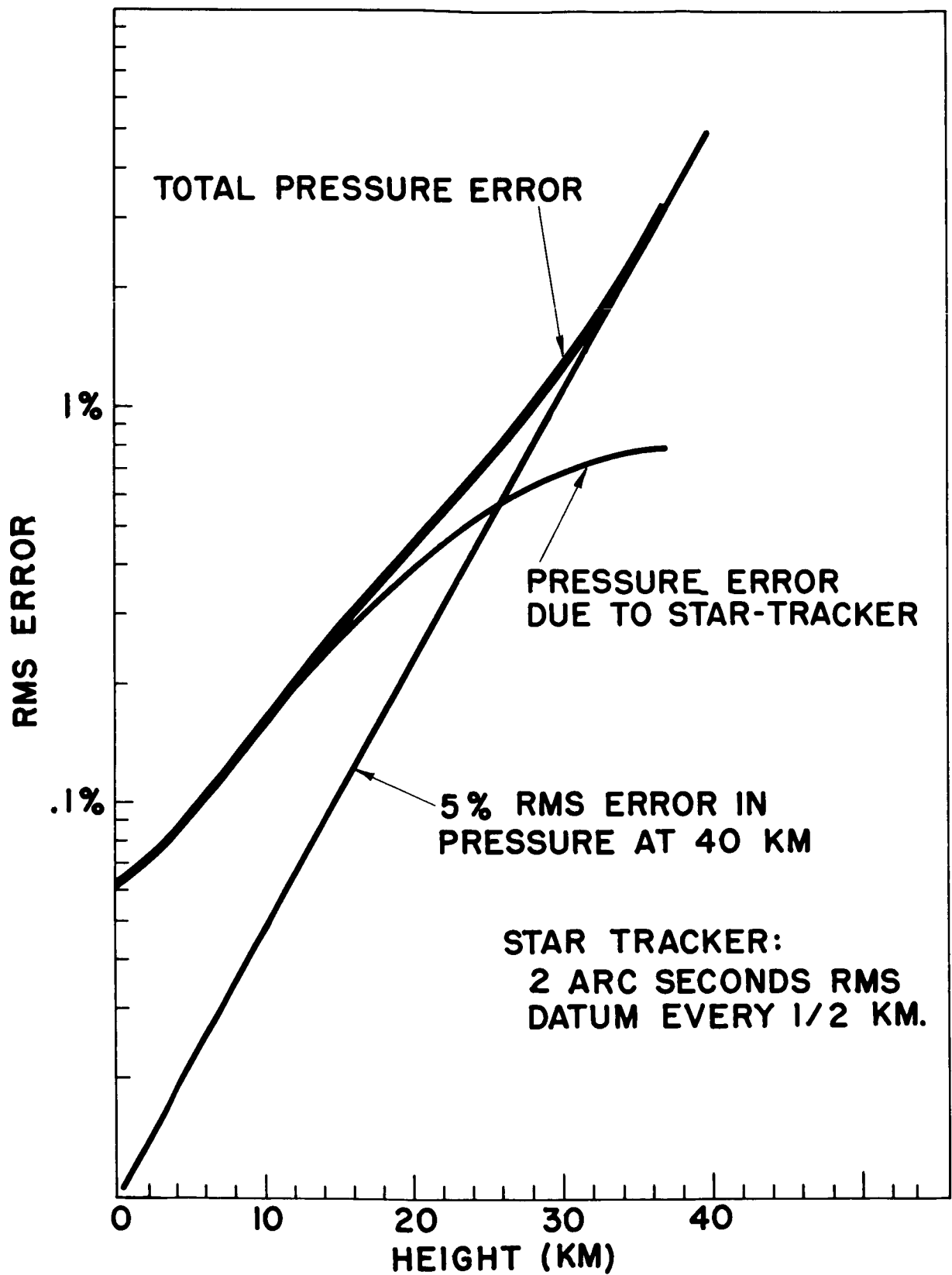
Fig. 5 Total pressure error for 2-arc-second star-tracker.
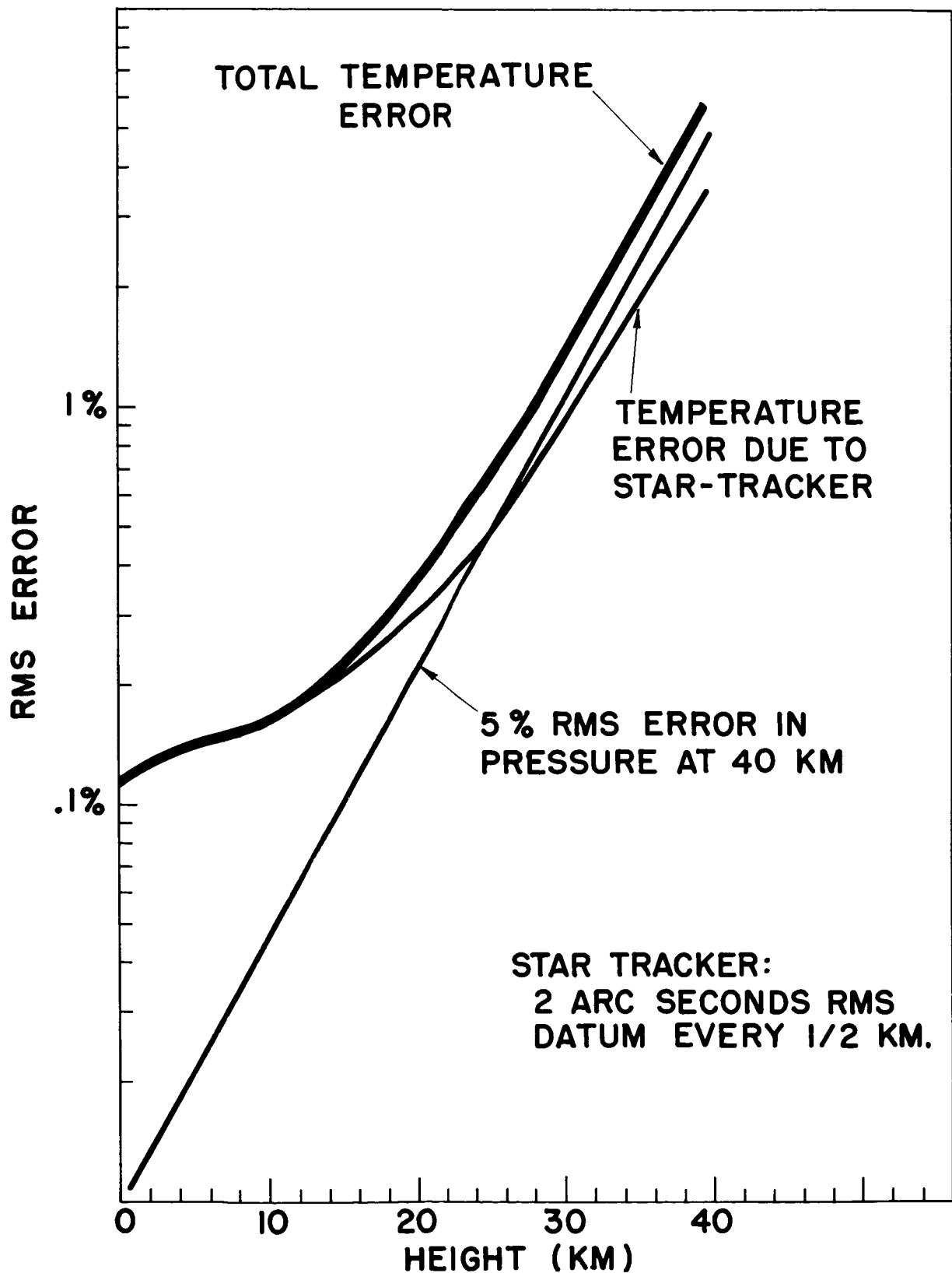
Fig. 6 Total temperature error for 2-arc-second star-tracker.

The figure contains the following labels:

TOTAL TEMPERATURE ERROR

TEMPERATURE ERROR DUE TO STAR-TRACKER

5 % RMS ERROR IN PRESSURE AT 40 KM

STAR TRACKER: 2 ARC SECONDS RMS DATUM EVERY 1/2 KM.

RMS ERROR

1 %

.1%

HEIGHT (KM)

0   10   20   30   40
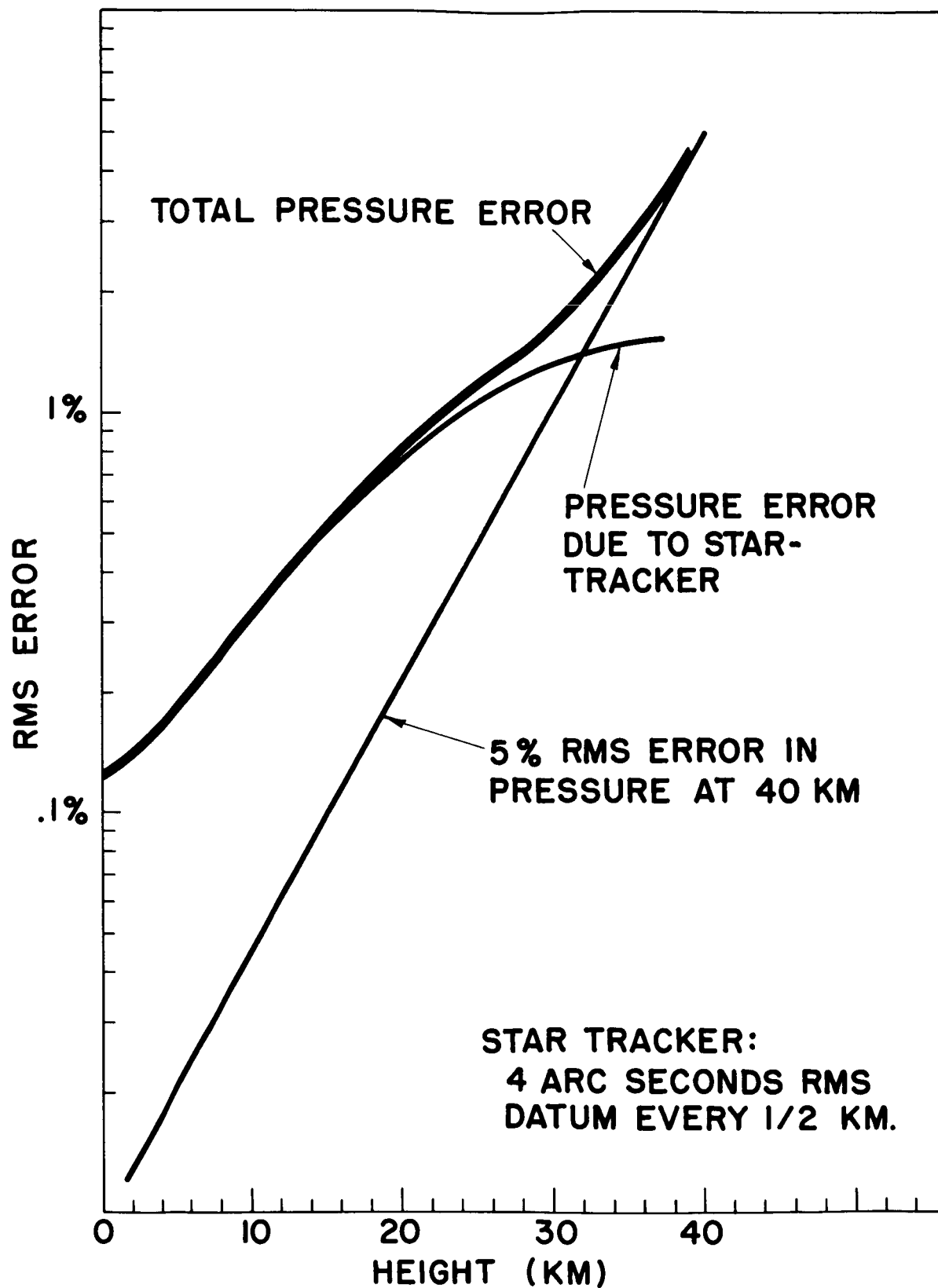
Fig. 7 Total pressure error for 4-arc-second star-tracker.
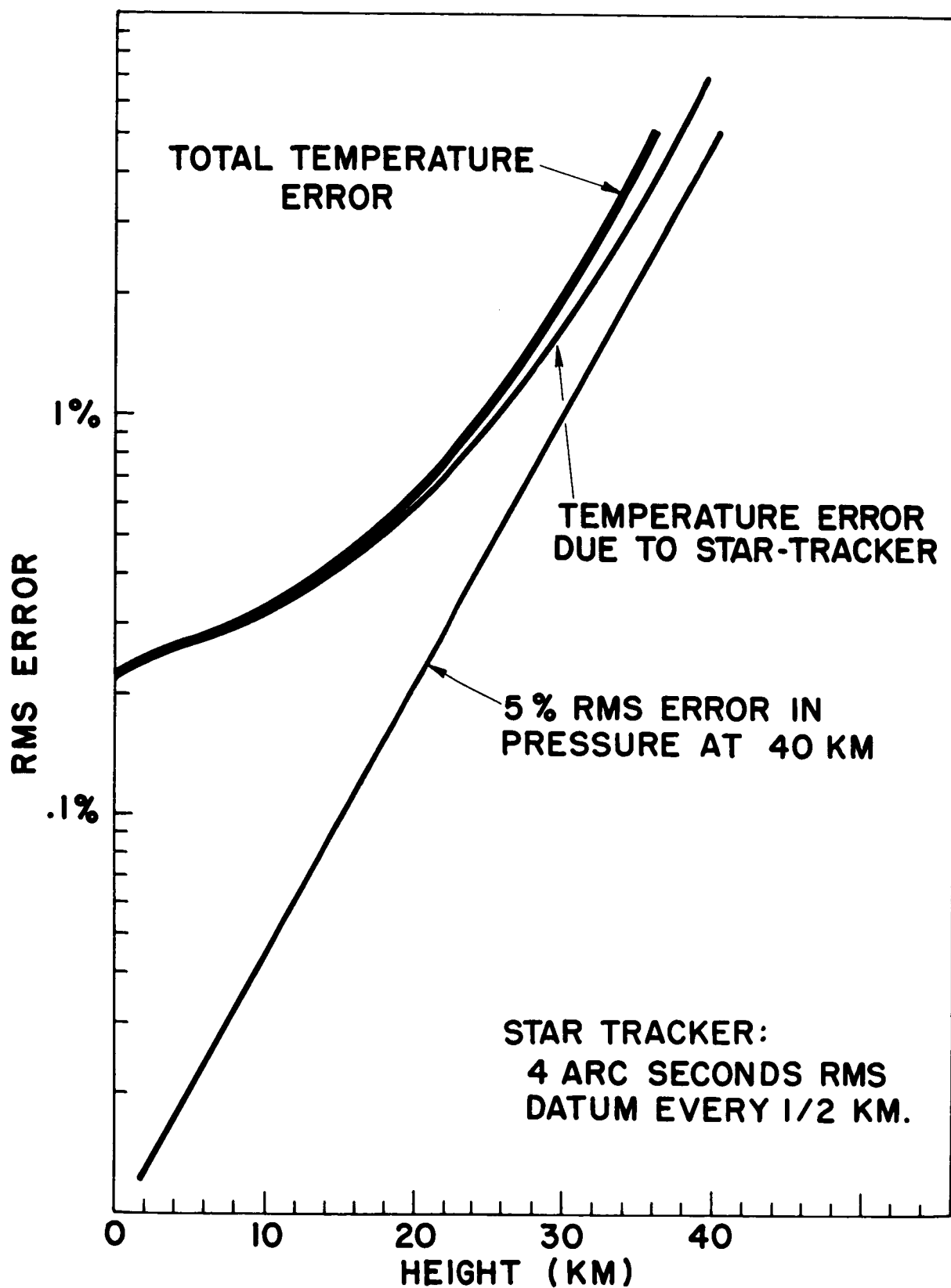
Fig. 8 Total temperature error for 4-arc-second star-tracker.

Fifth, after densities are obtained, a choice of altitude to begin pressure integration must be made. Here, our procedure entails an estimate of pressure at the initial altitude and the use of calculated densities to integrate downwards. The initial error is soon overcome by the exponentially increasing pressure. However, if density data are badly scattered at the upper end, it is better to begin by estimating pressure at a lower altitude. Experience indicates the optimum initial point, which varies somewhat with different amounts of scatter.

C. RESULTS

The results of both analyses are shown in Fig. 1-8. Figures 1, 2, and 3 show the results of the numerical analysis, with each symbol representing the rms error of 6 scans. The errors have been normalized to one arc-second rms star-tracking error. The mixing of the symbols in Fig. 1 and 3 shows the linearity of errors with rms star-tracking errors. While some nonlinearity exists in the pressure results of Fig. 2 (evidenced by the lines of symbols of the same type), as a general statement we may conclude that: In the range from .5 to 8 arc-seconds, the errors in pressure, temperature, and density are proportional to the rms tracking error; the magnitude of these errors is strongly dependent on height and corresponds closely with the theoretical results in density and temperature, but not so closely with results in pressure.

Figure 4 shows the effect of variations in data rate. Errors in density and temperature vary as the square root of the distance between observations, while errors in pressure vary directly with this distance. The results in Fig. 4 are from the theoretical analysis.

Figures 5 through 8 show the errors in pressure and temperature which would result with star-trackers of 2- and 4-arc-seconds rms error. The error in initial pressure estimation at 40 km is assumed to be 5% rms and is shown along with the error due to star-tracker error. The root-mean-square sum of these two errors then represents the total error of the system (excluding the height error associated with satellite tracking, which is considered elsewhere). Figures 5 through 8 are based on the actual results of data reduction, and not on the theoretical analysis, which would have reduced the pressure errors considerably.

III. AN ANALYSIS OF EXTINCTION EFFECTS

A. ISOTHERMAL ATMOSPHERE

The atmospheric extinction of stellar radiation by an isothermal atmosphere, and the resulting image energy distribution on a photocathode in an orbiting satellite, was examined for various tangent ray heights during occultation. Several factors contribute to the overall effect of extinction, namely, atmospheric dispersion due to differential refraction, molecular scattering, ozone absorption, Mie scattering, and water vapor scattering. In this analysis, only differential refraction, molecular scattering, and ozone absorption for an assumed ozone distribution are considered; Mie scattering and water vapor scattering are deferred until more data concerning their distribution can be obtained. In addition, the effect of star type, visual magnitude, and photocathode material characteristics are considered in order to examine the energy distribution on the photocathode image.

The geometry of a refracted ray is shown in Fig. 9. From the Dale and Gladstone Law, the density is related to the refractive index of air by

$$\mu - 1 = k\rho \; ; \tag{1}$$

k is a constant which depends upon wavelength alone and can be expressed by

$$k = \left[77.6 + \frac{0.584}{\lambda^2} \right] R \; , \tag{2}$$

where R = universal gas constant

$$= 2.8706 \; \frac{\text{millibar} - \text{m}^3}{\text{kg} - {}^\circ\text{K}}$$

λ = wavelength in microns.

Reference 1 shows that the refraction angle R_s of a ray of wavelength λ_0 passing through an isothermal atmosphere to an orbiting satellite with a tangent ray height of h_0 can be approximated by the relation

$$R_s = 2k_0\rho_b e^{-h_0/H} \sqrt{\frac{\pi(r_e + h_0)}{2H}} \; , \tag{3}$$

where ρ_b = density at ground level, (kg/m³),

H = Scale Height of the isothermal atmosphere (km),

r_e = radius of the earth, 6371 km.

The angle Θ in Figure 9 can be represented from the geometry by

$$\Theta = \frac{\pi}{2} + R_s - \sin^{-1}\left[\frac{r_e + h_o + b}{r_s} \cdot \cos R_s/2\right] ,$$

and $\qquad\qquad\qquad\qquad\qquad\qquad\qquad\qquad\qquad\qquad$ (4)

$$b = \frac{(r_e + h_o)\mu_o}{\cos R_s/2} - (r_e + h_o) ,$$

as shown in Ref. 2. Θ can further be reduced to yield

$$\Theta = \frac{\pi}{2} + R_s - \sin^{-1}\left[\frac{(r_e + h_o)(k_o \rho_o + 1)}{r_s}\right] , \qquad (5)$$

where

$\rho_o = \rho_b e^{-h_o/H}$, density at tangent ray height, h_o, for an isothermal atmosphere (kg/m³),

μ_o = index of refraction at tangent ray height,

r_s = orbital radius of the satellite (km).

To measure the dispersion of stellar radiation for an image appearing at the satellite, one must measure the change in refraction angle as a function of wavelength. The variation of refraction angle with wavelength and tangent ray height is shown in Fig. 10. Each beam incident upon the satellite is composed of a pencil covering a range of tangent heights within the atmosphere rather than a single tangent ray height. Rays of short wavelength will have a higher tangent ray height, h_{o1}, since they experience a greater refraction than rays of longer wavelength. If some intermediate wavelength is chosen as the standard, say λ_o, corresponding to a tangent ray height h_o, then rays of longer wavelength will have a lower tangent ray height, and the opposite holds for rays of shorter wavelength. The height spread can be controlled by selecting a proper wavelength band in measuring the amount of stellar refraction, thereby giving the density over a narrow tangency range.
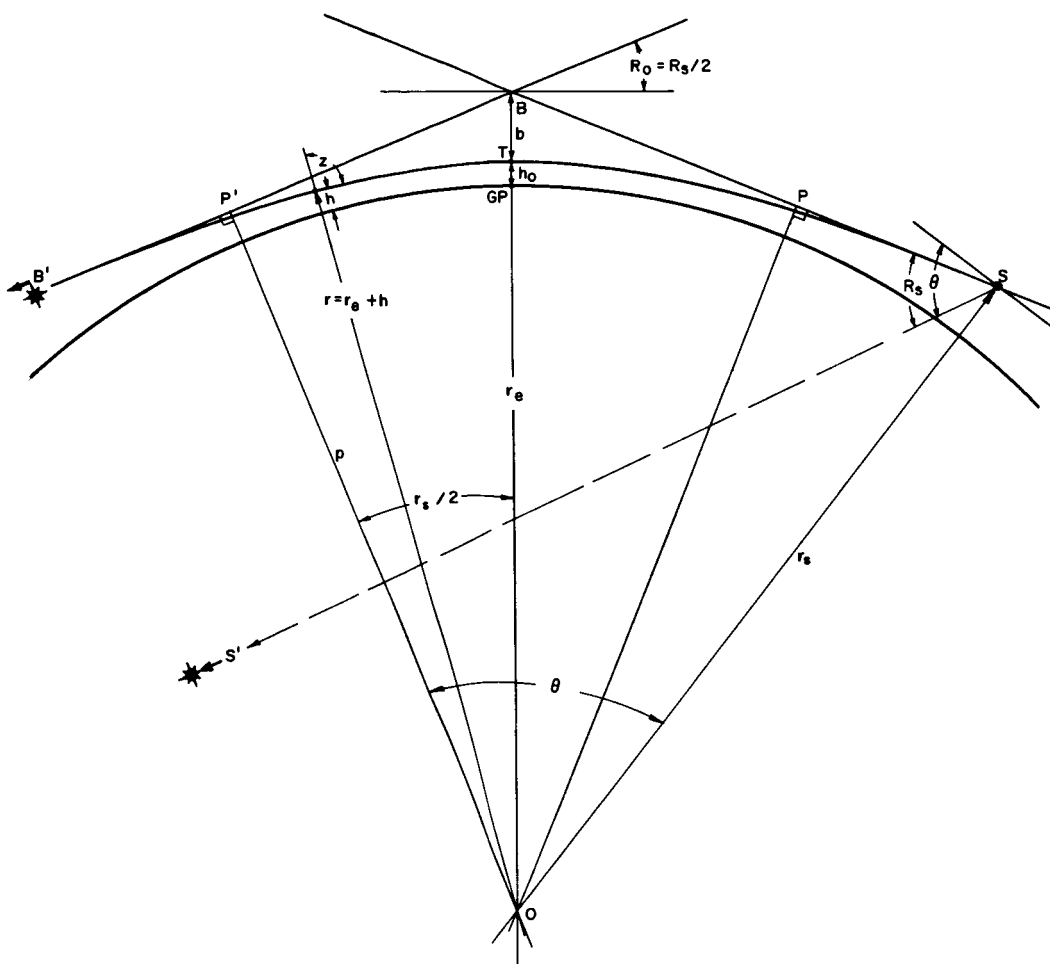
Fig. 9 Geometry of refraction.

$$\lambda_1 < \lambda_0 < \lambda_2$$

h_0 = Ray Tangency Height
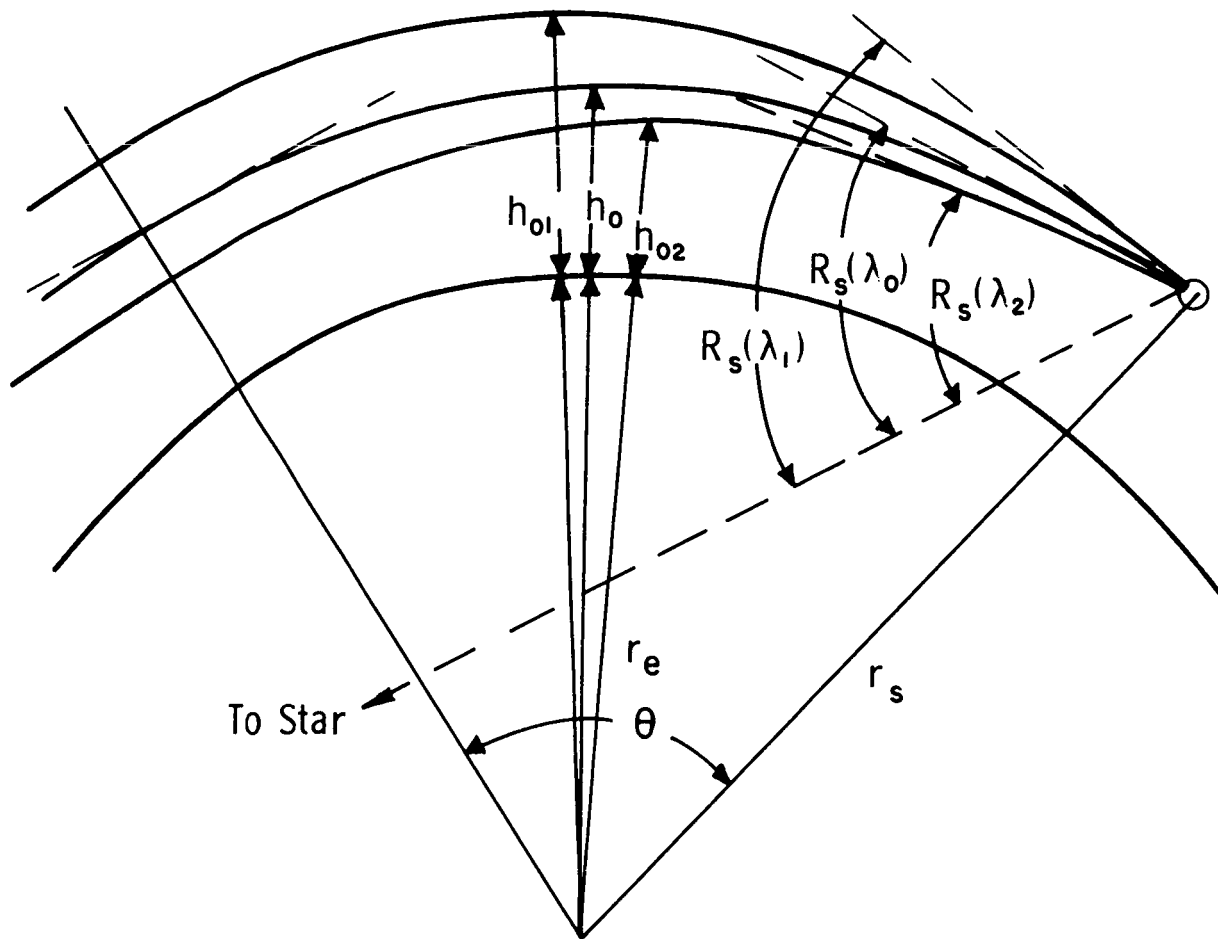
Fig. 10. Variation of refraction angle and ray height for rays of different wavelength incident upon an orbiting satellite (constant Θ).

The variation of refraction angle as a function of wavelength of rays incident upon the orbiting satellite may be obtained by an expansion about the point, h_0, for a constant Θ as,

$$R_S(k,h) = R_S(k_0,h_0) + \left.\frac{\partial R_S}{\partial k}\right|_\Theta \Delta k + \dots , \tag{6}$$

neglecting higher order terms. Since $R_S = f(k,h)$, and $\Theta = g(k,h)$, the derivative $(\partial R_S)/(\partial k)/_\Theta$ is a derivative of implicit functions and can be expressed as

$$\left.\frac{\partial R_S}{\partial k}\right|_\Theta = \left.\frac{\partial R_S}{\partial k}\right|_h - \left.\frac{\partial R_S}{\partial h}\right|_k \cdot \frac{\partial\Theta/\partial k|_h}{\partial\Theta/\partial h|_k} ; \tag{7}$$

and for an isothermal atmosphere this can be expressed analytically as

$$\left.\frac{\partial R_S}{\partial k}\right|_\Theta = 2\rho_0 \sqrt{\frac{\pi r_0}{2H}} - \frac{2\pi k_0 \rho_0}{H}\left[\frac{H-2r_0}{\sqrt{8\pi r_0 H}}\right] .$$

$$\frac{2\rho_0 \sqrt{\dfrac{\pi r_0}{2H}} - \dfrac{r_0 \rho_0}{\sqrt{r_s^2 - [r_0(k_0\rho_0+1)]^2}}}{\dfrac{2k_0 \pi\rho_0}{H}\left[\dfrac{H-2r_0}{\sqrt{8\pi r_0 H}}\right] - \dfrac{k_0\rho_0 + 1 - \dfrac{r_0 k_0 \rho_0}{H}}{\sqrt{r_s^2 - [r_0(k_0\rho_0+1)]^2}}} \tag{8}$$

Therefore, by substituting Eqs. (3) and (8) into Eq. (6) the amount of dispersion can be measured in terms of the variation of refraction angle as a function of wavelength.

25

To examine the character of the radiation coming through the atmosphere, one must determine the distribution of energy over the image formed by differential refraction. The energy distribution can be determined by examining the stellar radiation characteristics and the various extinction processes as a function of wavelength and relating the energy at a given wavelength to the refraction angle at that wavelength, thereby giving the image which would be formed by an ideal sensor located on an orbiting satellite. The output characteristics of an non-ideal phototube will be examined later. Since the extinction processes are differential refraction, molecular scattering, and ozone absorption, and the intensity of incoming radiation is dependent upon the type of star being considered and its visual magnitude, each effect will be examined separately and then combined to give the integrated effect.

From the geometry shown in Fig. 11, the intensity reduction of stellar radiation due to differential refraction can be expressed as

$$\frac{I}{I_o} = \frac{dA_o}{dA_1} \left(\frac{r}{y}\right) \frac{d_r}{d_y} = \psi = \frac{1}{(1 - D\, \partial R_s/\partial h)(1 - D\, \frac{R_s}{r})} \quad , \qquad (9)$$

where $D = r_s \sin \theta$ (as seen from Figure 9)

$$\left(1 - D\, \frac{R_s}{r}\right) \sim 1.0; \quad \frac{DR_s}{r} \ll 1.; \quad r \stackrel{\sim}{=} r_e \quad .$$

For an isothermal atmosphere, the intensity reduction due to differential refraction can be expressed as

$$\frac{I}{I_o} = \psi(k_o, h_o) \cong \frac{1}{\left[1 + \frac{D}{H} \sqrt{\frac{2\pi r_o}{H}} \cdot k_o \rho_o\right]} \quad . \qquad (10)$$

An expansion similar to that used for the refraction angle may be obtained for the intensity reduction due to differential refraction as a function of the wavelength and is

$$\psi(k, h) = \psi(k_o, h_o) + \left.\frac{\partial \psi}{\partial k}\right|_\theta \Delta k + \dots \quad . \qquad (11)$$

Likewise, since $\psi = h(k, h)$ and $\theta = g(k, h)$, the derivative again involves implicit functions and can be represented as
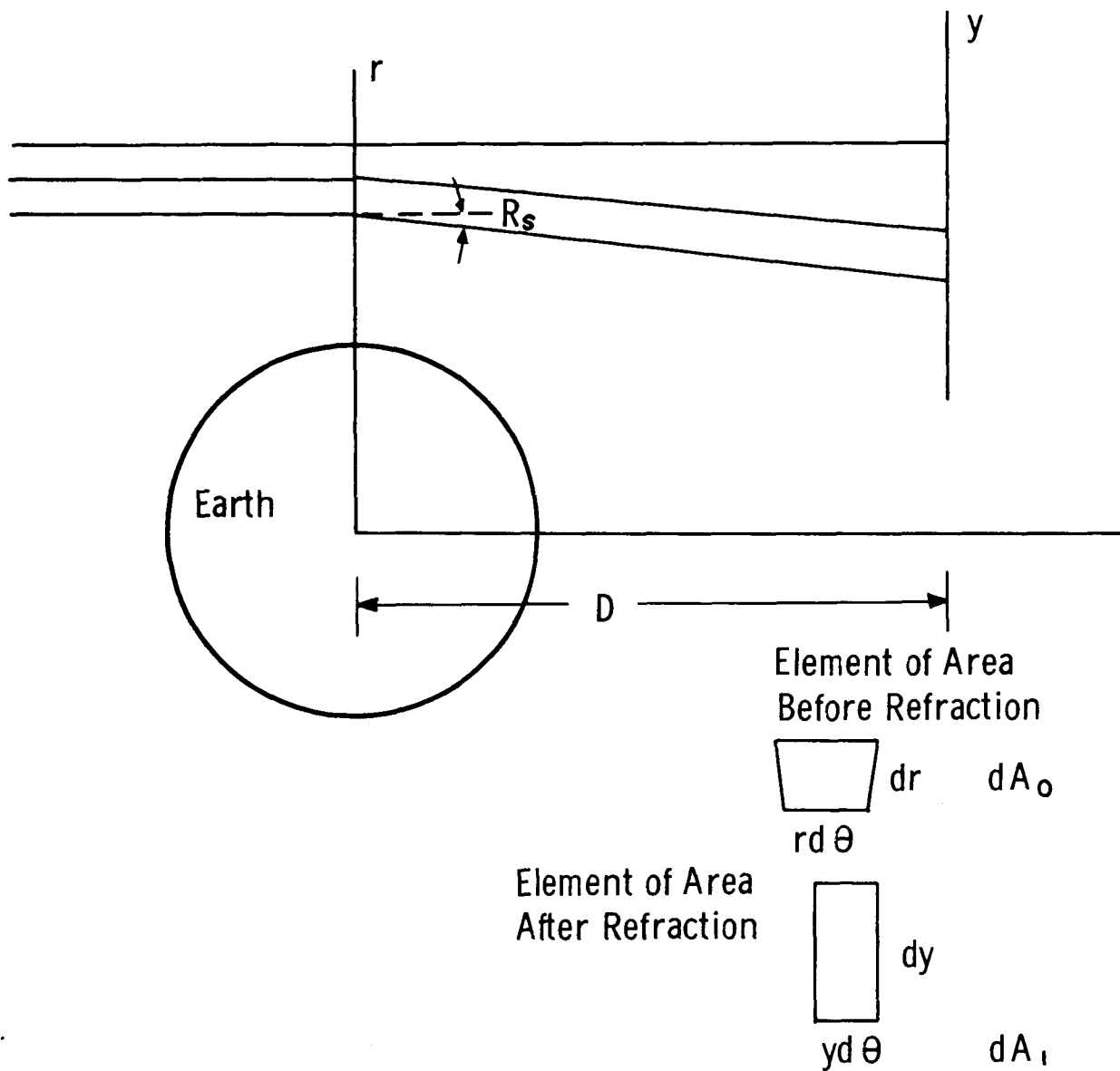
Fig. 11.   Intensity reduction due to differential refraction.

$$\frac{\partial \psi}{\partial k}\bigg|_\theta = \frac{\partial \psi}{\partial k}\bigg|_h - \frac{\partial \psi}{\partial h}\bigg|_k \;\frac{\partial \theta/\partial k|_h}{\partial \theta/\partial h|_k} \; . \tag{12}$$

For an isothermal atmosphere the derivative is

$$\frac{\partial \psi}{\partial k}\bigg|_\theta = \frac{-\dfrac{D}{H}\rho_0\sqrt{\dfrac{2\pi r_0}{H}}}{\left[1+\dfrac{D}{H}\sqrt{\dfrac{2\pi r_0}{H}}\cdot k_0\rho_0\right]^2} + \frac{\dfrac{k_0 D\rho_0}{H^2}\sqrt{\dfrac{2\pi r_0}{H}}}{\left[1+\dfrac{D}{H}\sqrt{\dfrac{2\pi r_0}{H}}\cdot k_0\rho_0\right]^2} \; .$$

$$\frac{2\rho_0\sqrt{\dfrac{\pi r_0}{2H}} - \dfrac{r_0\rho_0}{\sqrt{r_s^2 - [r_0(k_0\rho_0+1)]^2}}}{\dfrac{2k_0\rho_0\pi}{H}\left[\dfrac{H-2r_0}{\sqrt{8\pi r_0 H}}\right] - \dfrac{k_0\rho_0+1-\dfrac{r_0 k_0\rho_0}{H}}{\sqrt{r_s^2 - [r_0(k_0\rho_0+1)]^2}}} \tag{13}$$

Now, by substituting Eqs. (10) and (13) into Eq. (11), the intensity reduction due to differential refraction can be determined as a function of wavelength for a given tangent ray height.

The intensity reduction due to molecular scattering depends upon the scattering coefficient and ray path through the atmosphere and can be expressed as

$$\left[\frac{I}{I_0}\right]_s = \exp\left[-\int_{-\infty}^{\infty} e\,ds\right] , \tag{14}$$

where d_s = element of path through the atmosphere,

$$\epsilon = \text{scattering coefficient} \left[\frac{32\pi^3}{3n\lambda^4} (\mu - 1)^2 \right],$$

$$n = \text{particles}/cm^3 .$$

Since the beam consists of many rays which must pass through a point at the satellite, rays of different wavelength travel at different tangent ray heights within the atmosphere, viz., above h_0 for $\lambda < \lambda_0$, and below h_0 for $\lambda > \lambda_0$. Therefore, when considering the intensity reduction due to molecular scattering care must be taken to insure that the proper ray path is used when evaluating the integral in Eq. (14). The tangent height for a ray of wavelength λ can be determined by

$$h_1 = h_0 + \Delta h , \tag{15}$$

where h_0 = tangent ray height of a ray having a wavelength λ_0. Δh may be obtained by solving the Taylor series expansion in two variables

$$R_s(k,h) = R(k_0,h_0) + \frac{\partial R_s}{\partial k}\bigg|_h \Delta k + \frac{\partial R_s}{\partial h}\bigg|_k \Delta h + \frac{\partial^2 R_s}{\partial k \partial h} \Delta k \, \Delta h + \ldots . \tag{16}$$

Neglecting higher order terms and solving,

$$\Delta h = \frac{R_s(k,h) - R_s(k_0,h_0) - \dfrac{\partial R_s}{\partial k}\bigg|_h \Delta k}{\dfrac{\partial R_s}{\partial h}\bigg|_k} \tag{17}$$

Since $R_s(k,h)$ can also be expressed by Eq. (6),

$$\Delta h = \frac{\left[\dfrac{\partial R_s}{\partial k}\bigg|_\theta - \dfrac{\partial R_s}{\partial k}\bigg|_h \right] \Delta k}{\dfrac{\partial R_s}{\partial h}\bigg|_k} = \left(\frac{\dfrac{\partial \theta}{\partial k}}{\dfrac{\partial \theta}{\partial h}} \right) \Delta k . \tag{18}$$

For an isothermal atmosphere the change in height may be expressed as

$$\Delta h = - \left\{ \frac{2\rho_0 \sqrt{\dfrac{\pi r_0}{2H}} - \dfrac{r_0\rho_0}{\sqrt{r_s^2 - [r_s(k_0\rho_0 +1)]^2}}}{\dfrac{2k_0\pi \rho_0}{H} \left[\dfrac{H-2r_0}{8\pi r_0 H}\right] - \dfrac{k_0\rho_0+1 - \dfrac{r_0 k_0\rho_0}{H}}{\sqrt{r_s^2 - [r_s(k_0\rho_0+1)]^2}}} \right\} \Delta k. \qquad (19)$$

Since $nm = \rho$ and, using the Dale and Gladstone Law, $k\rho = \mu-1$, Eq. (14) may be written as

$$\left[\frac{I(\lambda)}{I_0}\right]_s = \exp. \left[- \frac{32\pi^3}{3\lambda^4} k^2 m \int_{-\infty}^{\infty} \rho ds\right]. \qquad (20)$$

The integral for an isothermal atmosphere can be approximated by neglecting curvature effects due to refraction and

$$\int_{-\infty}^{\infty} \rho ds \cong \int_{\infty}^{\infty} \rho dx \cong 2\rho_1 \int_{h_1}^{\infty} \frac{(r_e+h)e^{-h/H}dh}{\sqrt{r-r_0}} \cong \frac{2\rho_1}{\sqrt{2(r_0+h_1)}} \int_{h_1}^{\infty} \frac{(r_e+h)e^{-h/H}}{\sqrt{h-h_0}}dh$$

$$= \rho_b e^{-h_1/H} \sqrt{\frac{\pi H}{2r_1}} (2r_1 + H), \qquad (21)$$

where $r_1 = r_e + h_1$,

ρ_1 = density at $h_1 = \rho_b e^{-h_1/H}$.

Therefore, the intensity reduction due to molecular scattering may be expressed by

$$\left[\frac{I(\lambda)}{I_0}\right]_s = e^{-\left[\frac{32\pi^3}{3\lambda^4} k^2 m \rho_b(2r_1 + H) \sqrt{\frac{\pi H}{2r_1}} e^{-h_1/H}\right]} \qquad (22)$$

Finally, by replacing

m = 4.808×10^{-26}/kg molecule of air,

k = $[221.051 + 1.663/\lambda^2] \times 10^{-6}$, (m^3/kg),

h = height (km),

H = scale height (km),

λ = wavelength (microns),

ρ_b = density of isothermal atmosphere at ground level (kg/m^3),

Eq. (22) may be written as

$$\left[\frac{I(\lambda)}{I_o}\right]_s = \exp\left[-\frac{32\pi^3}{3\lambda^4} \cdot 4.808\left(221.051 + \frac{1.663}{\lambda^2}\right)^2 \cdot\right.$$

$$\left. \rho_b\left(2(r_e+h_1) + H\right)\sqrt{\frac{\pi H}{2(r_e+h_1)}}\, e^{-h_1/H} \cdot 10^{-11}\right]. \tag{23}$$

The intensity reduction due to ozone absorption depends upon the vertical distribution of ozone within the atmosphere, which varies with time. However, by using the standard density distribution for ozone, as proposed by Altshuler for uniform layers around the earth (shown in Fig. 15), one can determine the effect of ozone absorption for a grazing ray. The intensity reduction due to ozone absorption can be expressed by

$$\left[\frac{I(\lambda)}{I_o}\right]_{O_3} = e^{-k_{O_3}(\lambda)\left[\int_{-\infty}^{\infty}\rho_{O_3}\, ds\right]_{h_1}} = e^{-k_{O_3}(\lambda)\cdot[M_{O_3}]_{h_1}} \tag{24}$$

An analytical function which **closely** approximates the ozone density distribution over the altitude range of interest is given in Ref. 2 by

$$\rho_{O_3} = \frac{\omega_p}{h}\frac{\exp(y-y_p)/h}{[1 + \exp(y-y_p)/h]^2}, \tag{25}$$

where ω_p, y_p, and h are adjusted constants used to fit the particular ozone distribution under consideration. With this ozone density distribution, one can now integrate along a grazing ray path in order to determine the mass of ozone corresponding to a path having a tangent ray height of h_1. The integral can be represented by

$$M_{O_3} = \int_{-\infty}^{\infty} \rho_{O_3} ds \cong \int_{-\infty}^{\infty} \rho_{O_3} dx = 2 \int_{r_1}^{\infty} \frac{\rho_{O_3} r dr}{\sqrt{r^2 - r_1^2}} \quad . \tag{26}$$

Using a linear interpolation for density values,

$$\rho = \rho_i + \frac{\rho_{i+1} - \rho_i}{r_{i+1} - r_i} (r - r_i) \quad . \tag{27}$$

The integral can be expressed as

$$M_{O_3} = 2 \sum_{i=0}^{\infty} \int_{r_i}^{r_{i+1}} \frac{\left[\rho_i + \frac{\rho_{i+1} - \rho_i}{r_{i+1} - r_i} (r - r_i)\right] r dr}{\sqrt{r^2 - r_1^2}} \quad , \tag{28}$$

letting

$$\frac{\rho_{i+1} - \rho_i}{r_{i+1} - r_i} = \beta_i \quad .$$

then,

$$M_{O_3} = 2 \sum_{i=0}^{\infty} \left[(\rho_i - \beta_i r_i) \int_{r_i}^{r_{i+1}} \frac{r dr}{\sqrt{r^2 - r_1^2}} + \right.$$

$$\left. \beta_i \int_{r_i}^{r_{i+1}} \frac{r^2 dr}{\sqrt{r^2 - r_1^2}} \right] \quad . \tag{29}$$

Evaluating the integrals, the ozone mass for a grazing ray having a tangent height h_1 is expressed as

32

$$\left[M_{O_3}\right]_{h_1} = 2 \sum_{i=0}^{\infty} \left\{ (\rho_i - \beta_i r_i) \left[\sqrt{r_{i+1}^2 - r_1^2} - \sqrt{r_i^2 - r_1^2} \right] + \right.$$

$$\left. + \beta_i \left[\frac{r_{i+1}}{2} \sqrt{r_{i+1}^2 - r_1^2} - \frac{r_i}{2} \sqrt{r_i^2 - r_1^2} + \frac{r_0^2}{2} \log\left(\frac{r_{i+1} + \sqrt{r_{i+1}^2 - r_1^2}}{r_i + \sqrt{r_i^2 - r_1^2}} \right) \right] \right\}$$

$$(30)$$

The stellar radiation intensity $I_O(\lambda, T)$ is a function of the stellar type and the star's magnitude, M_V. The energy distribution per wavelength can be obtained by assuming that the star radiates as a black body at an effective temperature which depends upon the stellar type (i.e., Type G-0, $5950^\circ K$). A curve relating the effective radiating temperature to the stellar type for stars on the main sequence is shown in Fig. 12. The magnitude of the radiation above the atmosphere can be related to the visual magnitude by the following expression as given in Allen[1]:

$$I_O = e^{-(0.921 M_V + 19.3875)} \quad \left(\frac{\text{watts}}{\text{cm}^2 - \overset{\circ}{A}} \right) , \qquad (31)$$

where M_V = visual magnitude of the star at a wavelength $\lambda_O = 0.55$. The magnitude of the energy can now be expressed in watts/cm^2 - μ as a function of wavelength, and effective radiating temperature by

$$I_O(\lambda, T) = e^{-(0.921 M_V + 19.3875)} \cdot \frac{\lambda_O^5}{\lambda^5} \frac{\left(e^{-\frac{1.438}{\lambda \cdot T \cdot 10^{-4}}} - 1 \right)}{\left(e^{-\frac{1.438}{\lambda_O T 10^{-4}}} - 1 \right)} \cdot 10^{-3} , \qquad (32)$$

where $\lambda_O = 0.55$, λ = wavelength of ray considered, and T = effective radiating temperature ($^\circ K$). The energy in watts/cm^2-μ received at the optical system of the satellite can now be expressed as

33
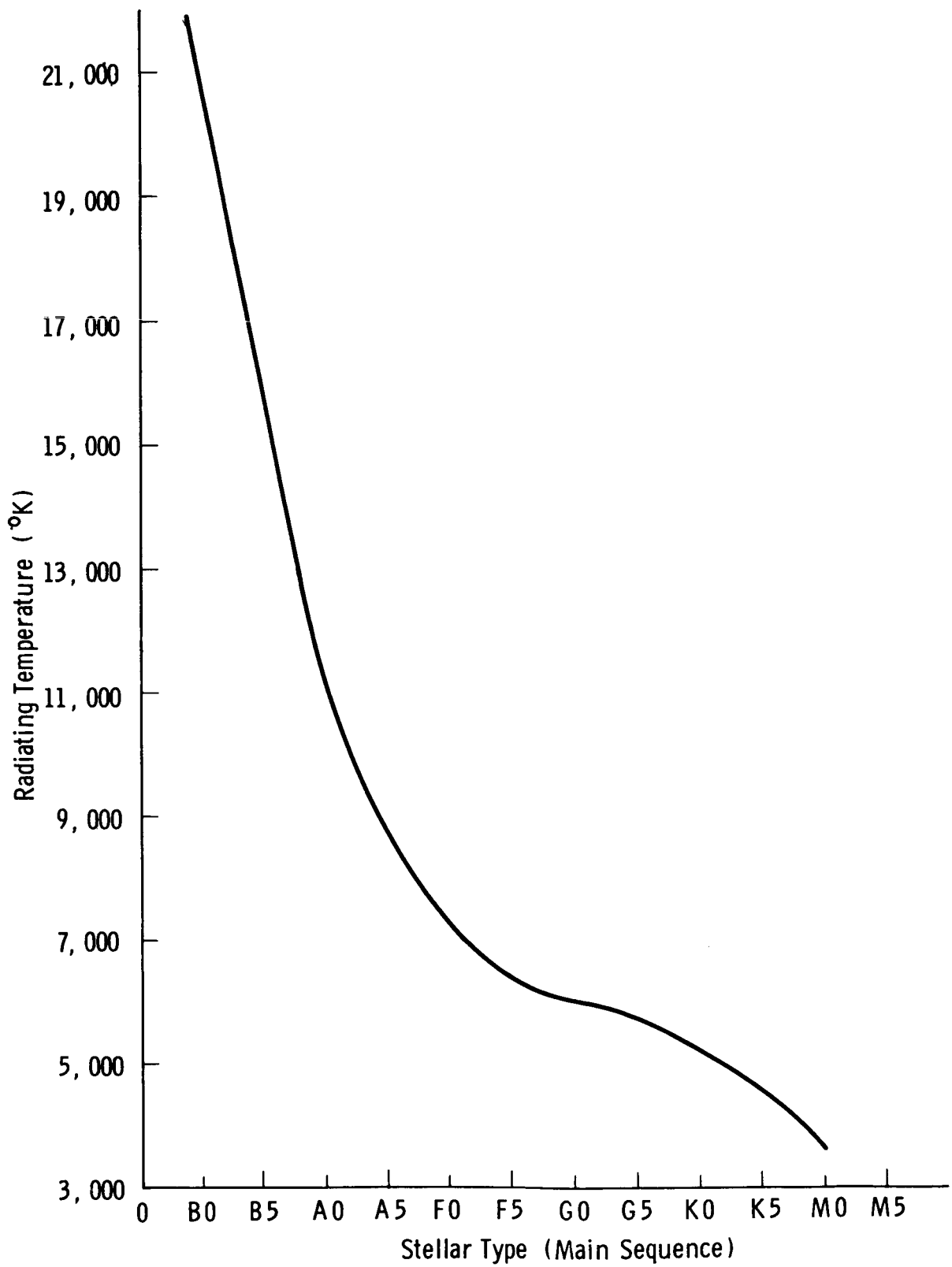
Fig. 12. Effective black body radiating temperature as a function of stellar type.

$$I_o(\lambda, T) \cdot \psi(\lambda) \cdot \left[\frac{I(\lambda)}{I_o}\right]_s \cdot \left[\frac{I(\lambda)}{I_o}\right]_{o_3} \cdot \qquad (33)$$

To determine the output of a typical photocathode, the material characteristics of the photocathode must also be integrated into the analysis. The spectral response of several photocathodes is shown in Fig. 13 as a function of wavelength. Therefore, the output of the photocathode in milliamps $/cm^2$-μ can be expressed by multiplying the intensity reduction factors by the photocathode and star characteristics to yield

$$\frac{\partial E}{\partial \lambda} = I_o(\lambda, T) \cdot \psi(\lambda) \cdot \left[\frac{I(\lambda)}{I_o}\right]_s \cdot \left[\frac{I(\lambda)}{I_o}\right]_{o_3} \cdot P \quad, \qquad (34)$$

where P = photocathode characteristic obtained from Fig. 13 (milliamps/watt).

The total energy output of the photocathode expressed in milliamps/cm^2 is obtained by integrating Eq.(34) over all wavelengths to yield

$$E = \int_0^\infty \frac{\partial E}{\partial \lambda} \, d\lambda \quad . \qquad (35)$$

However, since it is the energy distribution within the image that is of concern, one must obtain the energy distribution as a function of the difference in refraction angle from $R_s(\lambda_o)$:

$$\Delta R_s = R_s(\lambda) - R_s(\lambda_o) \quad . \qquad (36)$$

Therefore,

$$\frac{\partial E}{\partial \Delta R_s} = \frac{\partial E}{\partial \lambda} \cdot \frac{\partial \lambda}{\partial k} \cdot \frac{1}{\left.\frac{\partial R_s}{\partial k}\right|_\theta}$$

$$= -\frac{\lambda^3 \cdot 10^6}{3.327164} \cdot \frac{\partial E}{\partial \lambda} \cdot \frac{1}{\left.\frac{\partial R_s}{\partial k}\right|_\theta} \qquad (37)$$
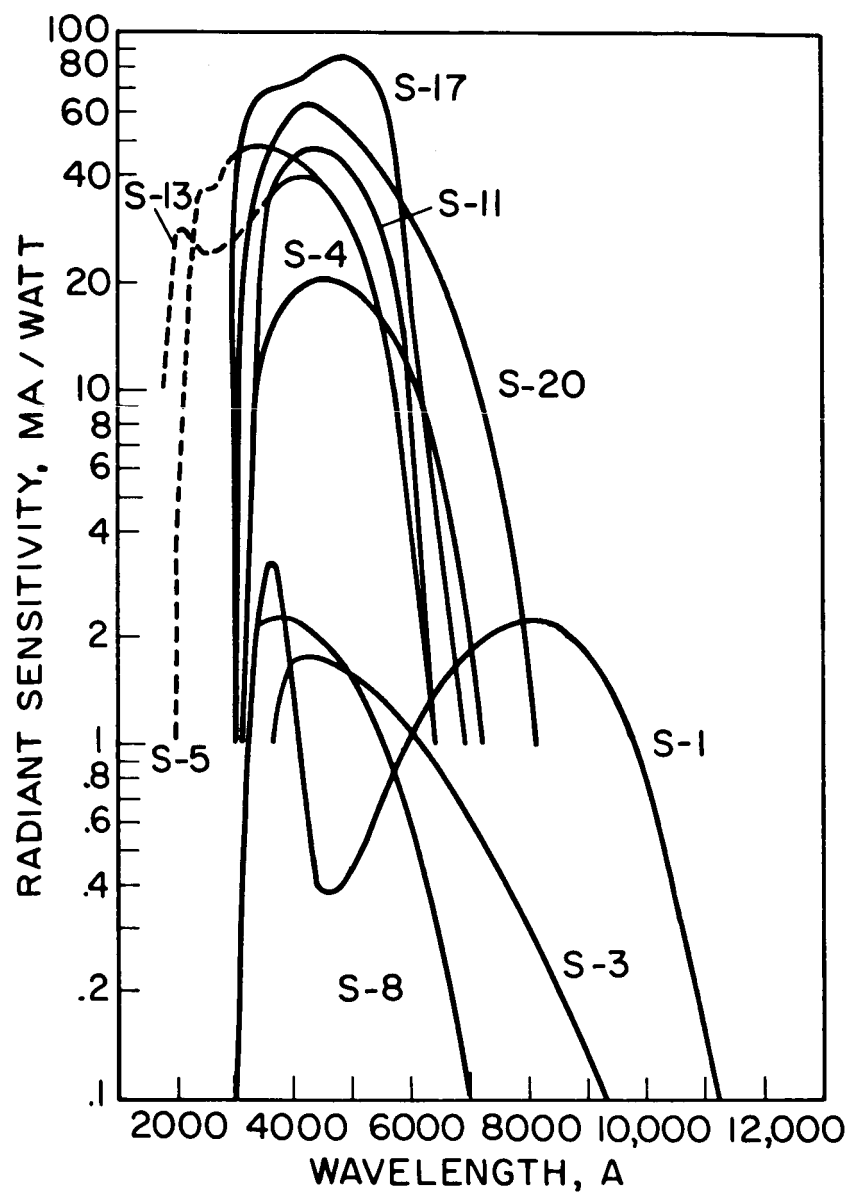
Fig. 13. Average spectral sensitivity characteristics of typical photo-tubes.

and the total energy is again the integral over all refraction angle differences:

$$E = \int_{-\infty}^{\infty} \frac{\partial E}{\partial \Delta R_S} \, d(\Delta R_S) = -\int_{0}^{\infty} \frac{\partial E}{\partial \lambda} \, d\lambda \; . \qquad (38)$$

The center of gravity of the photocathode image is important since it will be used to determine the refraction angle of the star. Thus, once the center of gravity is located, its wavelength can be used to determine the tangent ray height at which the density is determined from the inversion process. The center of gravity can be determined from

$$\overline{\Delta R_S} = \frac{\displaystyle\int_{-\infty}^{\infty} \Delta R_S \cdot \frac{\partial E}{\partial \Delta R_S} \, d(\Delta R_S)}{\displaystyle\int_{-\infty}^{\infty} \frac{\partial E}{\partial \Delta R_S} \, d(\Delta R_S)} \qquad (39)$$

The center of gravity of the image is a function of tangent ray height, h_O, and will most likely shift in position as the star occults.

The refraction angle corresponding to the center of gravity is therefore

$$\overline{R}_S = R_S(k_O) + \overline{\Delta R_S} \qquad (40)$$

Also,

$$\overline{R}_S = R_S(k_O) + \left.\frac{\partial R_S}{\partial k}\right|_\theta \overline{\Delta k} \; . \qquad (41)$$

Therefore, $\overline{\Delta k}$ may be expressed in two ways by

$$\overline{\Delta k} = \frac{\overline{R}_S - R_S(k_O)}{\left.\dfrac{\partial R_S}{\partial k}\right|_\theta} \qquad (42)$$

and $\quad \overline{\Delta k} = 1.6636 \times 10^{-6} \left(\dfrac{1}{\overline{\lambda}^2} - \dfrac{1}{\lambda_O^2} \right) . \qquad (43)$

The wavelength of the center of gravity may be determined from

$$\bar{\lambda} = \sqrt{\frac{\lambda_o^2}{1 + \frac{\lambda_o^2 \,\overline{\Delta k}}{1.6636 \times 10^{-6}}}} \,.\qquad (44)$$

The tangent ray height of this wavelength will differ from the tangent ray height of the base ray λ_o by

$$\overline{\Delta h} = -\left\{\frac{2\rho_o \sqrt{\frac{\pi r_o}{2H}} - \frac{r_o \rho_o}{\sqrt{r_s^2 - [r_o(k_o\rho_o+1)]^2}}}{\frac{2k_o\pi\,\rho_o}{H}\left[\frac{H-2r_o}{8\pi r_o H}\right] - \frac{k_o\rho_o + 1 - \frac{r_o k_o \rho_o}{H}}{\sqrt{r_s^2 - [r_o(k_o\rho_o+1)]^2}}}\right\}\overline{\Delta k}\,.$$

$$(45)$$

The tangent ray height corresponding to the image center of gravity at wavelength $\bar{\lambda}$ is

$$\overline{h_1} = h_o + \overline{\Delta h} \qquad (46)$$

If the characteristics of a star having a visual magnitude of + 1.0 and the photocathode characteristics are integrated over the wavelength band under consideration, the results can be arbitrarily defined as a photocathode magnitude of + 1.0. In this manner a decrease of photocathode magnitude as the star is being occulted can be expressed by

$$M_2(h) = M_1 + \log_{10} \frac{\int_o^\infty I_o(\lambda,T) \cdot P \cdot d\lambda}{\int_o^\infty \frac{\partial E(h)}{\partial \lambda} \, d\lambda}\,, \qquad (47)$$

where

M_1 = initial photocathode magnitude above the atmosphere,

P = photocathode characteristics,

M_2 = photocathode magnitude at a given height viewed through the atmosphere.

38

The photocathode magnitude is a function of the tangent ray height as the star sets in the atmosphere, and it gives a measure of the effect of overall extinction processes at various tangent ray heights.

Results

The analysis was performed on an isothermal atmosphere having a scale height, H, of 6.406 km, and a density at 10 km equal to the standard atmospheric density at 10 km. This yielded a ground level density of 1.99 kg/m^3. Other parameters used are

radius of the earth, (r_e)	— 6371 km
radius of the orbiting satellite, (r_s)	— 7471 km
base wavelength, (λ_o)	— 0.7 μ
tangent ray heights, (h_o)	— 5, 10, . . ., 40 km
star visual magnitude, (M_v)	— +1.0 at $\lambda_o = 0.55$
star type	— GO
star effective black body temperature	— 5950°K
photocathodes	— S-20 and S-1

The ozone absorption coefficient is shown in Fig. 14 as a function of wavelength, and the assumed atmospheric ozone distribution is shown in Fig. 15. With these parameters, the effect of differential refraction on the radiation intensity reduction is shown in Fig. 16. The intensity reduction due to molecular scattering within the atmosphere is shown in Fig. 17 for the various wavelengths. The intensity reduction due to ozone absorption for the assumed ozone distribution within the atmosphere, and calculated for a grazing ray at tangent ray height h_o, is shown in Fig. 18 for various wavelengths.

The analysis was conducted for two phototubes, the S-20 and the S-1, both of which seemed promising for the desired application. The S-20 appears attractive due to the large output obtained over the wavelengths from 0.3 to 0.8 microns, whereas the S-1, although having a smaller output, covered the larger range of wavelengths from 0.3 to 1.1 microns. The images on the photocathode are shown in Fig. 19-21 for the S-20 at various tangent ray heights, and in Fig. 22-25 for the S-1. The analysis covered all wavelengths; however, it appears to be desirable to restrict the wavelength band in order to obtain a sharper image and locate the center of gravity near the midpoint of the central image. This applies especially to the image on the S-1 photocathode, where a

Ozone Absorption Coefficient as a Function of Wavelength
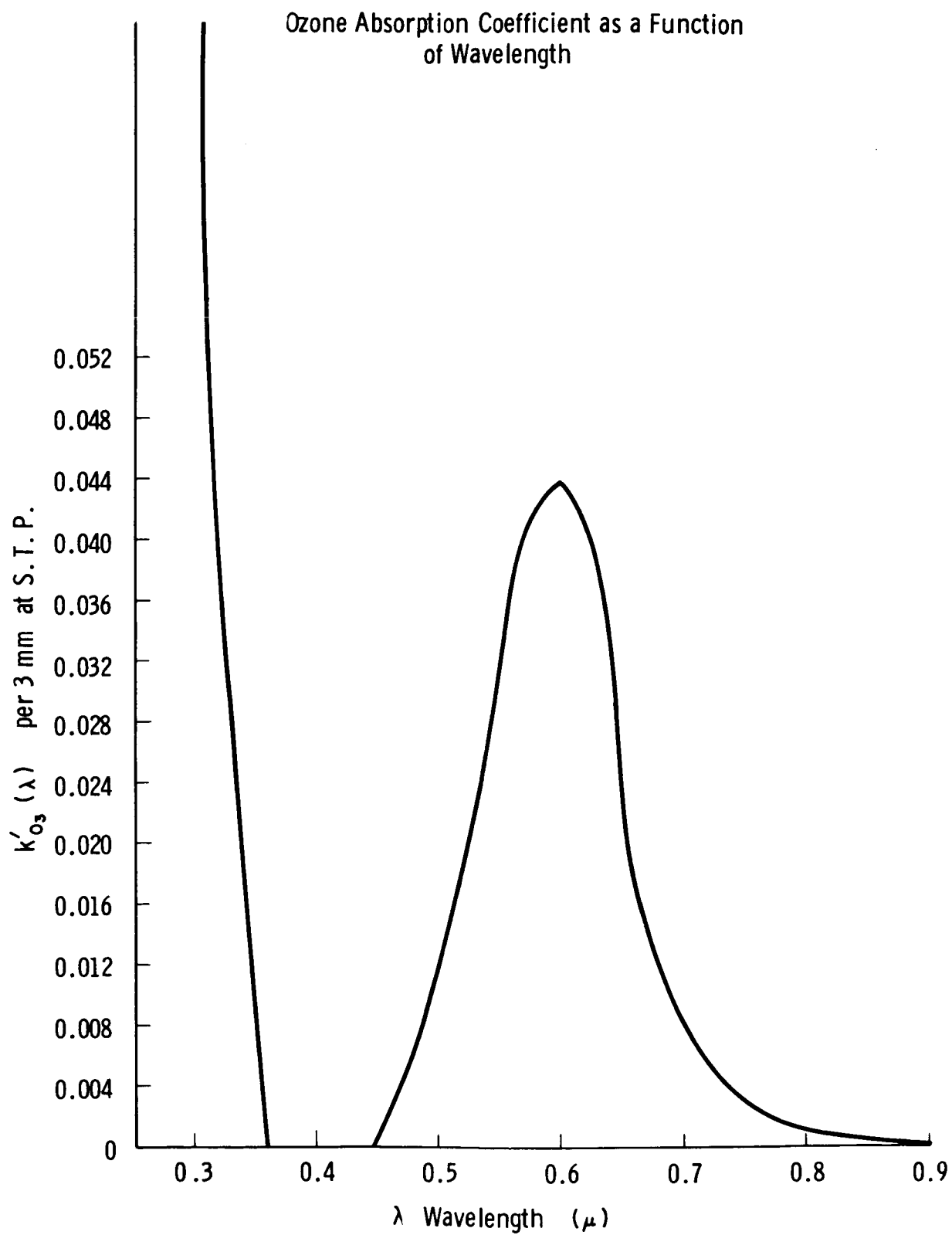
Fig. 14. Ozone absorption coefficient as a function of wavelength, from Allen[1].
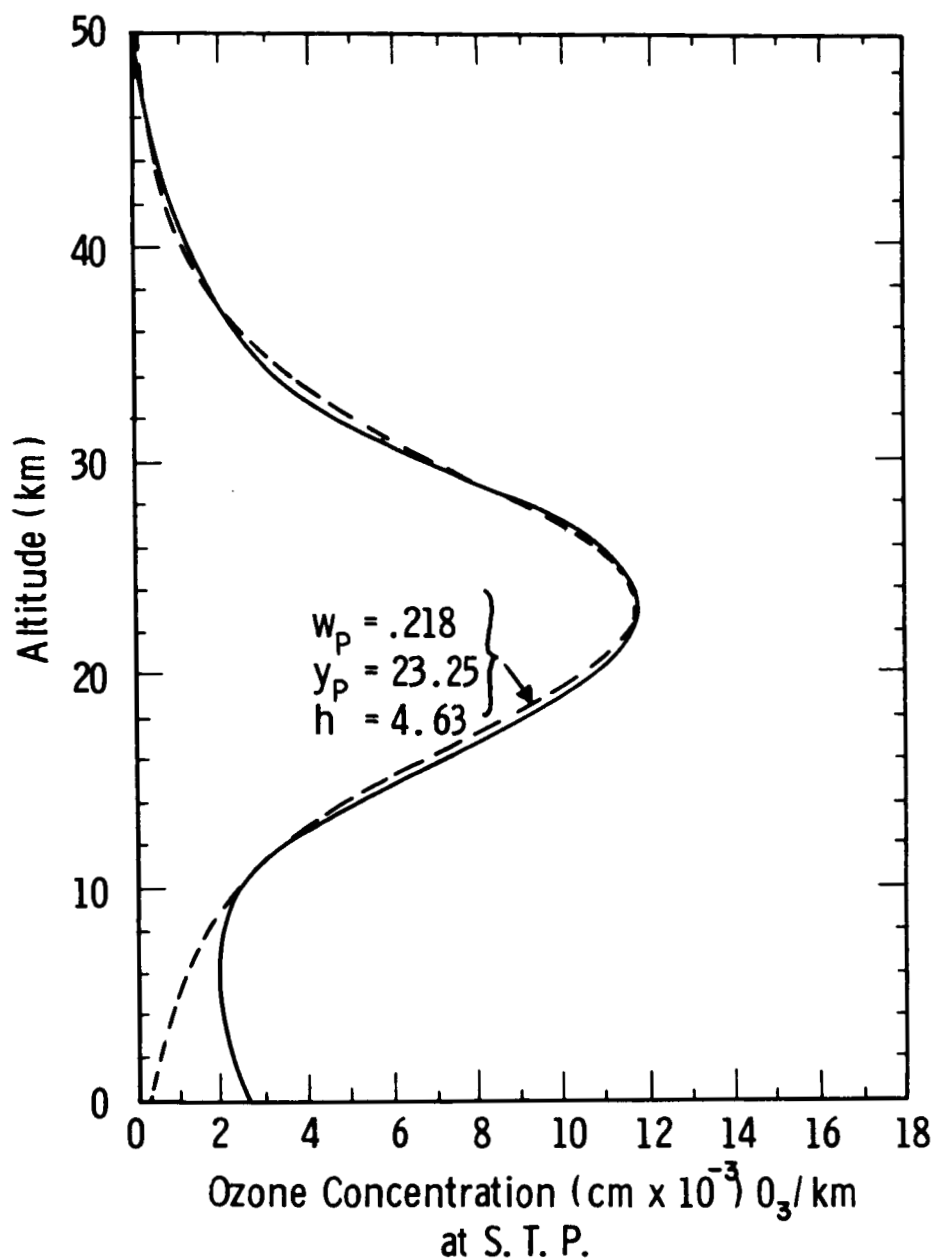
Fig. 15. A "standard" density distribution for ozone. The solid curve
shows a "standard" density for ozone proposed by Altshuler[2]. It cor-
responds to 0.229 atm-cm of ozone in a vertical column. The dashed curve
represents the analytical fit with the parameters w_p, y_p, and h as indicated
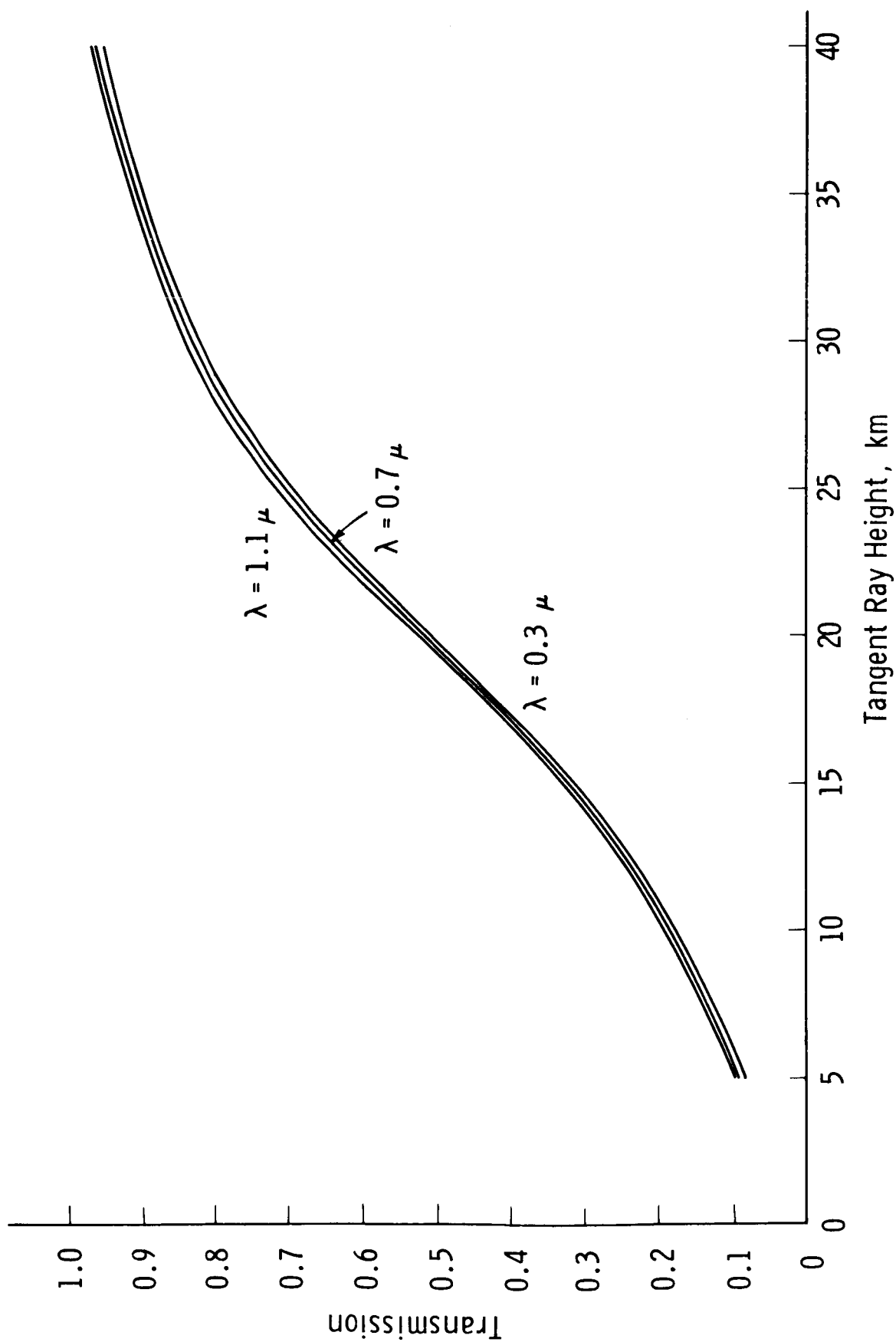
Fig. 16. Intensity reduction due to differential refraction in an isothermal atmosphere.
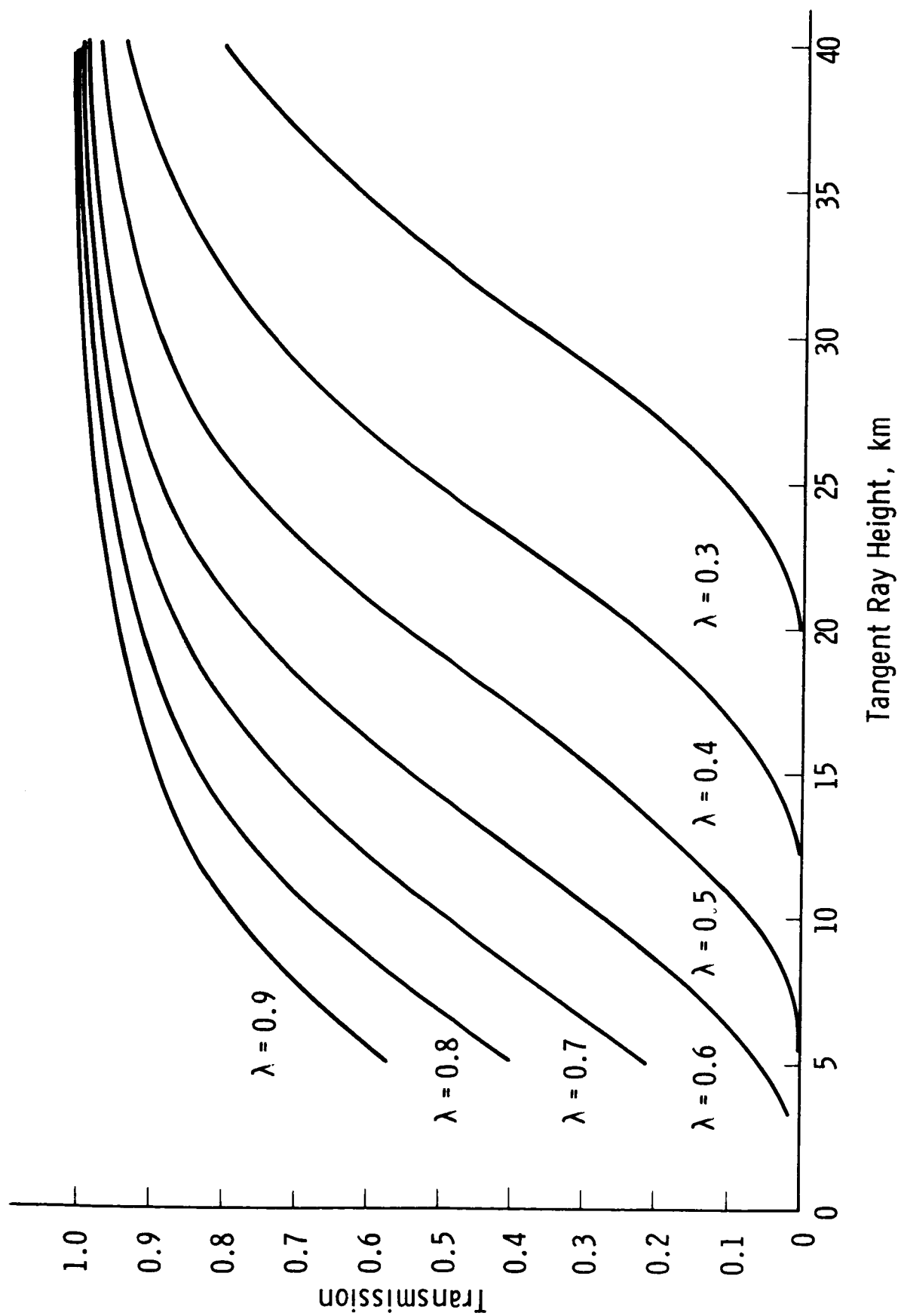
Fig. 17. Intensity reduction due to molecular scattering in an isothermal atmosphere.
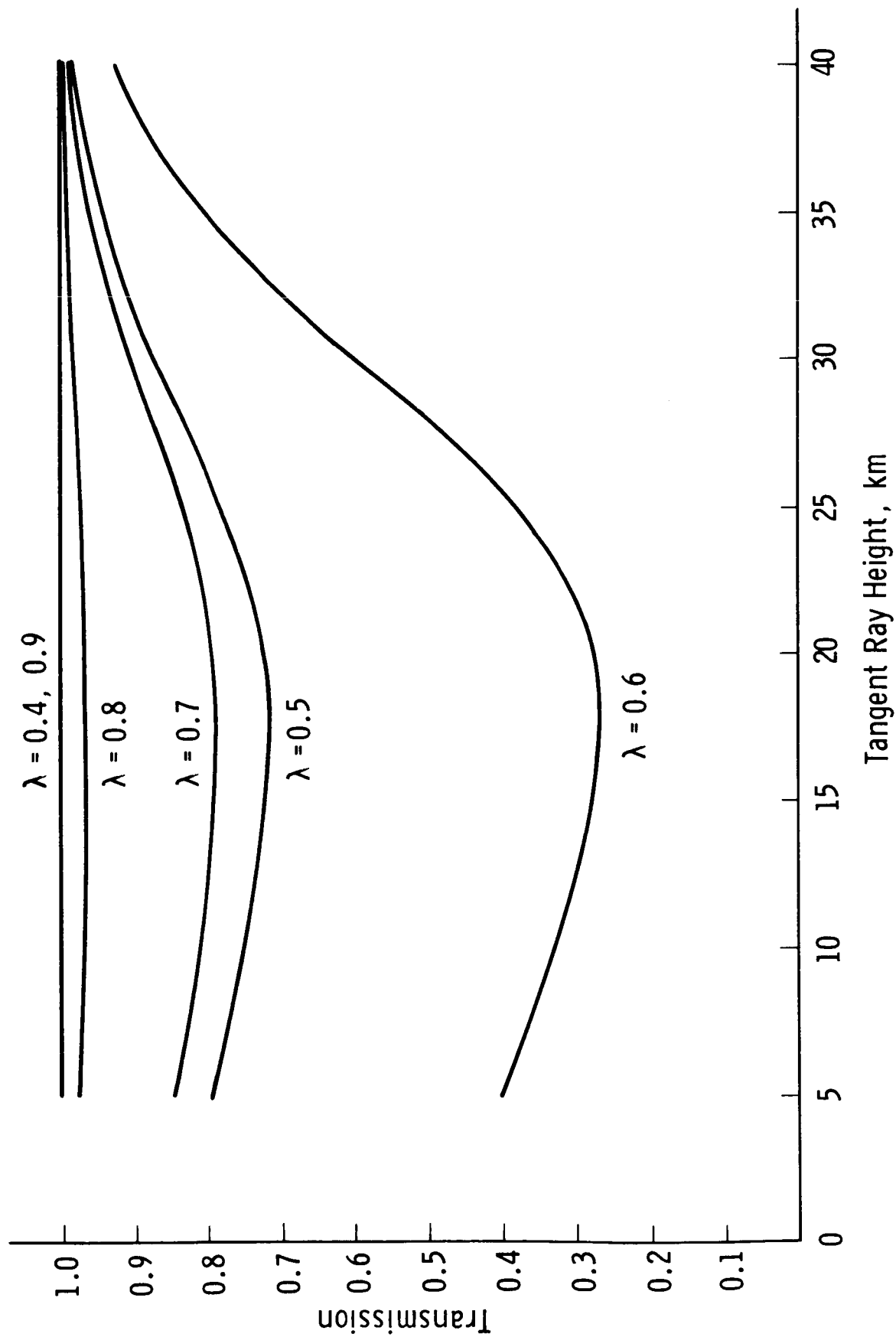
Fig. 18. Intensity reduction due to ozone absorption; standard ozone distribution.
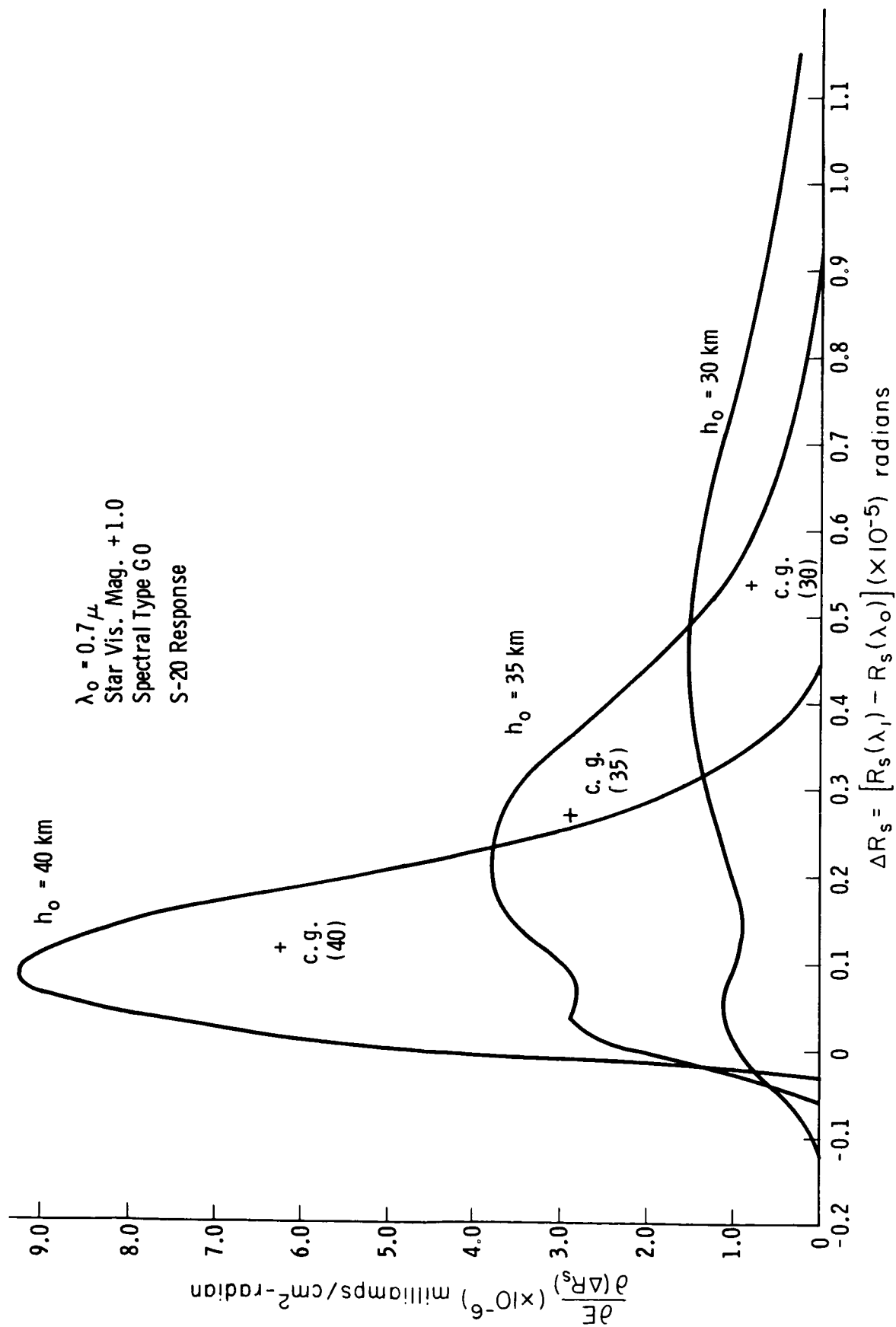
Fig. 19. Energy distribution and center of gravity for photocathode images at tangent ray heights 40 km-30 km in an isothermal atmosphere (S-20 response).

$\lambda_o = 0.7 \mu$
Star Vis. Mag. +1.0
Spectral Type G 0
S-20 Response

$h_o = 40$ km

$h_o = 35$ km

$h_o = 30$ km

$+$ c.g. (40)

$+$ c.g. (35)

$+$ c.g. (30)

$\Delta R_s = [R_s(\lambda_1) - R_s(\lambda_o)](\times 10^{-5})$ radians

$\frac{\partial E}{\partial (\Delta R_s)} (\times 10^{-6})$ milliamps/cm^2-radian

45

Fig. 20. Energy distribution and center of gravity for photocathode images at tangent ray heights 25 km-15 km in an isothermal atmosphere (S-20 response).
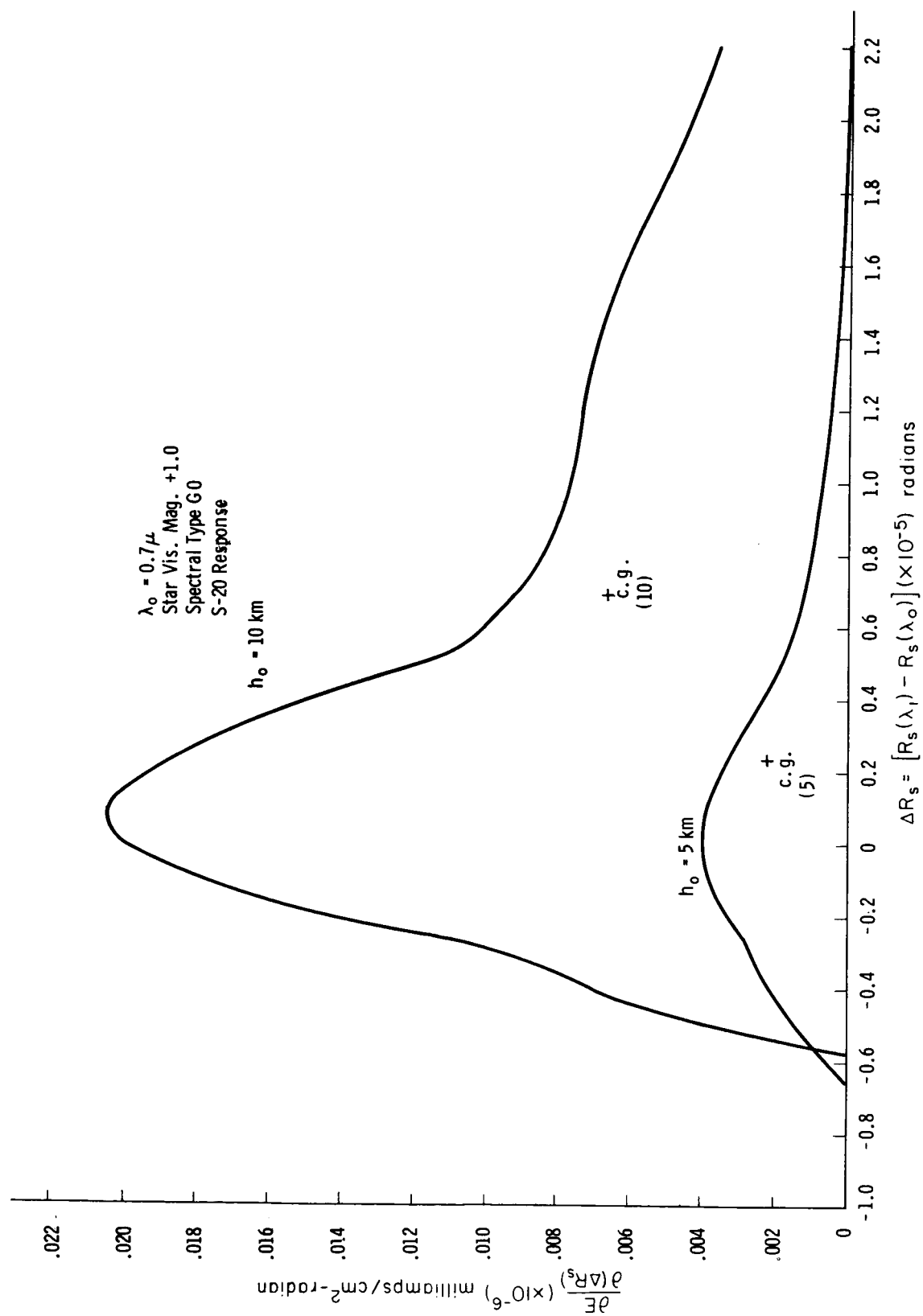
Fig. 21. Energy distribution and center of gravity for photocathode images at tangent ray heights 10 km–5 km in an isothermal atmosphere (S-20 response).

The plot axes and labels:

Y-axis: $\dfrac{\partial E}{\partial(\Delta R_s)}$ ($\times 10^{-6}$) milliamps/cm²-radian

X-axis: $\Delta R_s = [R_s(\lambda_l) - R_s(\lambda_o)](\times 10^{-5})$ radians

$\lambda_o = 0.7\,\mu$
Star Vis. Mag. +1.0
Spectral Type G0
S-20 Response

$h_o = 10$ km

$h_o = 5$ km

+ c.g. (10)

+ c.g. (5)

Fig. 22. Energy distribution and center of gravity for photocathode images at tangent ray heights 40 km–35 km in an isothermal atmosphere (S-1 response).
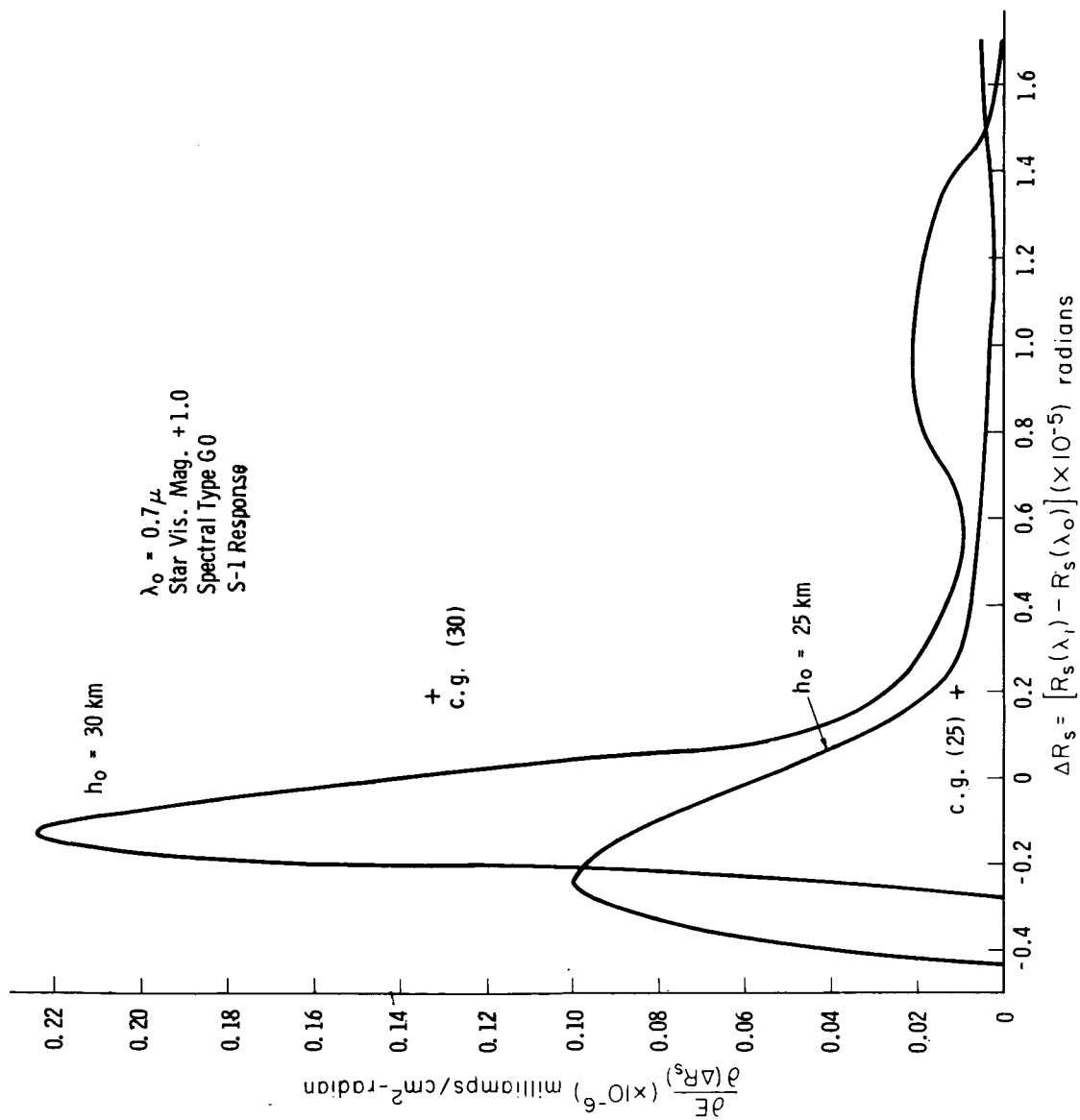
Fig. 23. Energy distribution and center of gravity for photocathode images at tangent ray heights 30 km-25 km in an isothermal atmosphere (S-1 response).
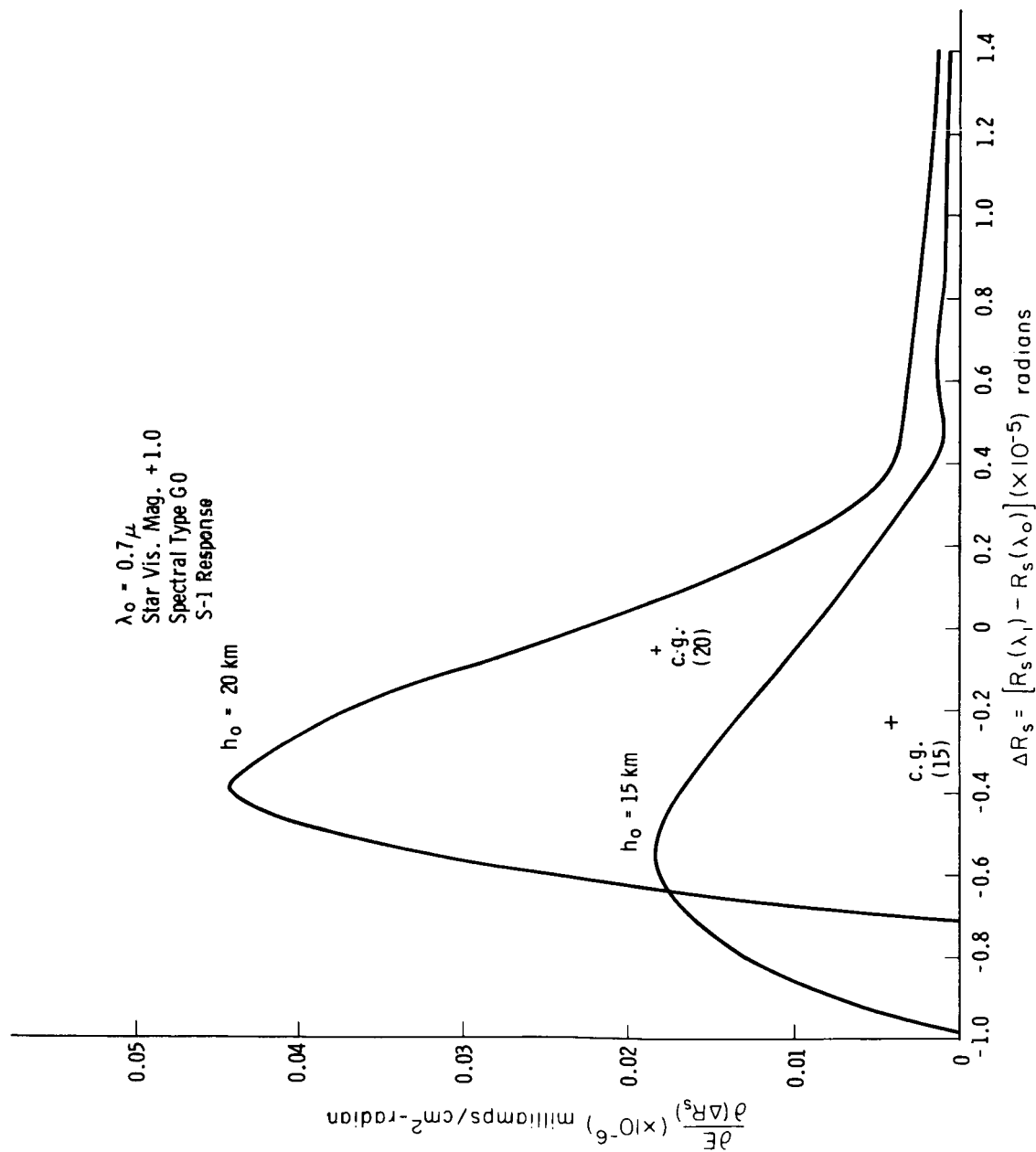
Fig. 24. Energy distribution and center of gravity for photocathode images at tangent ray heights 20 km–15 km in an isothermal atmosphere (S-1 response).
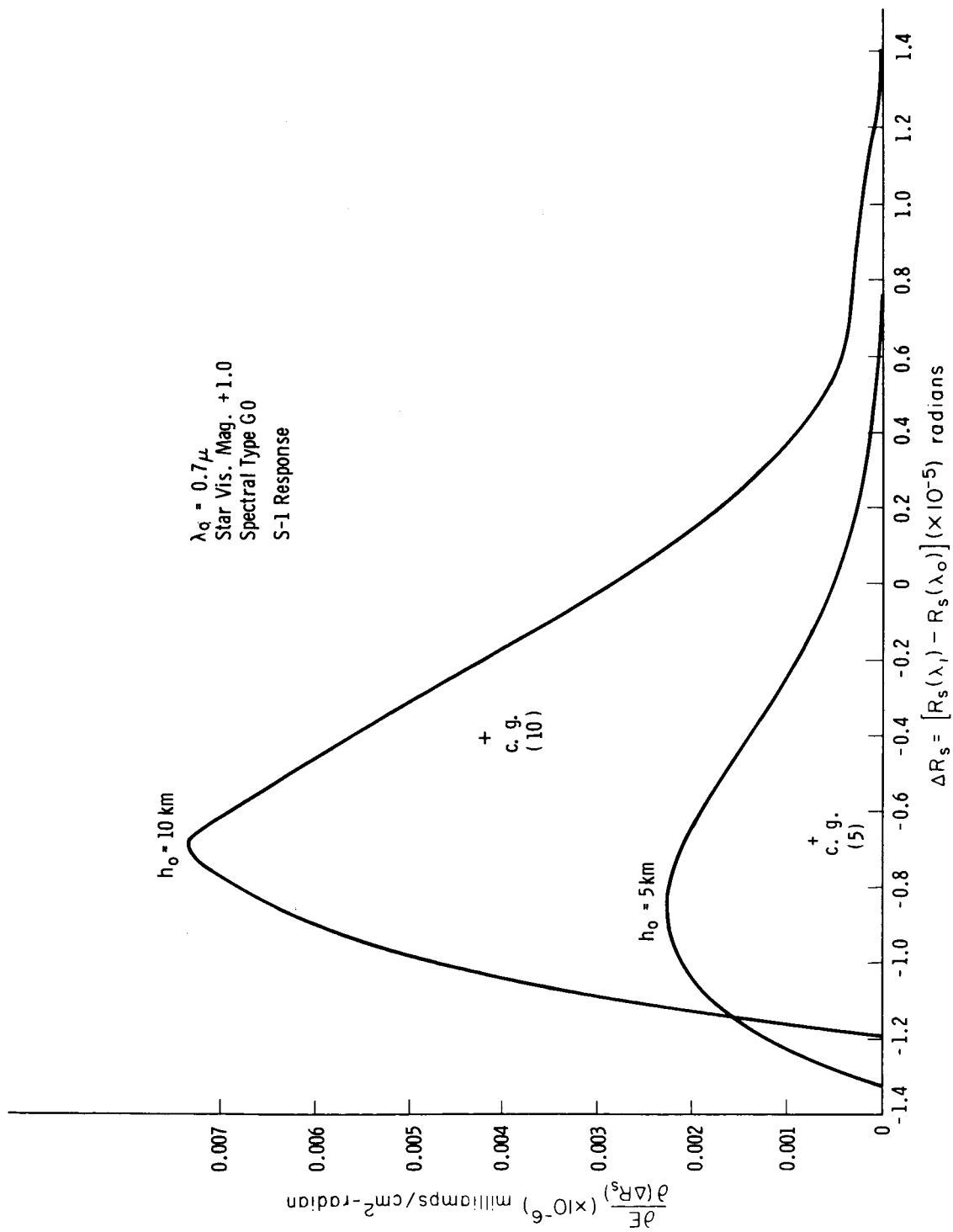
Fig. 25. Energy distribution and center of gravity for photocathode images at tangent ray heights 10 km-5 km in an isothermal atmosphere (S-1 response).

low output is spread over the shorter wavelengths having larger refraction angles, and a large output is obtained over the larger wavelengths where the refraction angle is smaller. This shifts the center of gravity of the image away from the peak region, as shown in the Figs. 22-25, and it may be desirable to restrict the waveband in order to center the center of gravity in the peaked region.

The centers of gravity of the images obtained at various tangent ray heights tend to shift as the star is occulted. Figure 26 shows the shift in the center of gravity for the S-20 photocathode where an overall shift of 2.33 arc-seconds occurs, and also shows the corresponding shift for the S-1 photo-cathode; however, since it operates more in the red end of the spectrum it shifts only 1.74 arc-seconds. Figure 26 shows that the center of gravity shift is initially small, since the atmosphere is thin at high altitudes and little differential refraction occurs. As the tangency point of the grazing ray d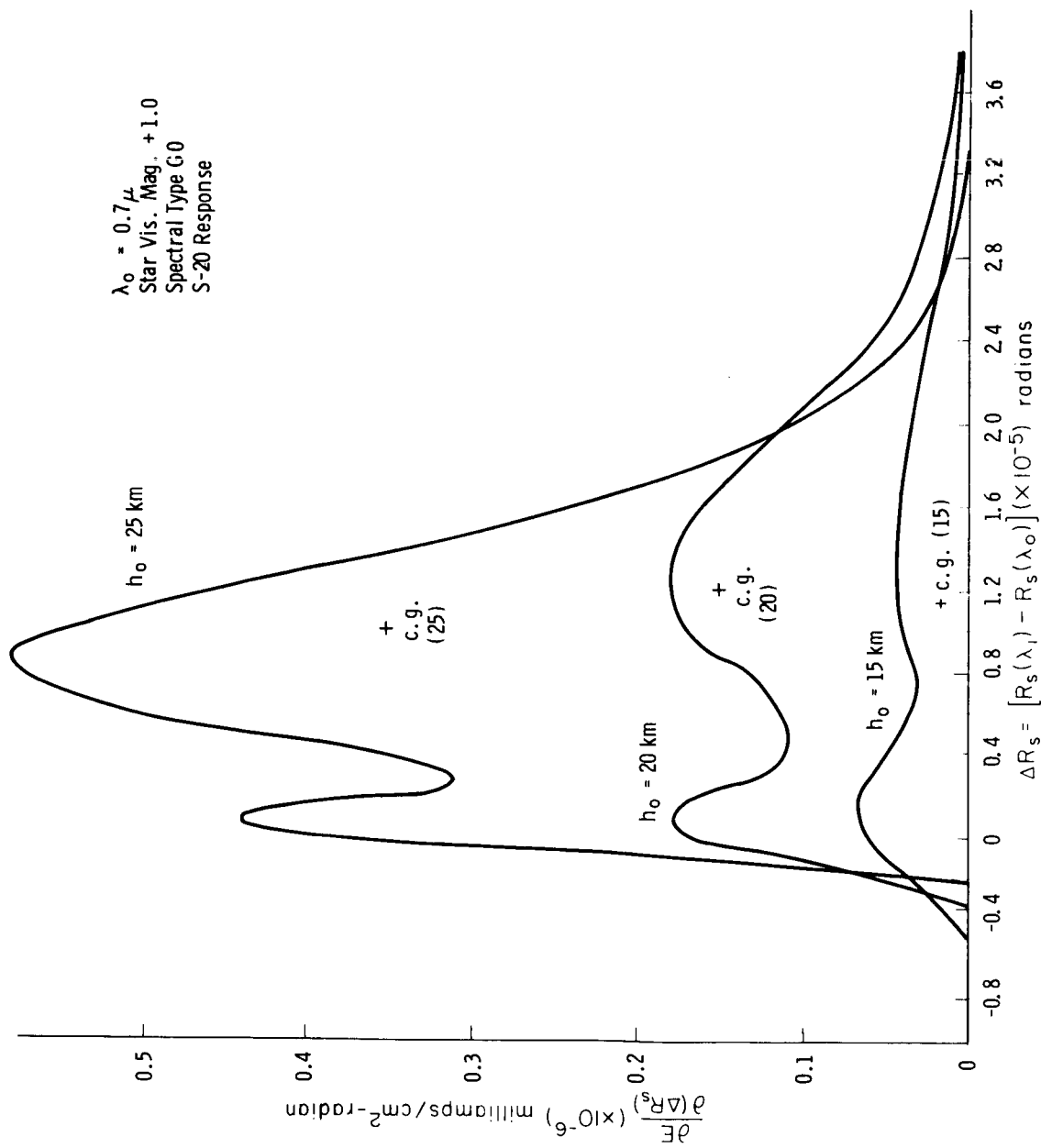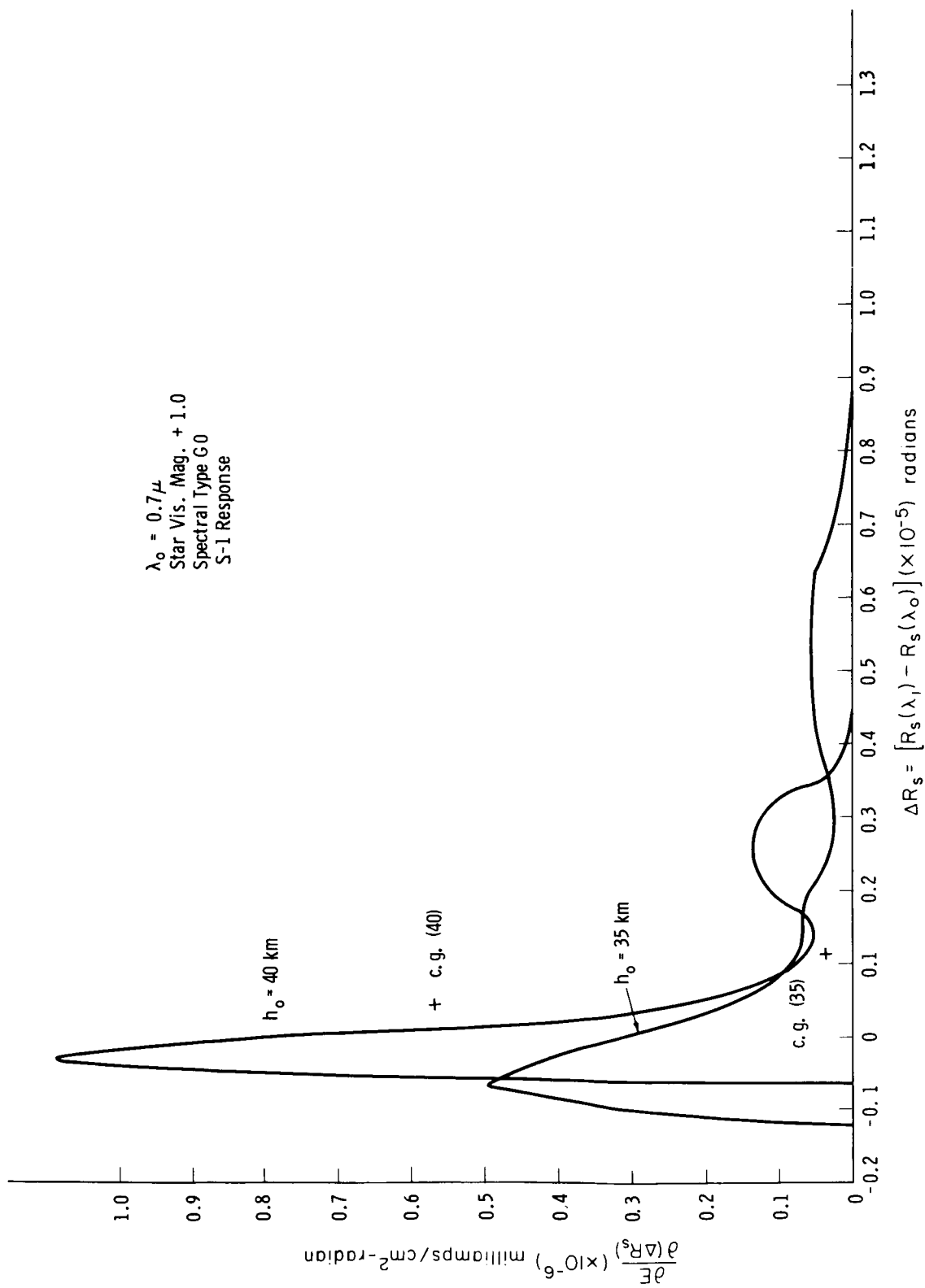ecreases, differential refraction causes the center of gravity to shift to the blue end of the spectrum. However, at about 20 km, scattering and ozone absorption play an important part in the energy distribution and shift the center of gravity back to the red end of the spectrum. The shift in the center of gravity is much less for the S-1 photosensor, since it responds mainly in the red and scattering is not as influential.

Figure 27 gives the decrease in photocathode magnitude with tangent ray height from an arbitrarily assigned initial value of + 1.0, corresponding to a star with visual magnitude +1.0. Since the S-1 has greater response at longer wavelengths, and the extinction processes are not as pronounced, the S-1 suffers less magnitude change than the S-20 as the star sets.

The energy output of the two photocathodes in milliamps/cm^2 of surface is shown in Fig. 28. The larger output of the S-20 sensor is partially offset by the greater change in photocathode magnitude during a scan. Thus, between tangent ray heights of 40 km and 5 km, the S-20 undergoes a change of about three orders of magnitude, whereas the S-1 changes two orders of magnitude. In view of these photocathode characteristics, other factors must also be considered before a final selection of the photocathode can be made. The image energy distribution curves given in Figs. 19-21 for the S-20, and in Figs. 22-25 for the S-1, along with the shift of the image center of gravity in Fig. 26, and the decrease in photocathode magnitude during occultation in Fig. 27, summarize the parameters which define the image characteristics necessary in the design of a suitable star-tracker.

B. ANALYTIC MODEL ATMOSPHERE

Using the geometry of the refracted ray shown in Fig. 9, an image analysis can be performed on an arbitrary model atmosphere. It was desired that the density function be smooth; therefore the atmosphere defined in Ref. 10 was chosen. The exact choice of a model was quite unimportant, as may be seen by
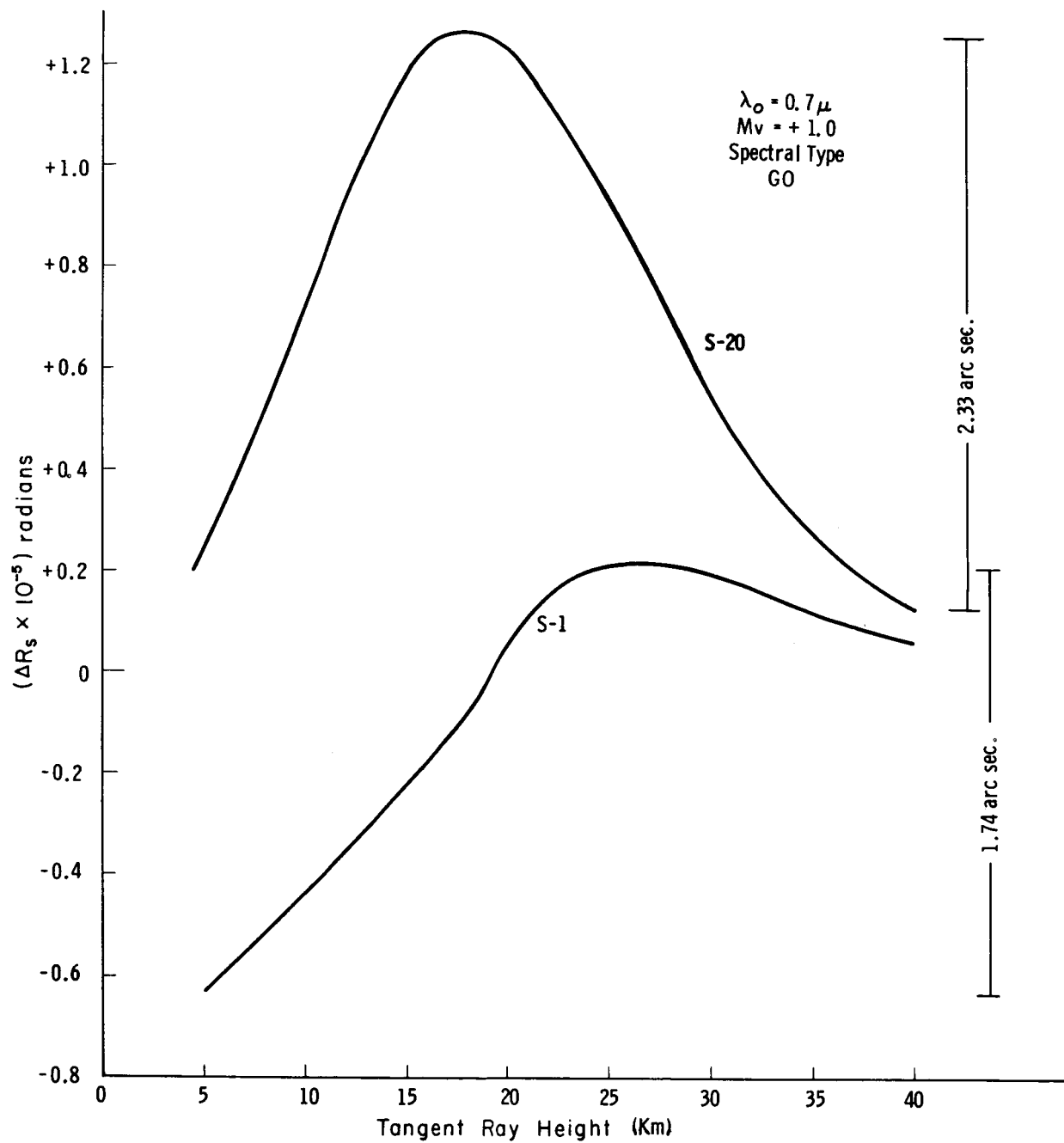
Fig. 26. Image center of gravity shift of photocathode during scan, isothermal atmosphere.

Fig. 27. Photocathode magnitude as a function of tangent ray height.

Initial Photocathode Magnitude + 1.0
Arbitrarily Assigned Equal to   + 1.0
Visual Magnitude Star
Spectral Type G0
Isothermal Atmosphere
$\lambda_o = 0.7_\mu$

$M_v = 1$

S-20

S-1

Tangent Ray Height, km

Photocathode Magnitude

54

$$E = \int_0^\infty \frac{\partial E}{\partial \lambda}\ d\lambda$$
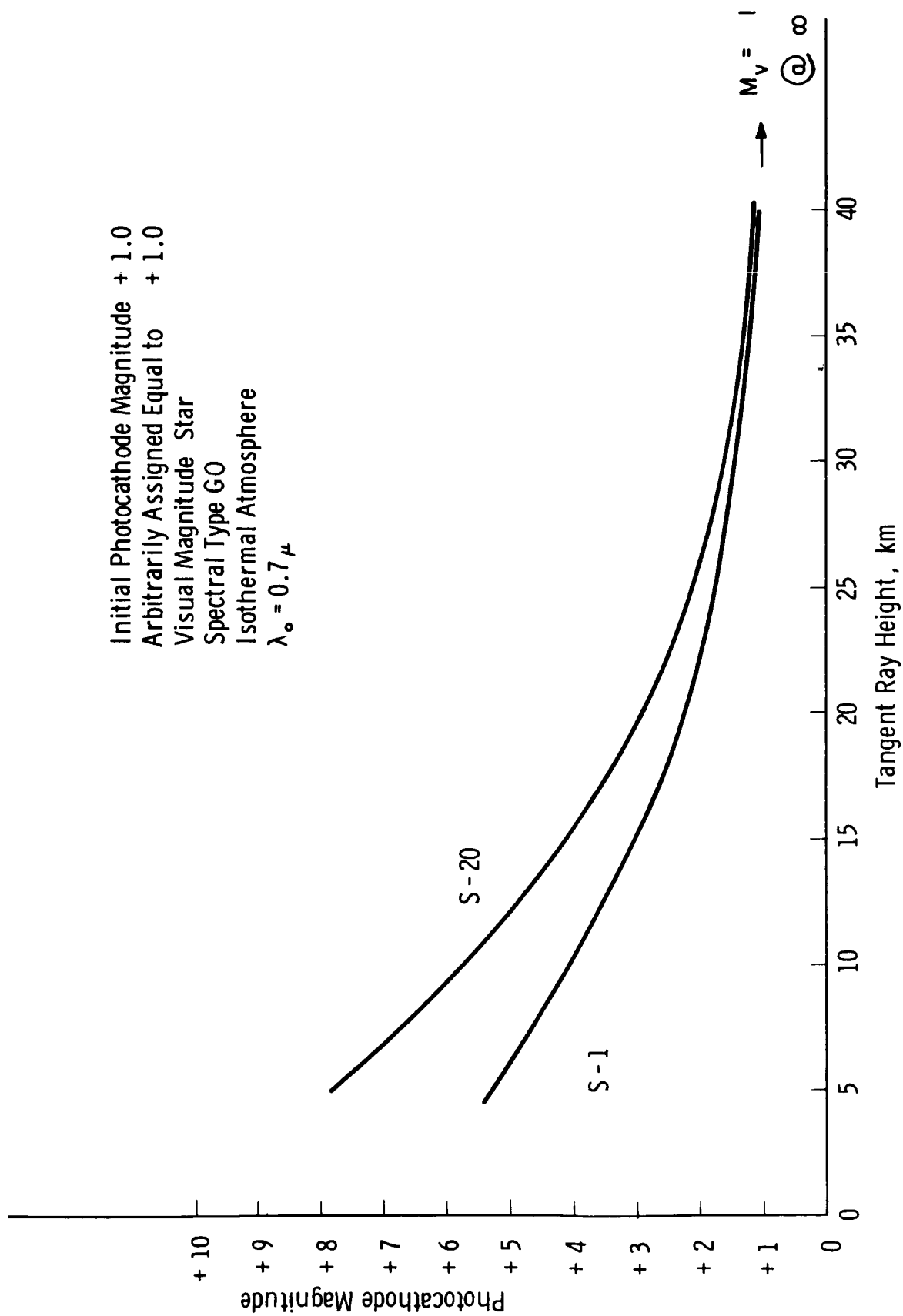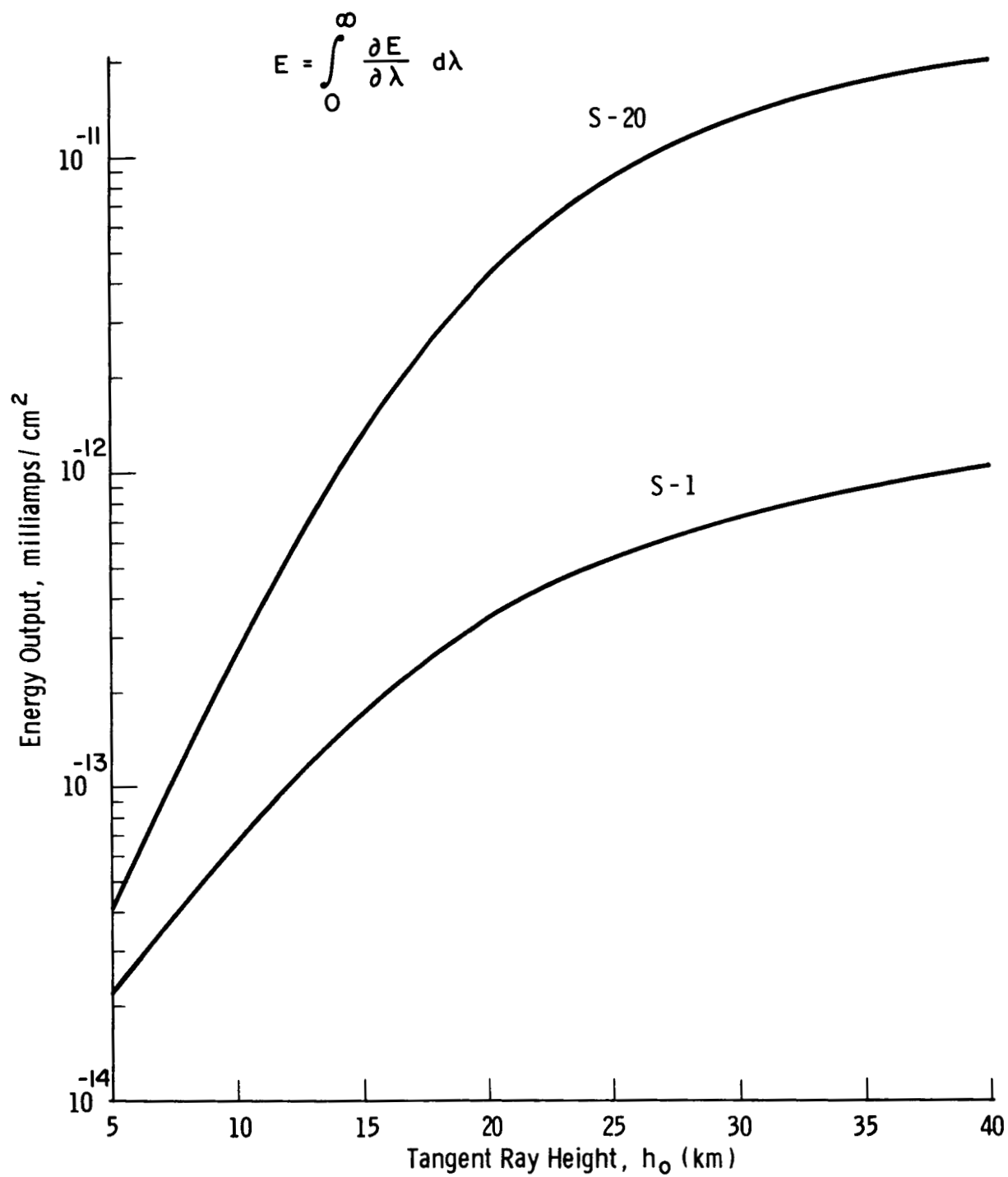
Fig. 28. Magnitude of energy output of photocathode for various tangent ray heights.

comparing these results with those for the isothermal atmosphere. The same extinction factors are again used, namely, differential refraction, molecular scattering, and ozone absorption. Since analytical expressions cannot be obtained for the various extinction factors in the model atmosphere, an IBM 7090 computer was used to evaluate these factors numerically.

The refraction angle of a grazing ray passing through the model atmosphere to an orbiting satellite can be expressed in the following manner, as shown in Hays and Fischbach[8]:

$$R(\eta_o) = 2\eta_o \int_{\eta_o}^{\infty} \frac{\frac{d \log \mu}{d\eta} d\eta}{\sqrt{\eta^2 - \eta_o^2}} \quad , \tag{48}$$

where

$$\eta_o = \mu_o r_o \, ,$$

$$\eta = \mu r \, ,$$

μ = index of refraction related to the density by the Dale and Gladstone Law[9],

$$r = r_e + h.$$

From Ref. 8, the exact inversion in solving for the density profile, given the measured refraction angles, is

$$\mu = k\rho + 1 = \exp\left\{ -\frac{1}{\pi} \int_{\eta}^{\infty} \frac{R(\eta_o) d\eta_o}{\eta_o^2 - \eta^2} \right\} \tag{49}$$

The angle Θ as obtained from the geometry in Fig. 9 is

$$\Theta = \frac{\pi}{2} + R_s - \sin^{-1}\left[\frac{(r_e + h_o)(k_o \rho_o + 1)}{r_s} \right] , \tag{5}$$

where ρ_o = density at tangent ray height h_o in the model atmosphere (kg/m^3),

r_s = radius of satellite orbit (km).

As in the case of the isothermal atmosphere, the variation of the refraction angle as a function of wavelength of rays incident upon the orbiting satellite may be obtained by an expansion about the point h_o, for a constant Θ,

as,

$$R_s(k,h) = R_s(k_o,h_o) + \left.\frac{\partial R_s}{\partial k}\right|_\theta \Delta k + \ldots \quad , \tag{6}$$

neglecting higher order terms. Again the derivative $\left.\dfrac{\partial R_s}{\partial k}\right|_\theta$ is

$$\left.\frac{\partial R_s}{\partial k}\right|_\theta = \left.\frac{\partial R_s}{\partial k}\right|_h - \left.\frac{\partial R_s}{\partial h}\right|_k \cdot \frac{\partial\theta/\partial k|h}{\partial\theta/\partial h|k} \quad ; \tag{7}$$

and for the model atmosphere this can be expressed as

$$\left.\frac{\partial R_s}{\partial k}\right|_\theta = \left.\frac{\partial R_s}{\partial k}\right|_h - \left.\frac{\partial R_s}{\partial h}\right|_k \cdot \frac{\left.\dfrac{\partial R_s}{\partial k}\right|_h - \dfrac{r\rho}{\sqrt{r_s^2 - [r(k\rho+1)]^2}}}{\left.\dfrac{\partial R_s}{\partial h}\right|_k - \dfrac{rk\dfrac{d\rho}{dh} + k\rho + 1}{\sqrt{r_s^2 - [r(k\rho+1)]^2}}} \quad . \tag{50}$$

The derivatives were obtained numerically by evaluating the refraction integral, Eq. (48), on an IBM 7090 computer for the various values required for the derivative. Therefore, by substituting Eqs. (48) and (50) into Eq. (7), the amount of dispersion can be measured in terms of the variation of refraction angle as a function of wavelength.

The intensity reduction due to differential refraction is defined as in Eq. (9):

$$\frac{I}{I_o} = \psi = \frac{1}{(1-D\dfrac{\partial R_s}{\partial h})(1-D\dfrac{R_s}{r})} \quad ; \tag{9}$$

and for

$$(1-D\frac{R_s}{r}) \sim 1.0; \quad \frac{DR_s}{r} \ll 1 \; ; \; r \cong r_e$$

Then

$$\psi \cong \frac{1}{(1-D\frac{\partial R_s}{\partial h})} \quad .$$ (51)

Again by expanding ψ about h_o for constant angle Θ, the intensity reduction as a function of wavelength can be expressed as

$$\psi(k,h) = \psi(k_o,h_o) + \frac{\partial \psi}{\partial k}\bigg|_\Theta \Delta k + \ldots \ldots , $$ (11)

and

$$\frac{\partial \psi}{\partial k}\bigg|_\Theta = \frac{\partial \psi}{\partial k}\bigg|_h - \frac{\partial \psi}{\partial h}\bigg|_k \cdot \frac{\partial \Theta / \partial k\big|_h}{\partial \Theta / \partial h\big|_k} \quad .$$ (12)

For the model atmosphere this derivative is

$$\frac{\partial \psi}{\partial k}\bigg|_\Theta = -\frac{D\frac{\partial}{\partial k}\left(\frac{\partial R_s}{\partial h}\right)}{\left[1+D\frac{\partial R_s}{\partial h}\right]^2} + \frac{D\frac{\partial^2 R_s}{\partial h^2}}{\left[1+D\frac{\partial R_s}{\partial h}\right]^2} \cdot \frac{\frac{\partial R_s}{\partial k} - \frac{r\rho}{\sqrt{r_s^2-[r(k\rho+1)]^2}}}{\frac{\partial R_s}{\partial h} - \frac{rk\frac{d\rho}{dh} + k\rho + 1}{\sqrt{r_s^2-[r(k\rho+1)]^2}}}$$ (52)

The intensity reduction due to differential refraction can be determined as a function of wavelength for a given tangent ray height by substituting Eqs. (51) and (52) into Eq. (11).

The intensity reduction due to molecular scattering can again be expressed as shown in Eq. (14) for the model atmosphere. The tangent ray height at which a ray of given wavelength passes through the atmosphere can be obtained as shown in Eqs. (15), (16), (17) and (18) for the isothermal atmosphere. Equation (18), the change in height for a ray of given wavelength for the model atmosphere, is

$$\Delta h = -\left\{\frac{\frac{\partial R_s}{\partial k}\bigg|_h - \frac{r\rho}{\sqrt{r_s^2-[r(k\rho+1)]^2}}}{\frac{\partial R_s}{\partial h}\bigg|_k - \frac{rk\frac{d\rho}{dh} + k\rho + 1}{\sqrt{r_s^2-[r(k\rho+1)]^2}}}\right\} \Delta k \quad .$$ (53)

58

Now the intensity reduction due to scattering is

$$\left[\frac{I(\lambda)}{I_o}\right]_s = e^{-\frac{32\pi^3}{3\lambda^4}k^2 m\left[\int_{-\infty}^{\infty}\rho ds\right]_{h_1}} . \tag{20}$$

The integral for the model atmosphere can be approximated by neglecting the curvature effects due to refraction and

$$M_a = \int_{-\infty}^{\infty}\rho ds = 2\int_{r_1}^{\infty}\frac{\rho(r)\ rdr}{\sqrt{r^2 - r_o^2}} . \tag{54}$$

Interpolating between data points in the model atmosphere, the density can be expressed as

$$\rho = \rho_i\ e^{\log(\rho_{i+1}/\rho_i)(\frac{r-r_i}{r_{i+1}-r_i})} \tag{55}$$

in the range

$$r_i \leq r \leq r_{i+1} .$$

Let

$$\alpha_i = \frac{1}{r_{i+1}-r_i}\ \log\ \left(\frac{\rho_{i+1}}{\rho_i}\right) \tag{56}$$

and

$$\eta = r - r_i . \tag{57}$$

Then,

$$M_a = 2\sum_{i=o}^{\infty}\rho_i\int_o^{r_{i+1}-r_i}\frac{(\eta+r_i)e^{\alpha_i\eta}d\eta}{\sqrt{r_i+r_o+\eta}\ \sqrt{r_i-r_o+\eta_o}} \tag{58}$$

By neglecting η in the numerator $(\eta+r_i)$, since $r_i \gg \eta$, and by neglecting η in $\sqrt{r_i+r_o+\eta}$, since $r_i+r_o \gg \eta$, Eq. (58) can be written as

$$M_a = 2 \sum_{i=0}^{\infty} \frac{\rho_i r_i}{\sqrt{r_i + r_o}} \int_0^{\Delta r_i} \frac{e^{\alpha_i \eta} \, d\eta}{\sqrt{(r_i - r_o) + \eta_o}} \quad . \tag{59}$$

The integral is of the type

$$\int_0^x \frac{e^{-\alpha t}}{\sqrt{\epsilon + t}} dt = 2 \int_{\sqrt{\epsilon}}^{\sqrt{\epsilon + x}} e^{-\alpha(u^2 - \epsilon)} \, du$$

$$= 2 e^{\alpha \epsilon} \left\{ \int_0^{\sqrt{\epsilon + x}} e^{-\alpha u^2} du - \int_0^{\sqrt{\epsilon}} e^{-\alpha u^2} du \right\} \quad , \tag{60}$$

with

$$\sqrt{\epsilon + t} = u \; ; \; \alpha = -\alpha_i \; ; \; x = \Delta r_i = r_{i+1} - r_i \; ; \; \epsilon = r_i - r_o \quad .$$

Therefore, the integrals can be evaluated in terms of the error function, and the integrated mass can be expressed as

$$M_a \cong 2 \sum_{i=0}^{\infty} \frac{\rho_i r_i}{\sqrt{r_i + r_o}} \cdot \sqrt{\frac{\pi}{-\alpha_i}} \left\{ \text{erf} \sqrt{-\alpha_i(r_{i+1} - r_o)} \right.$$

$$\left. - \text{erf} \sqrt{-\alpha_i(r_i - r_o)} \right\} e^{-\alpha_i(r_i - r_o)} \quad . \tag{61}$$

For numerical evaluation, Eq. (61) can be used when x, of erf (x), is < 3.0. For x > 3.0 the asymptotic expansion of erfc(x) is used

$$\text{erfc}(x) \to \frac{e^{-x^2}}{\sqrt{\pi} \, x} \left\{ 1 - \frac{.5}{x^2} + \frac{.75}{x^4} - \frac{1.875}{x^6} + \frac{6.5625}{x^8} - \ldots \right\} \quad . \tag{62}$$

With this expansion, the evaluation of this integrated mass is

$$M_a \cong 2 \sum_{i=0}^{\infty} \frac{\rho_i r_i}{\sqrt{-\alpha_i(r_i+r_o)}} \left\{ \frac{1}{\sqrt{-\alpha_i(r_i-r_o)}} \left(1 - \frac{.5}{-\alpha_i(r_i-r_o)} + \frac{.75}{\alpha_i^2(r_i-r_o)^2} \mp \dots \right) \right. $$

$$\left. - \frac{e^{\alpha_i(r_{i+1}-r_i)}}{\sqrt{-\alpha_i(r_{i+1}-r_o)}} \left(1 - \frac{.5}{-\alpha_i(r_{i+1}-r_o)} + \frac{.75}{\alpha_i^2(r_{i+1}-r_o)^2} \mp \dots \right) \right\} .$$

$$(63)$$

The intensity reduction due to molecular scattering can now be evaluated by

$$\left[\frac{I(\lambda)}{I_o} \right]_s = e^{-\frac{32\pi^3}{3\lambda^4} k^2 m \cdot \left[M_a \right]_{h_1}} .$$

$$(64)$$

The intensity reduction due to ozone is obtained in the same manner as in Section III A. Again the standard ozone density distribution is used and assumed to lie in uniform spherical layers around the earth. The ozone intensity reduction can be expressed as

$$\left[\frac{I(\lambda)}{I_o} \right]_{O_3} = e^{-k_{O_3}(\lambda) \left[\int_{-\infty}^{\infty} \rho_{O_3} ds \right]_{h_1}} = e^{-k_{O_3}(\lambda) \left[M_{O_3} \right]_{h_1}} ,$$

$$(24)$$

where $\left[M_{O_3} \right]_{h_1}$ is obtained from Eq. (30).

The stellar radiation energy reaching the top of the earth's atmosphere can be represented by Eqs. (31) and (32). The total energy received at the optical system of the satellite can now be expressed by Eq. (33). The energy distribution of the image as a function of wavelength and also refraction angles can be obtained in the manner given by Eqs. (34) through (37). Equation (38) represents the total energy over all wavelengths, while Eq. (39) represents the image center of gravity, and Eq. (47) gives the overall magnitude change as the star sets within the atmosphere.

Since the star image is dispersed over a band of refraction angles depending upon the wavelength considered, each ray will also have a particular tangent ray height h_1 corresponding to that wavelength. The optical tracking system used will most likely read the refraction angle corresponding to the center of gravity of the image. One must therefore determine the refraction angle, wavelength of the ray at the center of gravity, and the corresponding tangent ray height for a ray incident at the center of gravity of the instrument.

The refraction angle corresponding to a ray incident at the image center of gravity can be determined by

$$\overline{R_s} = R_s(k_o) + \overline{\Delta R_s} \tag{40}$$

and

$$\overline{R_s} = R_s(k_o) + \left.\frac{\partial R_s}{\partial k}\right|_\Theta \overline{\Delta k} + \ldots \tag{41}$$

Δk represents the deviation of the index of refraction between the standard ray considered in the expansion, λ_o, and the ray corresponding to the center of gravity, $\overline{\lambda}$.

$$\overline{\Delta k} = \frac{\overline{R_s} - R_s(k_o)}{\partial R_s/\partial k \big|_\Theta} \tag{42}$$

and also

$$\overline{\Delta k} = 1.663 \times 10^{-6} \left(\frac{1}{\lambda^2} - \frac{1}{\lambda_o^2} \right) . \tag{43}$$

Therefore, the wavelength of the ray incident on the center of gravity of the stellar image can be determined from

$$\overline{\lambda} = \sqrt{\frac{\lambda_o^2}{1 + \dfrac{\lambda_o^2 \, \overline{\Delta k}}{1.6636 \times 10^{-6}}}} . \tag{44}$$

The difference in height between the standard ray and λ_o and the center of gravity ray at $\overline{\lambda}$ is found by

$$\overline{\Delta h} = - \left\{ \frac{\left.\dfrac{\partial R_s}{\partial k}\right|_h - \dfrac{r\rho}{\sqrt{r_s^2 - [r(k\rho+1)]^2}}}{\left.\dfrac{\partial R_s}{\partial h}\right|_k - \dfrac{k\rho\dfrac{d\rho}{dh} + k\rho + 1}{\sqrt{r_s^2 - [r(k\rho+1)]^2}}} \right\} \overline{\Delta k} . \tag{65}$$

The height above the surface corresponding to the ray $\overline{\lambda}$ is

$$\overline{h} = h_o + \overline{\Delta h} , \tag{46}$$

62

where h_0 = tangent ray height corresponding to the standard ray at λ_0. Equation (47) in Section III A can be used to calculate the decrease in photocathode magnitude for various tangent ray heights in the model atmosphere.

Results

The analysis was performed for two separate photocathode materials: the S-20, whose characteristics described in Section III A, and a Westinghouse experimental S-20, with the spectral response shown in Fig. 29. The same parameters outlined in Section III A, with the exception of density, were used for the analysis of the model atmosphere. Figures 30-32 show the resulting photocathode images for the various tangent ray heights during occultation on the Westinghouse experimental S-20. The images for the S-20 used in Section III A are not presented, but the photocathode magnitude change as a function of tangent ray height for both photocathodes are shown for comparison in Fig. 37.

The photocathode images in the model atmosphere are similar to the images obtained from the isothermal atmosphere and display the characteristic shift in the center of gravity as the tangent ray height decreases. This shift in the center of gravity is shown in Fig. 33 for the S-20 and the Westinghouse experimental S-20, and it occurs for the same reason as explained in Section III A.

Figure 34 shows the stellar transmission through the model atmosphere as a function of the tangent ray height due to differential refraction. The increase of stellar transmission occurring at 5 km due to differential refraction occurs because of the nature of the model atmosphere, where the sharp increase in the temperature between 10 km and 5 km eventually results in a change of the derivatives used in Eq. (52). These changes are reflected as a slight increase in transmission at 5 km. Figure 35 shows the intensity reduction due to molecular scattering as a function of tangent ray height and wavelength for the model atmosphere.

Figure 36 shows the height difference, at various tangent ray heights, between the base ray at λ_0 and rays of different wavelength λ. The height difference occurs because the refraction angle at any tangent ray height is a function of the wavelength. Since all rays converge at the satellite, the rays of different wavelength have different tangent ray heights, as shown in Fig. 10. By restricting the spectral waveband, control over the tangent ray height difference and photocathode image spread may be obtained.

Figure 37 shows the decrease in photocathode magnitude as a function of tangent ray height for both photocathode materials. The results obtained from the isothermal atmosphere analysis are also plotted; very close agreement between the two atmospheres occurs down to a tangent ray height of 10 km. Departures in photocathode magnitude are due to the increased density in the lower part of the isothermal atmosphere, where a surface density of 1.99
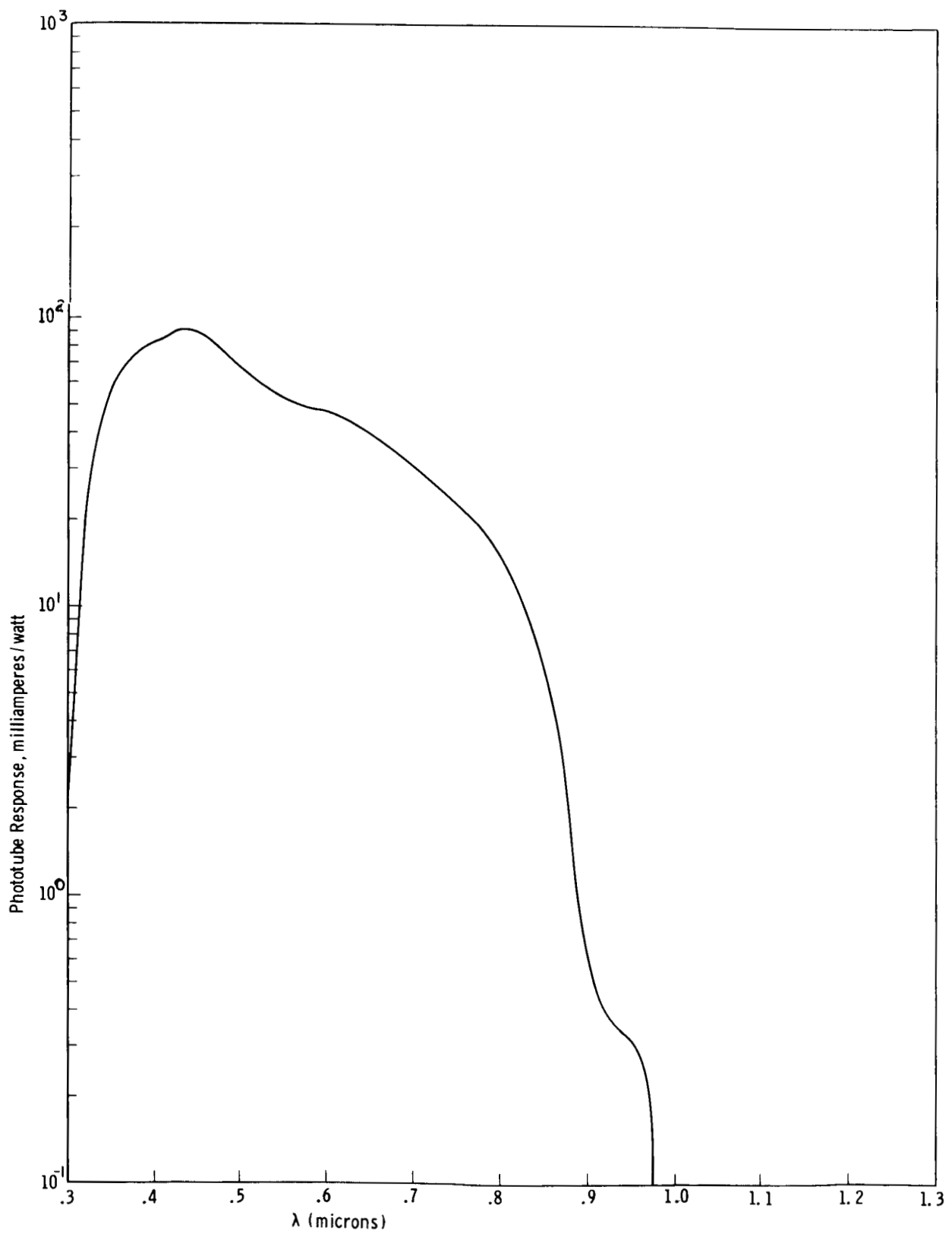
Fig. 29.   Spectral response of the Westinghouse Experimental S-20.
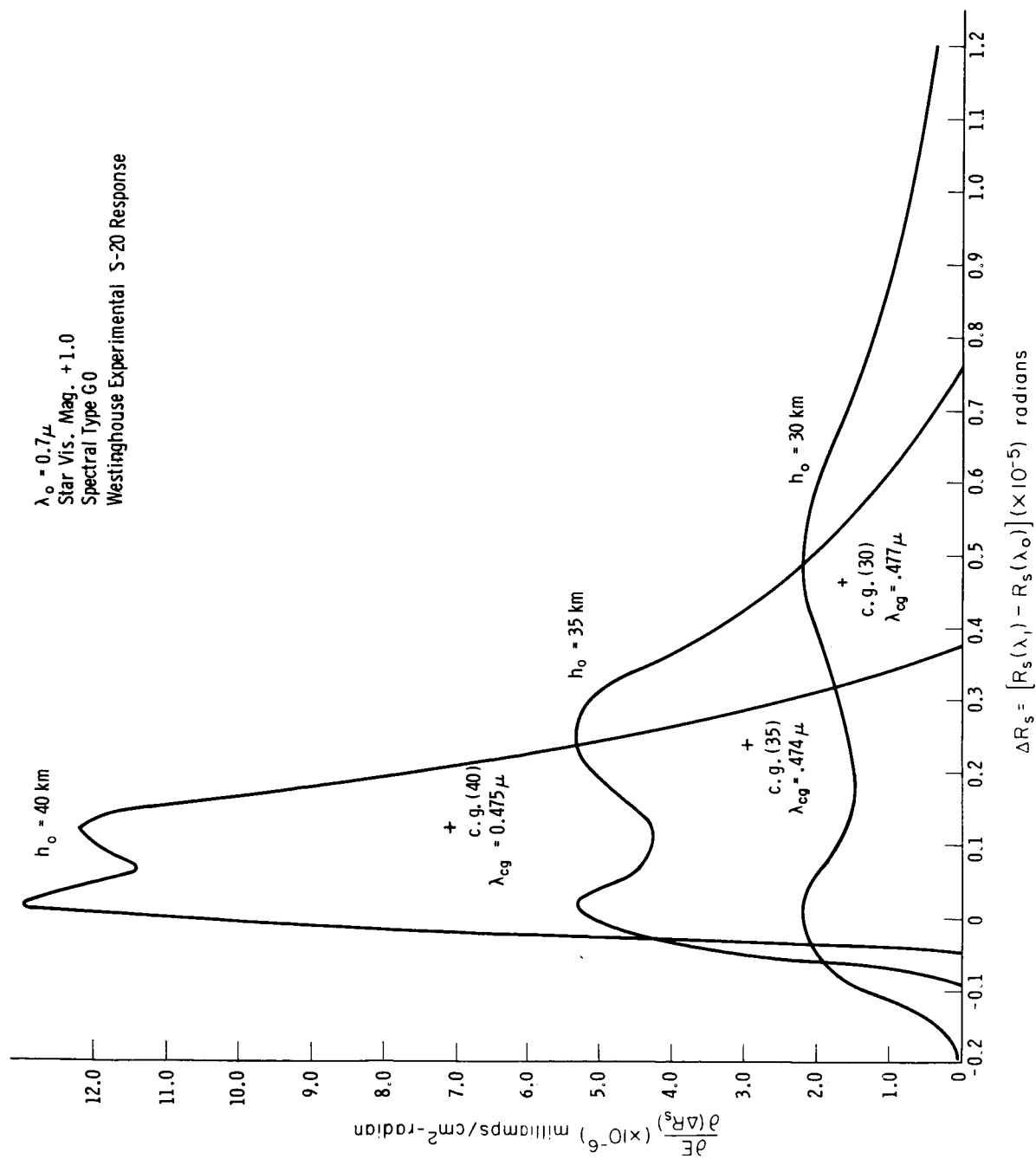
Fig. 30. Energy distribution and center of gravity for photocathode images at tangent ray heights 40 km-30 km in the analytic model atmosphere (S-20 response).
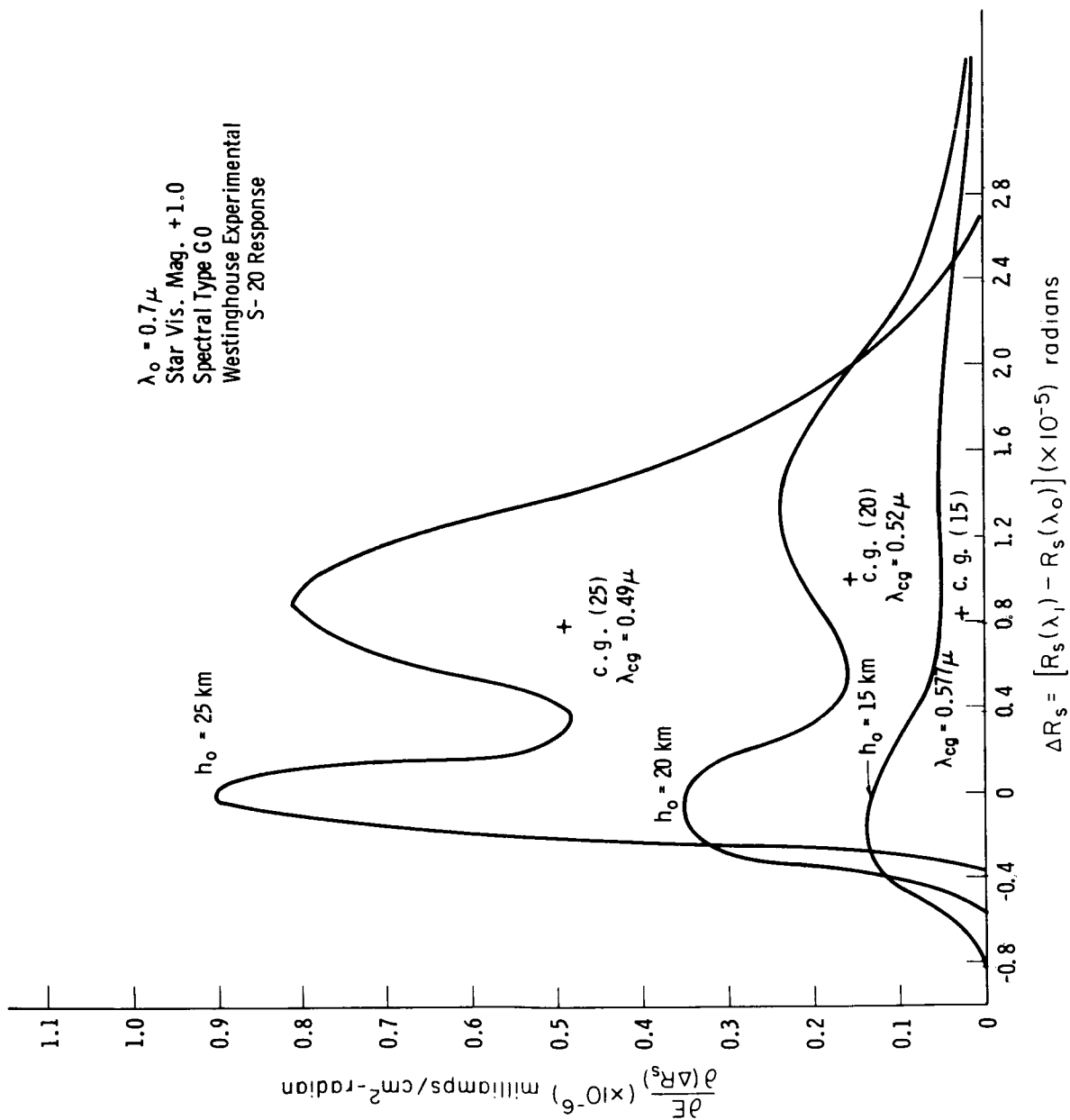
Fig. 31. Energy distribution and center of gravity for photocathode images at tangent ray heights 25 km–15 km in the analytic model atmosphere (S–20 response).

λₒ • 0.7
Star Vis. Mag. + 1.0
Spectral Type G0
Westinghouse Experimental
S-20 Response

$h_o = 10$ km

$h_o = 5$ km

+
c. g. (10)
$\lambda_{cg} = 0.625 \mu$

c. g. (5)
+ $\lambda_{cg} = 0.707 \mu$

$\Delta R_s = [R_s(\lambda_1) - R_s(\lambda_o)] (\times 10^{-5})$ radians

$\frac{\partial E}{\partial (\Delta R_s)} (\times 10^{-6})$ milliamps/cm²-radian

.048
.044
.040
.036
.032
.028
.024
.020
.016
.012
.008
.004
0

-2.0 -1.6 -1.2 -0.8 -0.4 0 0.4 0.8 1.2 1.6 2.0 2.4 2.8 3.2 3.6
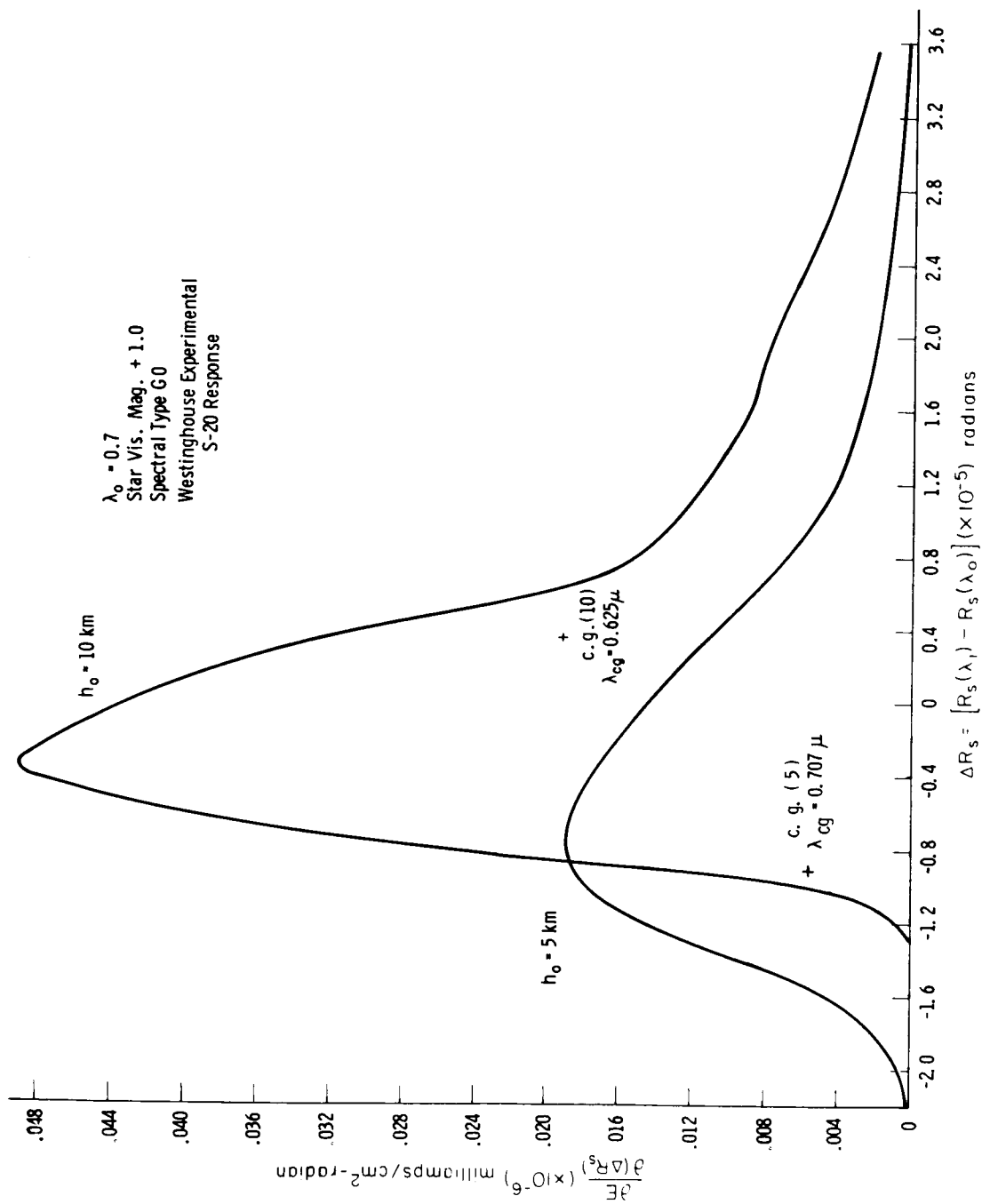
Fig. 32. Energy distribution and center of gravity for photocathode images at tangent ray heights 10 km and 5 km in the analytic model atmosphere (S-20 response).

67
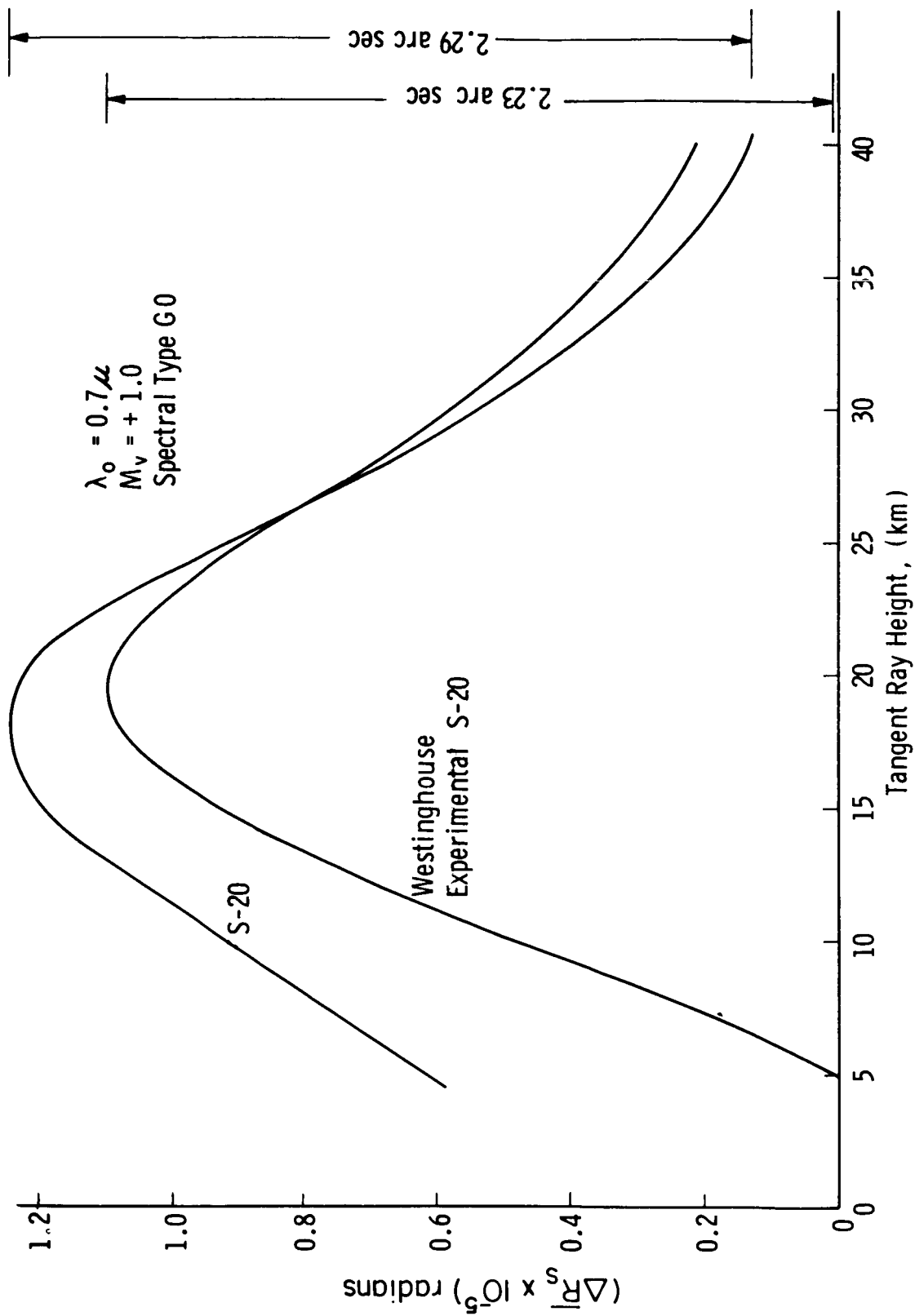
Fig. 33. Shifting of photocathode image center of gravity during scan by the S-20 and Westinghouse Experimental S-20, for the analytic model atmosphere.
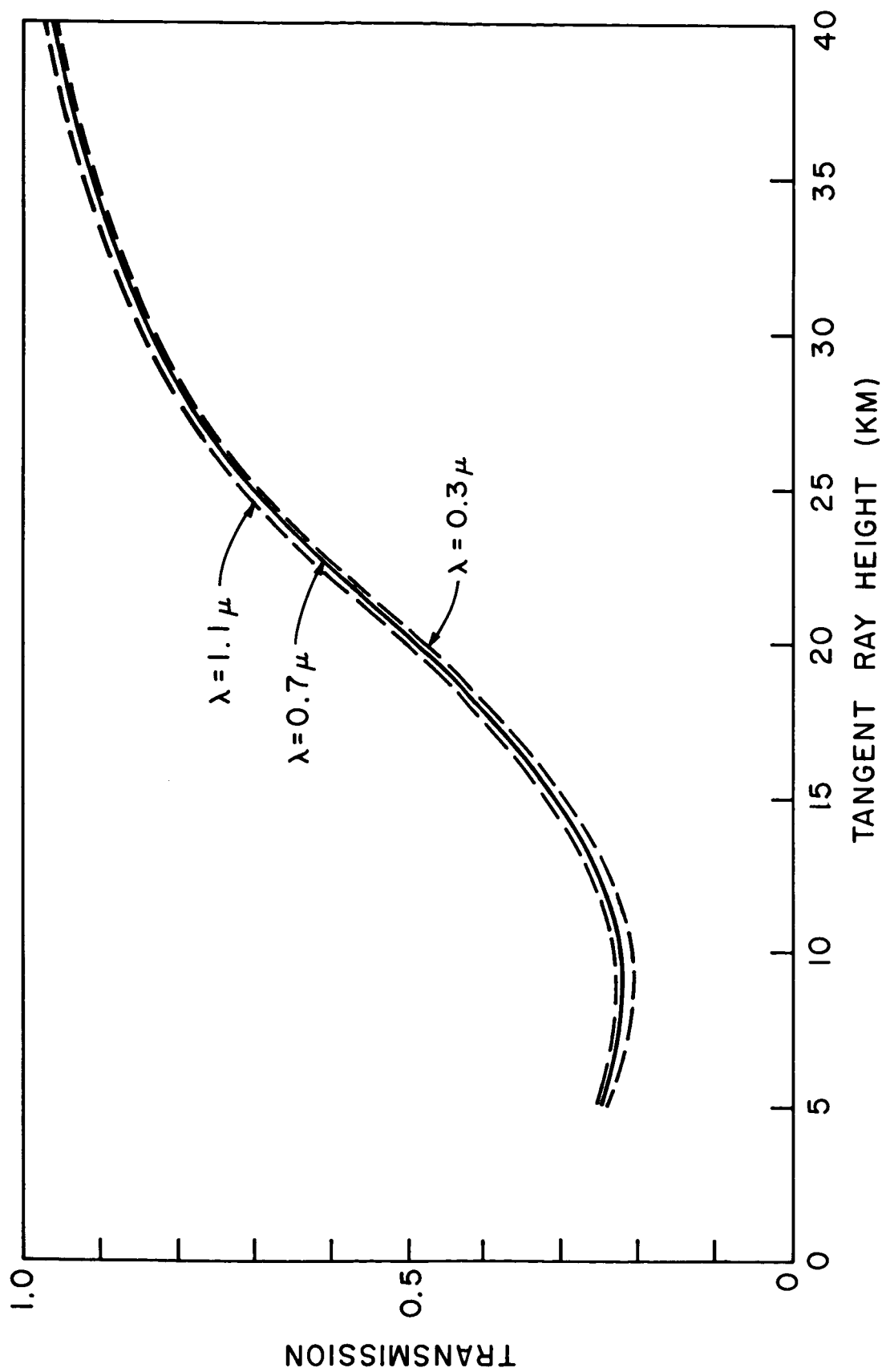
Fig. 34. Intensity reduction due to differential refraction in an analytic model atmosphere.
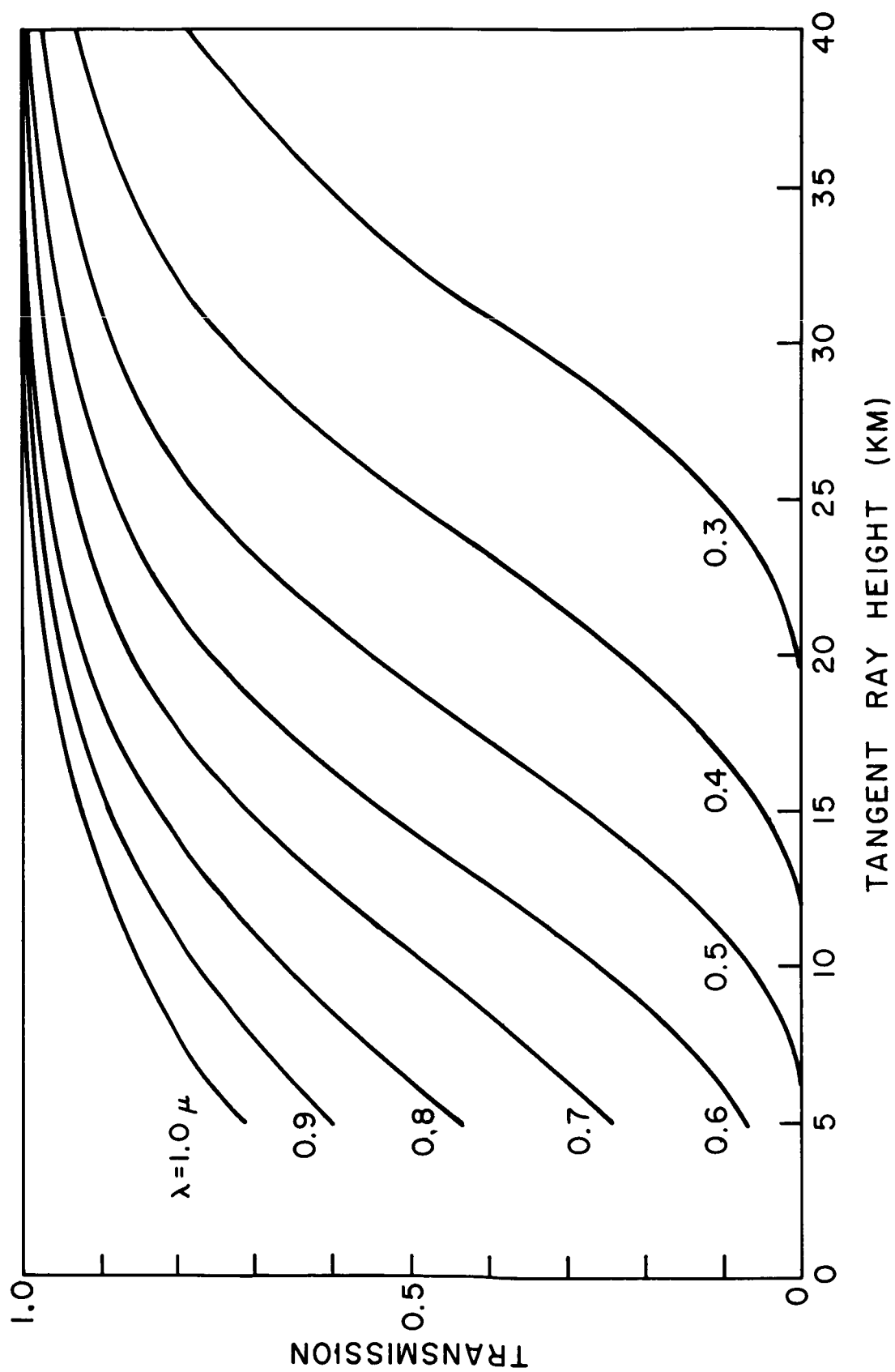
Fig. 35. Intensity reduction due to molecular scattering in an analytic model atmosphere.

70
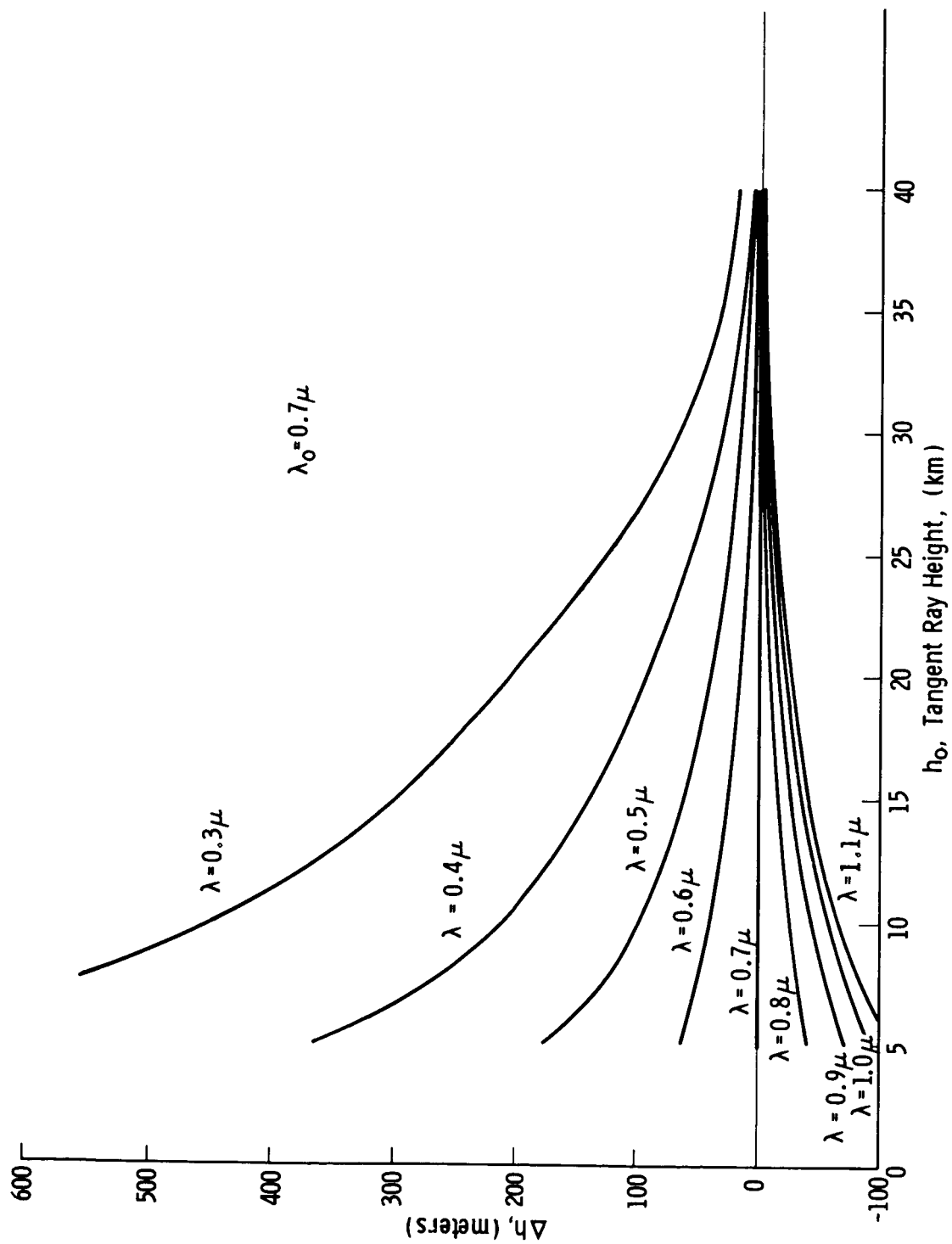
Fig. 36. Height difference between base ray λ_o and ray corresponding to wavelength λ for various tangent ray heights in the analytic model atmosphere.
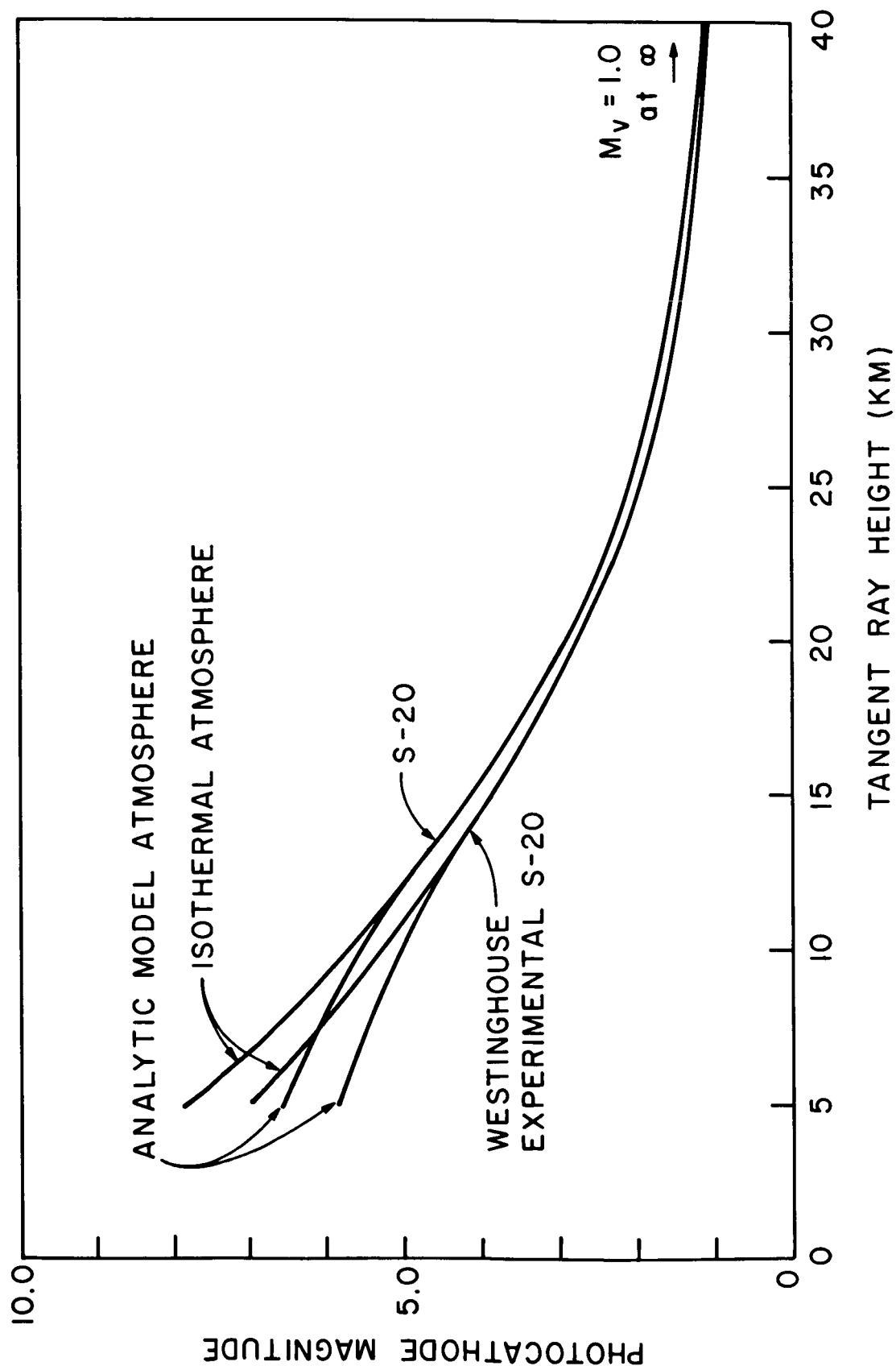
Fig. 37. Photocathode magnitude as a function of tangent ray height for the S-20 and Westinghouse Experimental S-20. The initial photocathode magnitude of +1.0 is arbitrarily assigned equal to +1.0 visual magnitude. The spectral type is GO.

72

kg/m³ is used. Therefore, the analytic approach used in the isothermal atmosphere may be used to a tangent ray height of 10 km, whereas the approach outlined in Section III B should be used in defining the star characteristics from 10 km until occultation.

The image energy distribution curves for the Westinghouse experimental S-20 given in Figs. 30-32, and the corresponding image center of gravity shift in Fig. 33, and photocathode magnitude decreases in Fig. 37 again summarizes the important parameters which define the image characteristics to be used in the design of a star-tracker.

IV. AN ANALYSIS OF BACKGROUND NOISE

The background noise consists essentially of four components: (1) stellar radiation and galactic light, (2) zodiacal light, (3) airglow emissions, and (4) auroral emissions.

The amount of galactic and zodiacal light appearing in the background will be variable, depending upon the direction of observation. Galactic starlight will be brightest in the plane of the Milky Way, whereas zodiacal light is brightest in the plane of the ecliptic. The aurora and airglow emissions, on the other hand, can vary with time as well as with the direction of observation, and a large range of intensity variations may be expected. Each component of the background noise will now be examined separately in order to arrive at a spectral energy distribution in the spectral region of expected photocathode operation, 0.3-0.975 microns.

In the design of the star-tracker, one of the necessary parameters to be determined is the expected range of the signal-to-noise ratio. At the lower limit, a short time after sunset when most of the background is scattered sunlight, signal-to-noise ratios of unity or less can be expected. Since the expected signal strength has already been determined in a previous section, the upper limit of the signal-to-noise ratio is obtained when the contributions due to each background noise component are minimum. For galactic and zodiacal light, the minimum is obtained by having the star-tracker field of view encompass the darkest region of the galactic sphere. The minimum contributions due to the airglow and aurora are more difficult to obtain, due to the lack of observational data of these phenomena as seen from space. However, with the aid of certain assumptions and ground based zenith spectral radiance measurements, one can obtain some representative values for the airglow and aurora emissions as they would appear at an orbiting spacecraft.

A. STELLAR BACKGROUND

Roach and Megill[15] performed calculations giving the total integrated starlight over the entire sky based on the star counts in "Groningen" Pub. No. 43. The results are given in both the photographic and visual magnitude scales in tabular and graphical form as a function of the galactic coordinates.

Since the S-20 photocathode operates in the visible and near-infrared, we had to extend the results of Roach and Megill to obtain the spectral energy distribution from 0.3 to 0.975 microns. In order to obtain the spectral energy distribution we had to assume that the energy radiated from a given portion of the sky follows the black body distribution. Since the photographic and

visual magnitude intensities are given by Roach and Megill, a color index of a given region on the galactic sphere may be obtained from

$$C.I. = 1.086 \ln \left(\frac{z}{z^1}\right) , \tag{66}$$

where

z = number of 10th visual magnitude stars/$\hat{\min}^2$

z^1 = number of 10th photographic magnitude stars/$\hat{\min}^2$

The effective black body temperature for the region may now be obtained from

$$T_e = \frac{8200.}{C.I. + 0.68} . \tag{67}$$

The number of 10th visual magnitude stars/deg^2 can be converted to a single star/deg^2 of magnitude:

$$m_{zv} = 10. + 1.086 \ln \left(\frac{1}{z}\right) . \tag{68}$$

The effective irradiance I_0, in watts/cm^2, in the visible portion of the spectrum of a star of visual magnitude zero is, according to Ramsey[13], 3.1×10^{-13} watts/cm^2. Therefore, the irradiance of a single star of visual magnitude m_{zv} in the visible portion of the spectrum is

$$I = 3.1 \times 10^{-13} e^{-\frac{m_{zv}}{1.086}} . \tag{69}$$

The efficiency of radiation of a black body at a temperature T_e over the visible region is given by

$$\eta_e(t) = \frac{\int_0^\infty \omega_\lambda(T) \, s(\lambda) \, d\lambda}{\int_0^\infty \omega_\lambda(T) \, d\lambda} , \tag{70}$$

where $\omega_\lambda(T)$ = Planck black body function at wavelength λ; $s(\lambda)$ = fractional response of the eye at wavelength λ.

The peak intensity of the black body at a temperature T_e can now be found from

$$H_{\lambda \; peak} = \frac{I(m_{zv})}{\eta_e(T)} \; \frac{\omega_{\lambda \; max}(T)}{\int_0^\infty \omega_\lambda(T) \; d\lambda} \; , \qquad (71)$$

where

$$\omega_{\lambda \; max}(T) = \text{maximum value of the Planck function,}$$

$$(1.290 \text{ X } 10^{-15}T^5) \quad ^{watts}/cm^2 - \mu \; ,$$

and

$$\int_0^\infty \omega(T)d\lambda = 5.679 \text{ X } 10^{-12}T^4 \; , \quad ^{watts}/cm^2 \; . \qquad (72)$$

Since the Planck function at temperature T_e can be matched to the peak intensity $H_{\lambda \; peak}$, the intensity at any wavelength can be obtained from

$$H(\lambda,T) = \frac{2.0421 \text{ X } 10^{-17}}{\eta_e(T)} \; e^{-\frac{m_v}{1.086}} \; \frac{T}{(\lambda T)^5 \; (e^{\frac{1.438}{\lambda T}} -1)} \; . \qquad (73)$$

The total intensity of the spectral region of interest can be obtained by integrating Eq. (73) over the region:

$$B(T) = \int_{\lambda_1}^{\lambda_2} H(\lambda,T)d\lambda \; . \qquad (74)$$

A later section will show that the contribution of stellar background, although 40-50% of the total observed in the zenith from the ground, will be negligible when the horizon is viewed from the spacecraft due to the increased airglow background. The airglow background will appear brighter because of the increased path length within the airglow. Therefore, although the color index and effective radiating temperature may vary slightly in different portions of the galactic sphere, the error in the total background made by assuming an average radiating temperature over the galactic sphere is small.

The number of 10th visual magnitude stars/deg^2 given by Roach and Megill can be converted to watts/cm^2 - min^2 over the spectral range 0.3-0.975 microns for an average effective radiating temperature of 5500°K by multiplying the data of Roach and Megill by 5.2 X 10^{-2}.

B. ZODIACAL LIGHT

Elvey and Roach[5] have calculated the distribution of zodiacal light of the entire sky in ecliptic coordinates and have presented the results graphically as the number of 10th photographic magnitude stars/deg^2. Since zodiacal light is generally believed to be sunlight scattered by interplanetary dust, its spectral energy distribution is the same as the energy distribution of the sun. The effective temperature of the sun is 6000°K, giving a color index of +0.57. Because the color index is constant throughout the entire sky, a conversion factor can be applied directly to obtain the energy radiated between the 0.3-0.975 micron region. This is based on the assumption that zodiacal light has the same black body spectral distribution as the sun over the wavelengths of interest. With this assumption, the spectral energy distribution may be obtained in a manner similar to the method described in the Stellar Background Section by using the data presented by Roach. The intensity given in number of 10th photographic magnitude stars/deg^2 can be converted to a single star of photographic magnitude m_{zp} in one square degree by

$$m_{zp} = 10 + 1.086 \ln \left(\frac{1}{z^1}\right) , \qquad (75)$$

where z^1 = number of 10th photographic magnitude stars/m$\hat{\text{i}}$n^2

This corresponds to a single star of visual magnitude

$$m_{zv} = m_{zp} - C.I. \qquad (76)$$

The visual efficiency $\eta_e(T)$ for a black body radiating at 6000°K is 0.128; therefore the spectral energy distribution can be approximated by

$$H(\lambda) = \frac{9.572 \times 10^{-9} e^{-\frac{m_{zv}}{1.086}}}{(\lambda \cdot 6000)^5 (e^{\frac{1.438}{\lambda \cdot 6000}} - 1)} , \qquad (77)$$

where

$$\lambda = \text{wavelength in cm} .$$

The intensity of the wavelength region of S-20 photocathode sensitivity, 0.3-0.975 microns, is

$$B = \int_{\lambda_1}^{\lambda_2} H(\lambda) \, d\lambda . \qquad (78)$$

If Roach's data giving the number of 10th photographic magnitude stars/deg^2 are multiplied by 7.8×10^{-2} to obtain watts/$\text{cm}^2 - \hat{\text{min}}^2$, the zodiacal light data are made consistent with the stellar background data in the 0.3-0.975 micron band.

C. AIRGLOW EMISSION

The airglow brightness, as viewed from an orbiting spacecraft, will vary with the direction of observation and with time. It is impossible to consider all brightness ranges, and there do not appear to be sufficient data to determine an average spectral energy distribution as a function of tangent ray height, as shown in Fig. 38. In addition, the numerous emission lines appearing in the airglow region over the wavelengths of interest complicates the problem of airglow background analysis considerably. To obtain an approximate value of the airglow background intensity for a preliminary star-tracker analysis, one must use a number of simplifying assumptions. These assumptions are:

(1) The emissions at all wavelengths under consideration, 0.3-1.0 microns, occur in a relatively narrow band between 80-120 km and have the same distribution as the continuum given in Ref. (11) and shown in Fig. 39.

(2) The airglow is confined to uniform spherical layers around the earth.

(3) The spectral energy distribution observed on the ground I_g, is the same as that observed in space, except greater by a geometry factor of I/I_g.

(4) The average zenith night sky spectral distribution consists of light due to the following sources:

   (a) starlight and galactic light   50%

   (b) zodiacal light   10%

   (c) airglow   40%

   (d) aurora   variable

   Therefore, 40% of a typical night sky spectral energy distribution, as shown in Fig. 40, and determined by the U. S. Army Engineering Research and Development Laboratory, Fort Belvoir, Va., will represent an airglow continuum as observed from the ground.

(5) The continuous distribution presented includes line emissions over the wavelength regions under consideration.
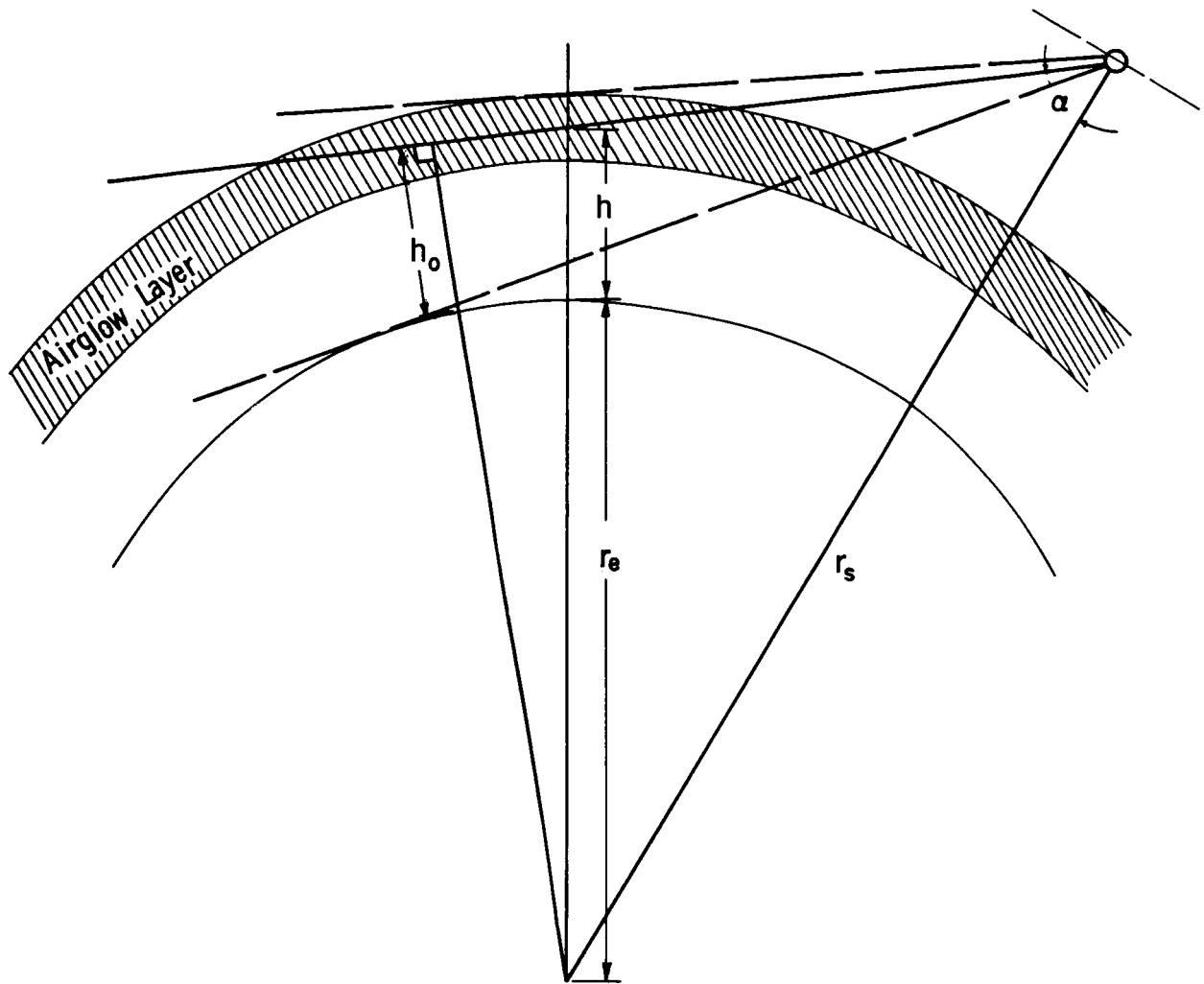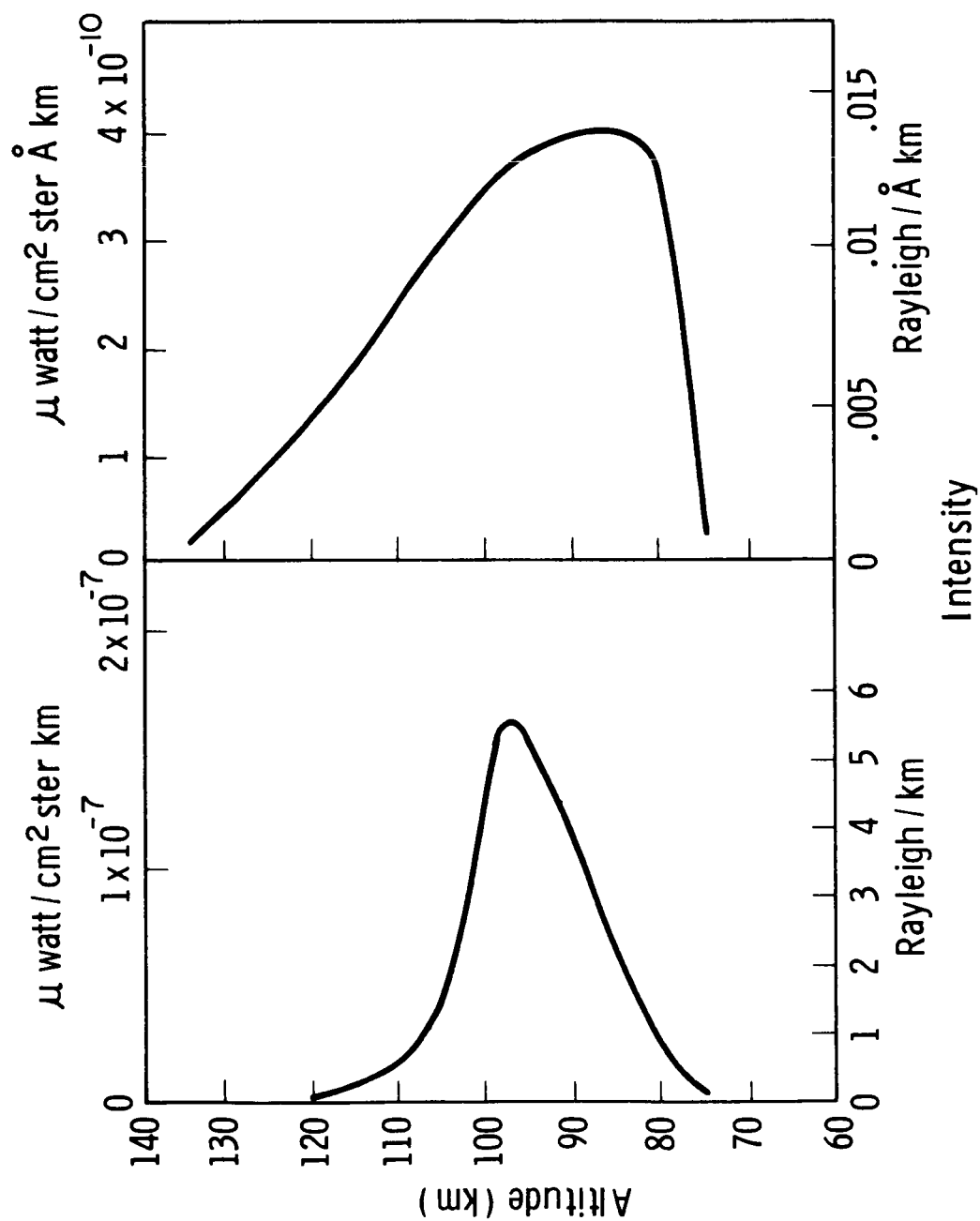
78

Fig. 38. Airglow layer as seen from space.

Fig. 39. Vertical distribution of night-airglow intensity for the 5577 Å oxygen emission and for the green continuum emission sampled at 5420 Å., from Koomen et al. [11]
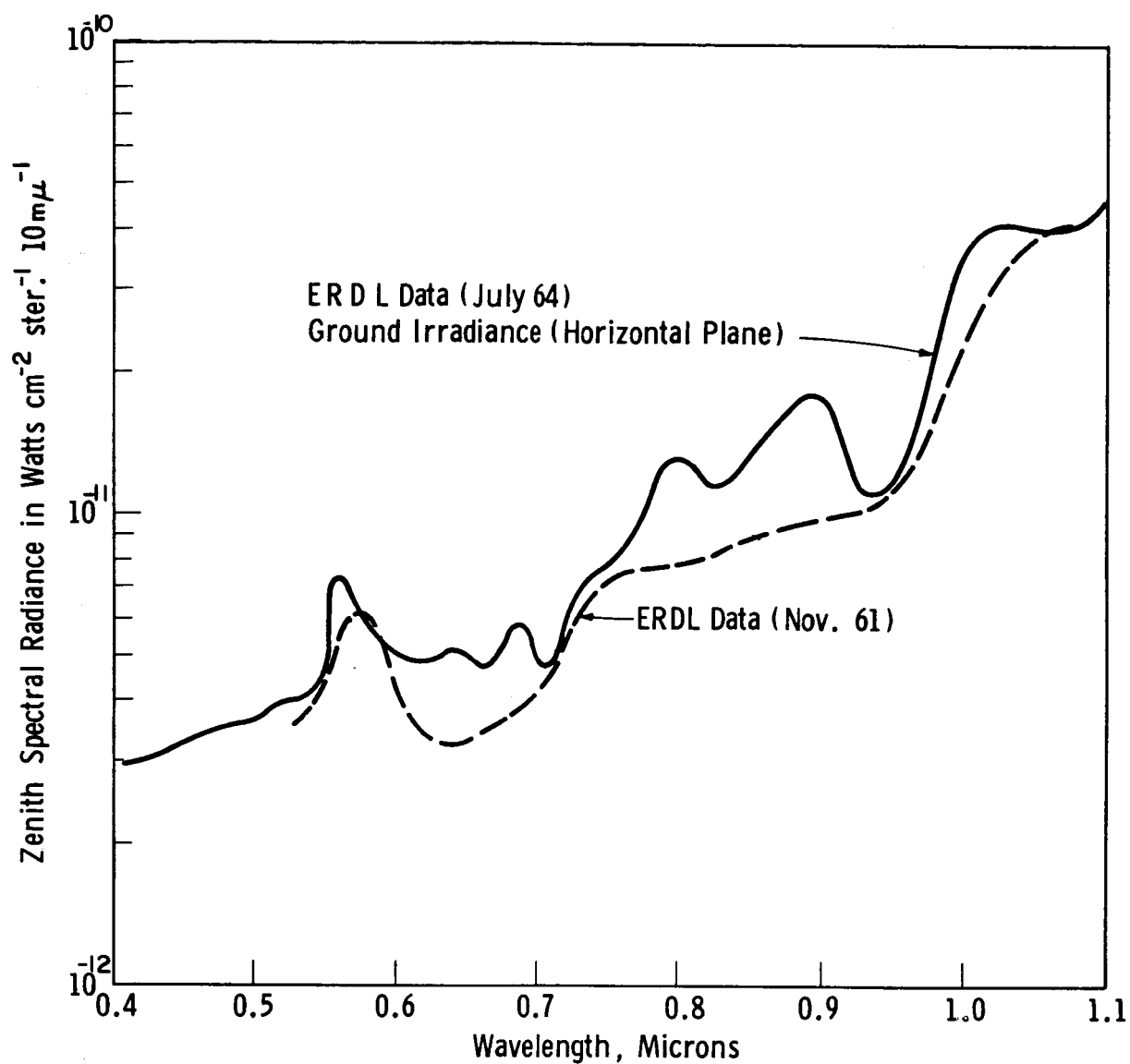
Fig. 40. Typical night sky spectral energy distribution.

Although the actual spectral energy distribution due to the airglow may vary from the assumed distribution, the deviations are not expected to be so large that the assumed distribution will lie outside the expected intensity variation band.

The airglow layer as observed from space appears brighter than the ground-based zenith airglow because of the geometry involved, as shown in Fig. 38. The intensity will, therefore, be a function of the angle, α. If the airglow emission rate of the continuum is known as a function of the height above the earth's surface, $F(r)$, in Rayleighs/$\overset{\circ}{A}$-km, the intensity of the airglow layer as seen from space may be calculated. Figure 41 shows the geometry of the situation, and the total number of photons emitted at a distance r to $r + dr$ and intercepted by the photometer is,

$$\frac{A}{4\pi r^2} \, r^2 \Omega \, F_\nu(r) dr \quad , \tag{79}$$

where A = photometer sensitive area, Ω = photometer field of view, and
      r = distance of photometer to the element.

The specific photonflux entering the photometer is

$$F_\nu = A\Omega \, \frac{1}{4\pi} \int_0^\infty F_\nu(r) dr \quad . \tag{80}$$

The specific intensity is now

$$I_\nu = \frac{F_\nu}{A\Omega} = \frac{1}{4\pi} \int_0^\infty F_\nu(r) dr \quad . \tag{81}$$

It can also be expressed in terms of emissions from a column, in units of Rayleighs/$\overset{\circ}{A}$, as

$$4\pi \, I_\nu = \int_0^\infty F(r) dr \quad . \tag{82}$$

This integral was evaluated for various nadir angles in the interval of tangent ray heights corresponding at one limit to zero, and at the other limit to 120 km, the top of the airglow layer. The intensity $I(\alpha)$ of the continuum emission is shown in Fig. 42 as a function of α and seen from a satellite at 1100 km. The ratio of the intensity as seen from space to the intensity as seen from the ground, I/I_g, is shown in Fig. 43 for a satellite at 1100 km. One can now determine the flux entering a photometer from the airglow background

Airglow
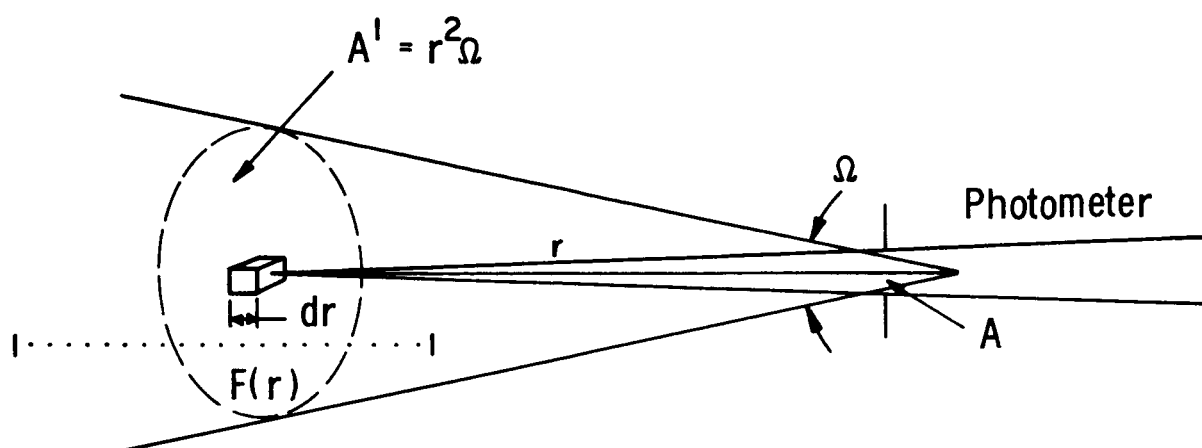
F (r) = distribution of rate of emission (photons / cm^3 - sec)
Ω = photometer field of view (steradians)
A = photometer sensitive area (cm^2)

Fig. 41. Geometry of airglow emission.

Fig. 42. Airglow intensity near 5400 Å due to continuum emission, as viewed from a satellite at 1100 km.

Fig. 43. Airglow intensity ratio due to continuum emission.

85

at a given nadir angle, α, by specifying the photocathode area and integrating the airglow intensity over the photometric field of view.
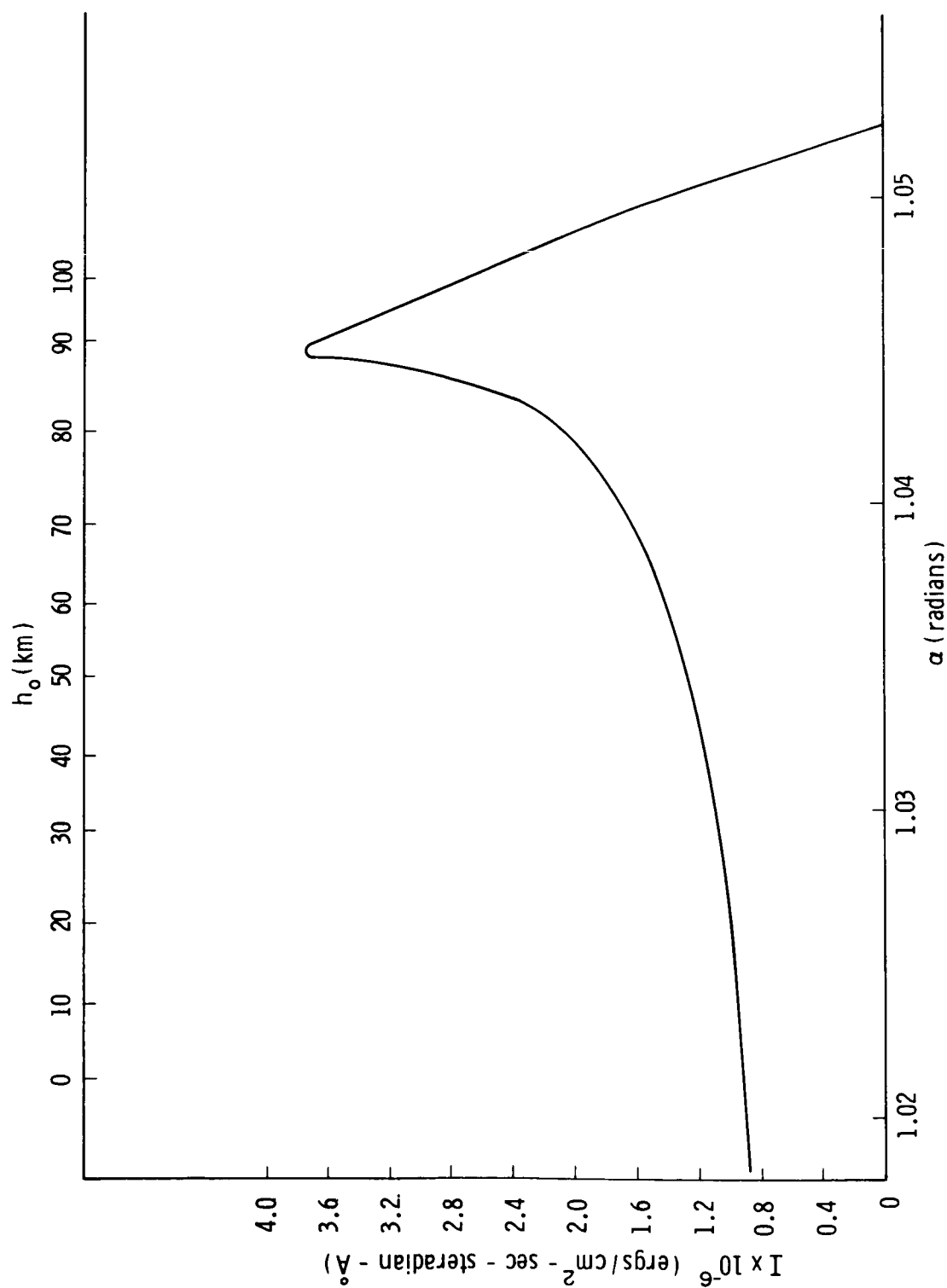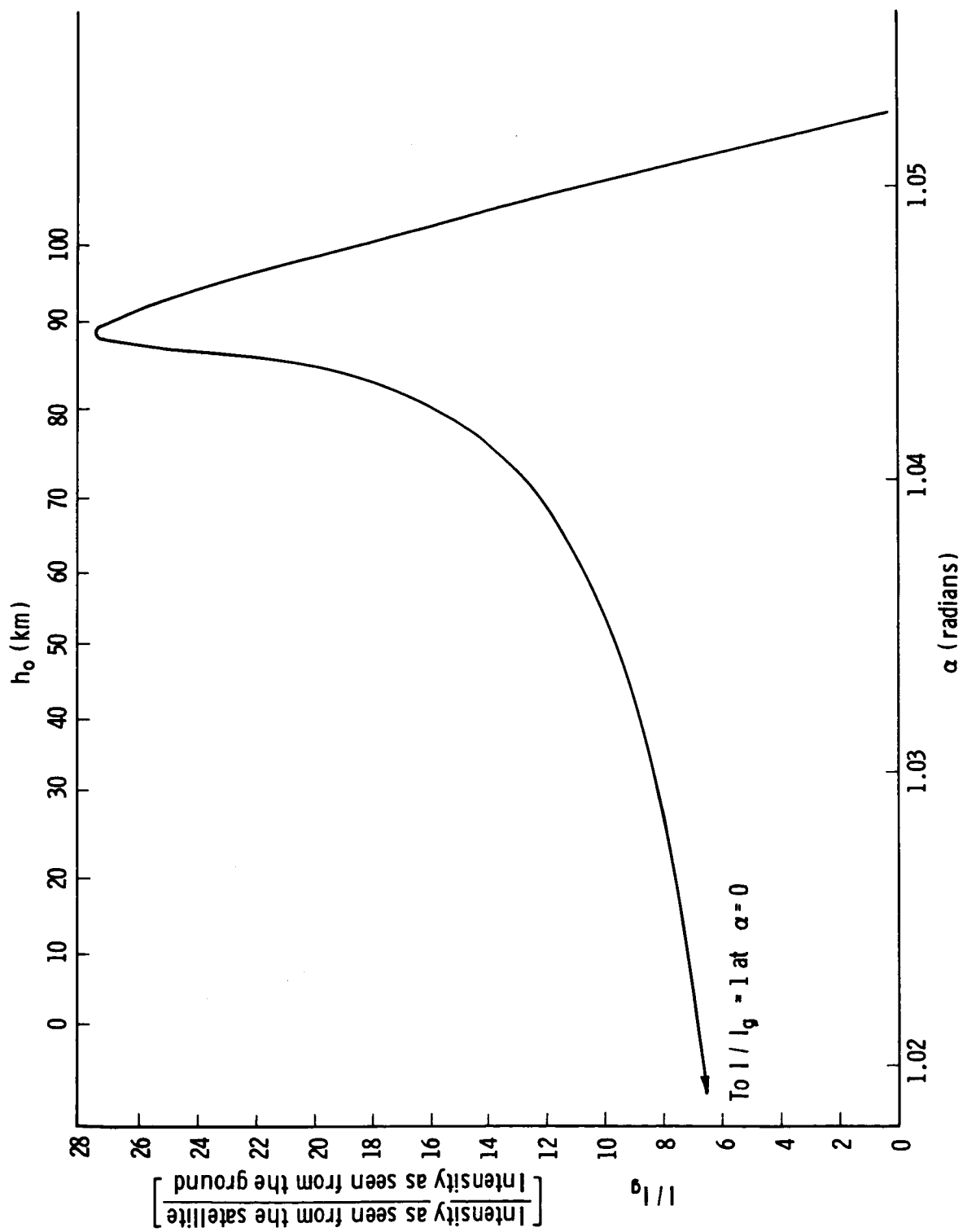
D. AURORAL EMISSION

Although the background attributed to the aurora may be large during certain times, and may contribute significantly to the star-tracker background, only the minimum background is desired at present. The minimum will occur when the aurora is not present within the field of view, as may be the case when the star-tracker is observing stars in the vicinity of the equator. Therefore, the auroral background is not considered to contribute to the background at the maximum signal-to-noise ratio position.

E. SCATTERED MOONLIGHT

Although scattered moonlight may contribute to the background, the maximum signal-to-noise ratios will occur when the moon is not visible from the satellite. It is, therefore, not considered to contribute to the background under the conditions for maximum signal-to-noise ratio.

F. MINIMUM BACKGROUND

The minimum background will appear when the field of view of the photometer encompasses the darkest portion of the galactic sphere and no aurora appears. In this situation, the bulk of the background consists of the airglow. If 40% of the intensity of the zenith night sky, shown in Fig. 40, is due to airglow, then the integrated intensity from 0.3 to 0.975 microns is 1.969×10^{-10} watts/cm^2 - steradian. The ratio of I/I_g at the peak in Fig. 43 for the continuum emission is 28.5. The ratio agrees with the observed values obtained in NRL rocket flights in Ref. 11. The intensity near 5500 Å is 2.0×10^{-10} watts/cm^2 - sterad - μ, and if this value is multiplied by the $(I/I_g)_{max}$ ratio of 28.5, the observed intensity is 1.71×10^{-9}, which corresponds to 4400-10th visual magnitude stars/deg^2. This value is reasonably close to the 3000-10th visual magnitude stars/deg^2 viewed by Cooper et al.,[7] considering the variable nature of the airglow intensities; the airglow observed by Cooper et al.[7] was less bright then the average observed values.

The vertical distribution of the 5577-Å oxygen green line from Ref. 11 is shown in Fig. 39. This corresponds to 2.913×10^{-5} ergs/sec - cm^2 - steradians, as measured from the ground. From geometry and the vertical distribution given, the value of $(I/I_g)_{max}$ is 39, giving a calculated intensity observed

from space of 113.6×10^{-5} ergs/sec - cm^2-steradian. This agrees reasonably well with the value of 160×10^{-5} ergs/sec - cm^2 - steradian observed by the NRL rocket flights.

If, for example, the minimum background at 40 km tangent ray height is desired, it can be found in the following manner. I/I_g at 40 km, from Fig. 43, is 8.8, giving an observed airglow intensity of 1.738×10^{-9} watts/cm^2 - steradian.

Therefore, the minimum background in the spectral range 0.3-0.975 microns for the assumed airglow spectral distribution is

<div align="center">

MINIMUM BACKGROUND

</div>

airglow 144.34×10^{-18} watts/cm^2-$\hat{min}^2$

stellar background 1.19×10^{-18} watts/cm^2-$\hat{min}^2$ (27-10th visual magnitude stars/ deg^2)

zodiacal light 2.30×10^{-18} watts/cm^2-$\hat{min}^2$ (50-10th visual magnitude stars/ deg^2)

_____

total 147.83×10^{-18} watts/cm^2-$\hat{min}^2$

This value will establish a minimum noise level. Since the signal strength has been calculated previously, the maximum signal-to-noise ratio is now established. The minimum signal-to-noise ratio is unity or less; therefore the expected range of signal-to-noise ratio of the star-tracker is established for orbtial conditions.

Another approach in determining the airglow intensity is to consider the mean zenith sky background given by Allen[1] as 400-10th visual magnitude stars/ degree². If 50% of the mean night sky background is due to integrated starlight, then the intensity of starlight, e.g., 200-10th visual magnitude stars/deg^2, at an effective black body temperature of $5500^{\circ}K$, will be 9.21×10^{-18} watts/ cm^2-$\hat{min}^2$ in the spectral range of 0.3-0.975 microns. Ten percent of the mean night sky background is zodiacal light, and the intensity of 40-10th visual magnitude stars/deg^2, at the effective black body of the sun, e.g., $6000^{\circ}K$, is 1.848×10^{-18} watts/cm^2-$\hat{min}^2$ from 0.3 to 0.975 microns. The integrated night sky background in the S-20 spectral range of Fig. 40 is 4.10×10^{-17} watts/cm^2-$\hat{min}^2$. Therefore, the difference of the sky background given in Fig. 40, and starlight and zodiacal light calculated above, can be attributed to airglow in the absence of any visible aurora.

The intensity of the background seen from space at a tangent ray height of 40 km and spectral range of 0.3-0.975 microns is

MINIMUM BACKGROUND

airglow	263.55×10^{-18} watts/cm^2-$\hat{min}^2$
stellar background	1.19×10^{-18} watts/cm^2-$\hat{min}^2$
zodiacal light	2.30×10^{-18} watts/cm^2-$\hat{min}^2$
total	267.04×10^{-18} watts/cm^2-$\hat{min}^2$

Therefore stellar background and zodiacal light can be neglected without serious error in calculating the sky background as seen from space at various tangent ray heights.

V.   GEOMETRY AND TIME OF OCCULTATION FOR VARIOUS AZIMUTH ANGLES

A star lying in the orbital plane of the satellite will have refraction acting entirely in the orbital plane as the star is occulted by the earth. Only changes in elevation of the star due to refraction will appear as the star sets, and no change will occur in the direction perpendicular to the orbital plane due to refraction. (There can be lateral refraction but this effect, treated in Ref. 6 under non-sphericity, is so small that it will be neglected here). However, if the star is not in the orbital plane but has some azimuth angle with respect to the satellite, refraction will not occur in a plane coincident with the orbital plane. As a result, changes in elevation and azimuth will occur simultaneously during occultation, and the star will appear to trace out a curved path with respect to the earth. The geometry of occultation at an arbitrary azimuth angle is shown in Fig. 44, where

$$\underline{r} \quad = \quad \text{satellite radius vector}$$

$$\underline{s}^* \quad = \quad \text{unrefracted vector to the star}$$

$$\underline{s} \quad = \quad \text{refracted star vector}$$

$$\underline{\Omega} \quad = \quad \text{normal to the orbital plane}$$

$$R_s \quad = \quad \text{refraction angle}$$

$$AZ \quad = \quad \text{initial azimuth angle for unrefracted star}$$

$$\psi \quad = \quad \text{angle between x-axis and satellite radius vector}$$

$$\delta \quad = \quad \text{angle between satellite radius vector and unrefracted star vector}$$

Figure 44 shows the intersection of the following three planes:

(1)   The orbital plane;

(2)   The plane perpendicular to the orbital plane containing the orbital plane normal $\underline{\Omega}$, and unrefracted star vector $\underline{s}^*$;

(3)   The plane formed by the satellite radius vector, $\underline{r}$, and unrefracted star vector $\underline{s}^*$.

The intersection of planes (1) and (2) form the x-axis. The normal to the orbital plane at the satellite is the z axis, whereas the y axis is formed by $\underline{z} \times \underline{x}$. Planes (1) and (2) remain fixed for a particular star, whereas plane
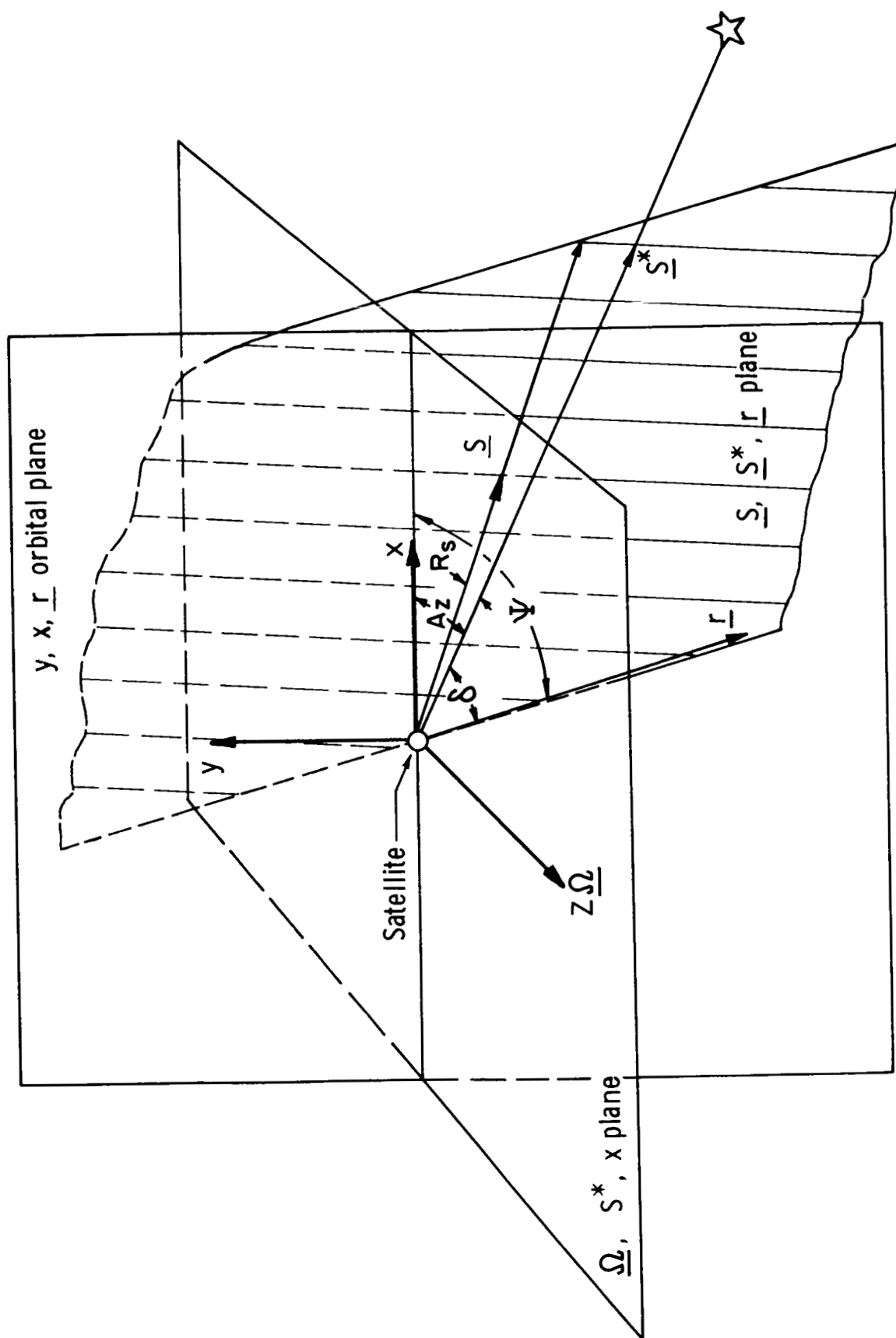
89

Fig. 44. Geometry of occultation for a given satellite azimuth angle.

(3) rotates in a nonlinear manner around $\underline{s}*$ as an axis as the satellite radius vector, $\underline{r}$, moves in its orbit during occultation. Refraction will occur entirely in plane (3).

In order to measure changes in elevation and azimuth angles, it was necessary to calculate the x, y, and z components of the orbital position and relate these components to the tangent ray height, refraction angle, and the other parameters used in the analysis of an isothermal atmosphere.

The refraction and component projections in plane (3) are shown in Fig. 45. The unit refracted star vector projected along the satellite radius vector is

$$\underline{s}_r = \underline{s} \ (\text{Sin } R_s / \sin \delta) \ , \tag{83}$$

$$\text{where} \ \ |\underline{s}| \ = 1 \ .$$

The refracted star vector projected along the unrefracted star vector $\underline{s}*$ is

$$\underline{s}_s = \underline{s} \ (\cos R_s + \sin R_s \cot \delta) \ . \tag{84}$$

These vectors give x, y, z components of $\underline{s}$ as

$$s_x = \underline{s} \ \left\{ (\cos R_s + \sin R_s \cot \delta) \cos AZ - \frac{\sin R_s}{\sin \delta} \cos \psi \right\} \ ; \tag{85}$$

$$s_y = \underline{s} \ (\sin R_s \sin \psi / \sin \delta) \ ; \tag{86}$$

$$s_z = \underline{s} \ \left\{ (\cos R_s + \sin R_s \cot \delta) \sin AZ \right\} \tag{87}$$

The variable azimuth and elevation angles with respect to the x, y, z coordinate system are

$$A = \cos^{-1} \left(\frac{s_x}{\sqrt{s_x^2 + s_z^2}} \right) ; \tag{88}$$
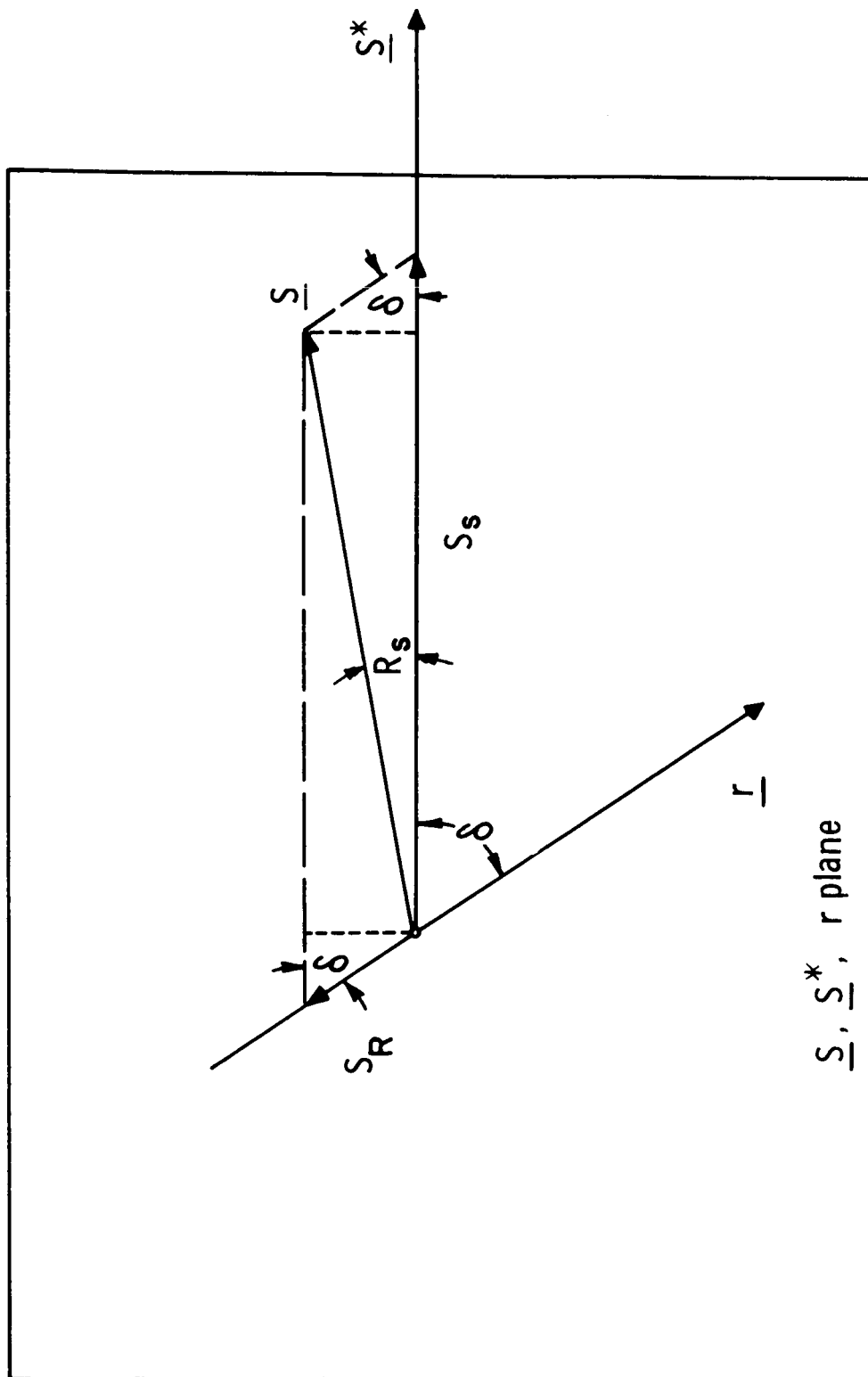
$$E = \cos^{-1} (s_y) \ . \tag{89}$$

91

Fig. 45. Refraction occurring in the $\underline{S}$, $\underline{S}^*$, $\underline{r}$ plane and the projection of the refraction vector on the $\underline{r}$ and $\underline{S}^*$ coordinates.

The angle ψ is related to Θ and AZ by

$$\psi = \cos^{-1}\left\{\frac{\cos \delta}{\cos AZ}\right\} \ .$$

(90)

From Section III A, Eq. (3) for an isothermal atmosphere, the refraction angle can be expressed as

$$R_S = 2k_0\rho_b \ e^{-h_0/H} \sqrt{\frac{\pi(r_e+h_0)}{2H}} \ ,$$

(3)

where

ρ_b = ground level density

h_0 = tangent ray height

H = scale height

r_e = radius of the earth

k_0 = $(221.05 + 1.66/\lambda^2) \times 10^{-6}$

λ = wavelength in microns

The angle δ can be expressed as

$$\delta = \sin^{-1}\left[\frac{(r_e+h_0)(k_0\rho_0+1)}{r_s}\right] - R_S \ .$$

(91)

Since $\delta = \frac{\pi}{2} - \Theta$, Θ is obtained from Section III A, Eq. (5) and expressed as

$$\Theta = \frac{\pi}{2} + R_S - \sin^{-1}\left[\frac{(r_e+h_0)(k_0\rho_0+1)}{r_s}\right] \ ,$$

(5)

where r_s = orbital radius of the satellite (km); $\rho_0 = \rho_b e^{-h_0/H}$.

   The time for occultation can be determined by taking the difference of the angle, ψ, between a given tangent ray height and a tangent ray height corresponding to occultation, in this case 5 km, and dividing it by the orbital frequency ω:

93

$$t(h) - t(h_o) = \frac{\psi(h) - \psi(h_o)}{\omega} \tag{92}$$

The change in elevation and change in azimuth angle are plotted in Fig. 46 for various azimuth angles during occultation. The changes are very close to being linear up to an azimuth angle of 30°. As an example, for a star having an unrefracted azimuth of 30° a change in azimuth angle of 19.5 arc-min occurs in going from a tangent ray height of 40 km to 5 km and the corresponding change in elevation is 51.5 arc-min.

The time required to pass between various tangent ray heights at any given azimuth angle is shown in Fig. 47. Occultation will be assumed to occur at 5 km, and the time required for occultation from any tangent ray height and any azimuth angle is given. Therefore, in the example occultation occurs in 31 seconds when the tangent ray height is 40 km.
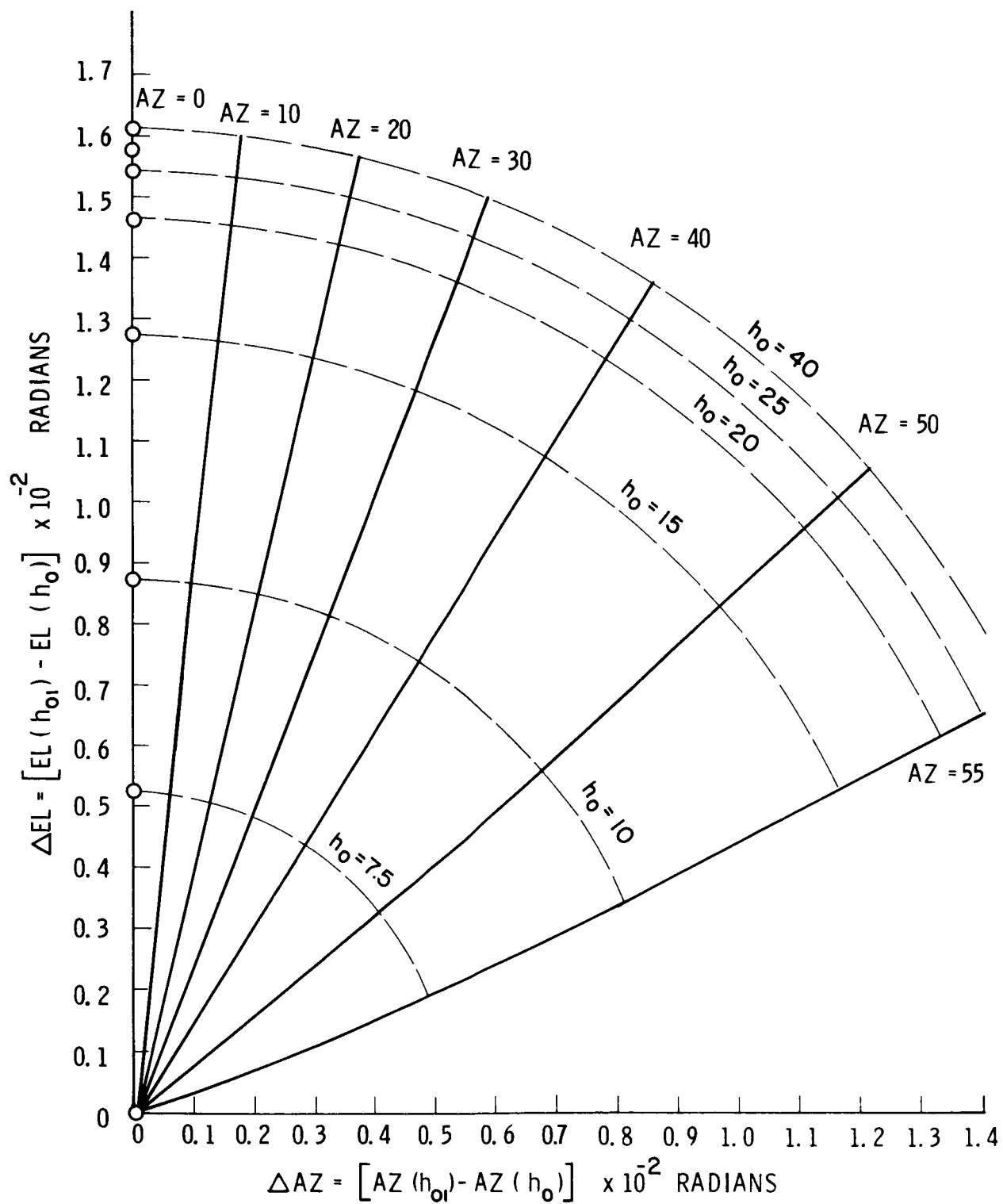
Fig. 46. Change in azimuth and elevation angles of a star tracker during occultation of stars at various azimuth angles.
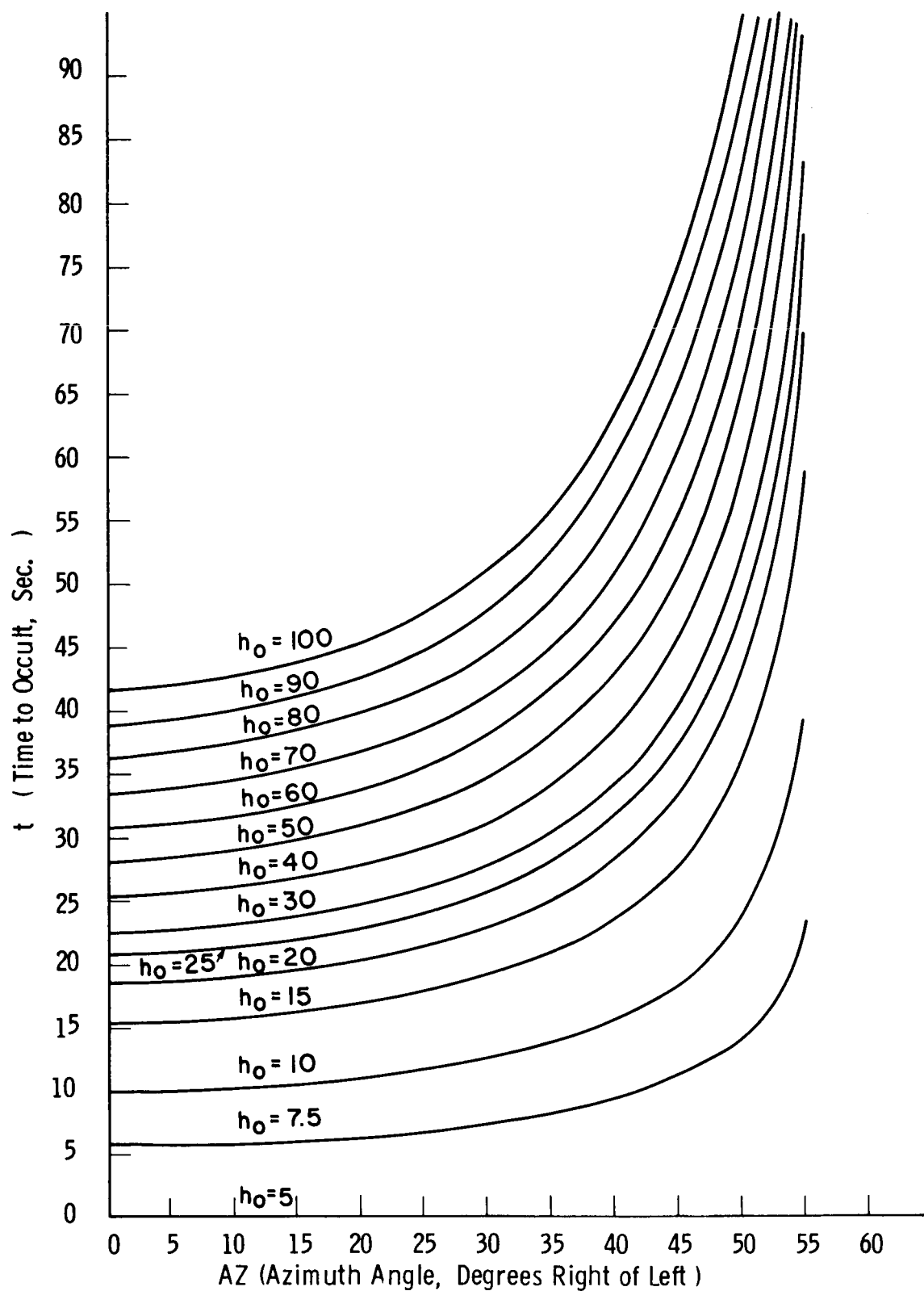
Fig. 47. Time to occult as a function of azimuth angle and tangent ray height.

96

VI. VERTICAL DISTRIBUTION OF CLOUD COVER AT LOW LATITUDES

Although estimates of regional and global cloud cover have been made from ground observations by Landsberg[12], from TIROS satellite photographs by Arking[3] and Clapp[4], and from TIROS longwave radiation data by Rasool[14] little information on the vertical distribution of regional cloud cover has been published. The scarcity of such climatic data may be attributed to the difficulty of observing the heights, and sometimes the presence, of high or multilayered clouds from the ground or from a ship. Commerical airline crews, however, enjoy a more favorable vantage point for obtaining such information. Therefore, cloud data recorded during trips between certain low-latitude terminals were utilized to arrive at an estimate of the vertical distribution of clouds above 4 km.

The data were made available by Pan American-Grace Airways, Inc., commerical carriers operating with jet turbine aircraft in South America. The routes were roughly meridional with terminals at Panama ($8°27'N$, $79°03'W$) at the northern end and Santiago ($33°26'S$, $70°40'W$) or Buenos Aires ($34°20'S$, $58°30'W$) at the southern end (Fig. 48). Cloud type and cloud altitude information had been entered on the flight forms for a considerable number of sectors of various lengths, so that the division of routes into segments of 5 to 10 degrees of latitude was both feasible and economical for data-handling. With one flight or more per day in each direction, and with three-quarters of the observations being acceptable over the period from August 1960 to May 1962, about 500 daytime observations per sector resulted in most cases. Night observations were less abundant, but they were also analyzed for comparison with day observations.

Since the obstruction to horizontal vision above 4-km altitude was the chief datum being sought, the method of processing used simple "Yes" or "No" answers to the questions, "Are clouds reported in this segment above 4, 5, ...12 km?" An affirmation of cloudiness in any sector of a segment was sufficient to count that segment among the positive cases. This counting procedure led to the cumulative frequency form of graphical representation, with altitude as the related variable (Fig. 49). Here the five curves are numbered according to latitudinal zones along the air routes at $8°N-0°$, $0°-10°S$, $10°S-20°S$, $20°S-30°S$, and $30°S-35°S$, with all daytime data included. The mean tropopause altitude was taken as an upper limit in each zone. The curves show a pronounced decrease in cloudiness southward at all altitudes above 4 km, except in the zone $20°S-30°S$, which is nearly identical to the ten-degree band on its northern side. A second interesting characteristic of the curves is the pronounced hump near 10 km in most cases. This apparent maximum in cloud frequency will be discussed in the section on systematic errors.

Monthly graphs similar to Fig. 49 were drawn in order to determine some suitable seasonal groups. The resulting combinations of months are used in Fig. 50 to show the seasonal variations in relation to latitude and altitude.
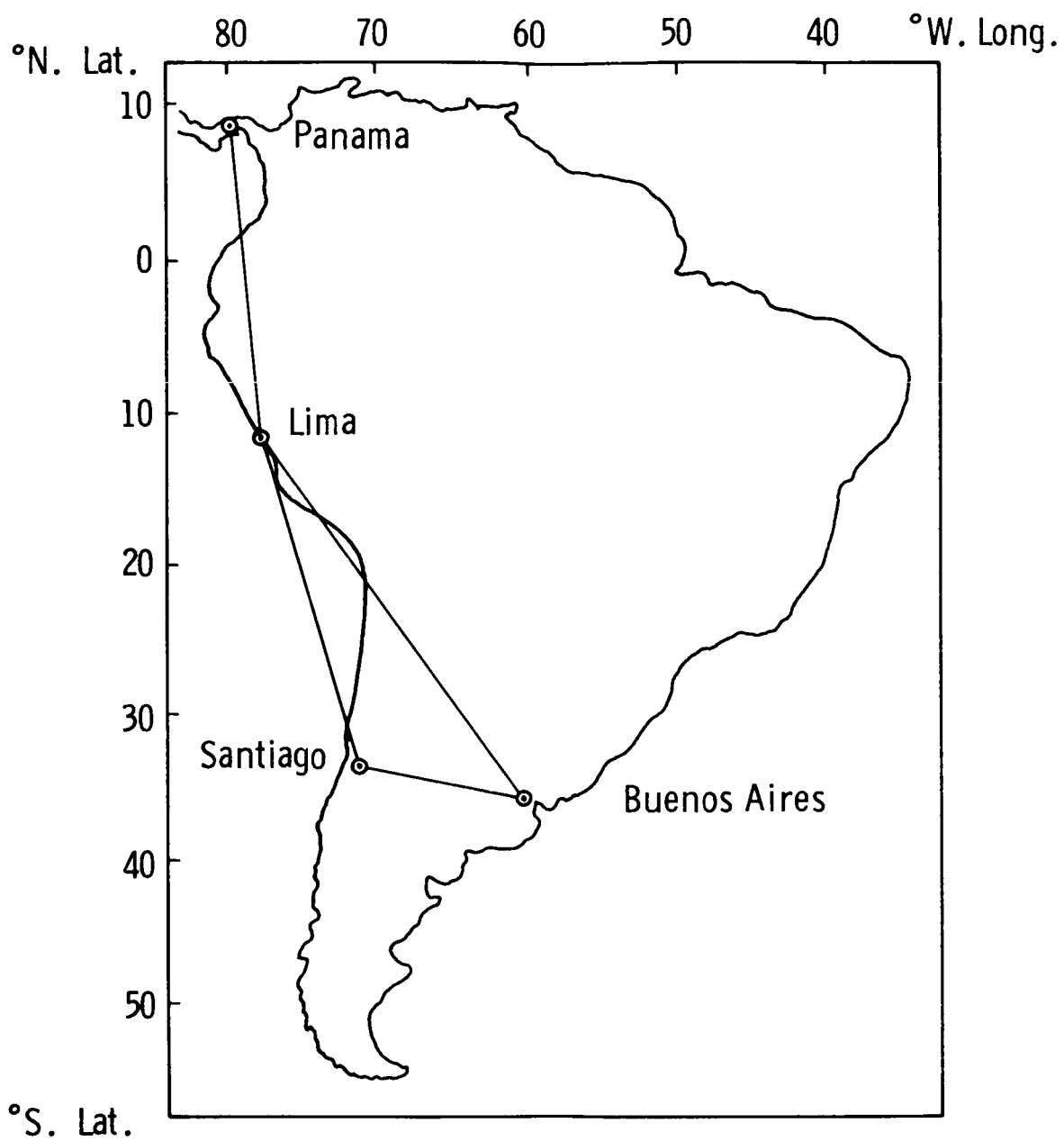
Fig. 48. South American airline routes for which cloud type and cloud altitude data were available.
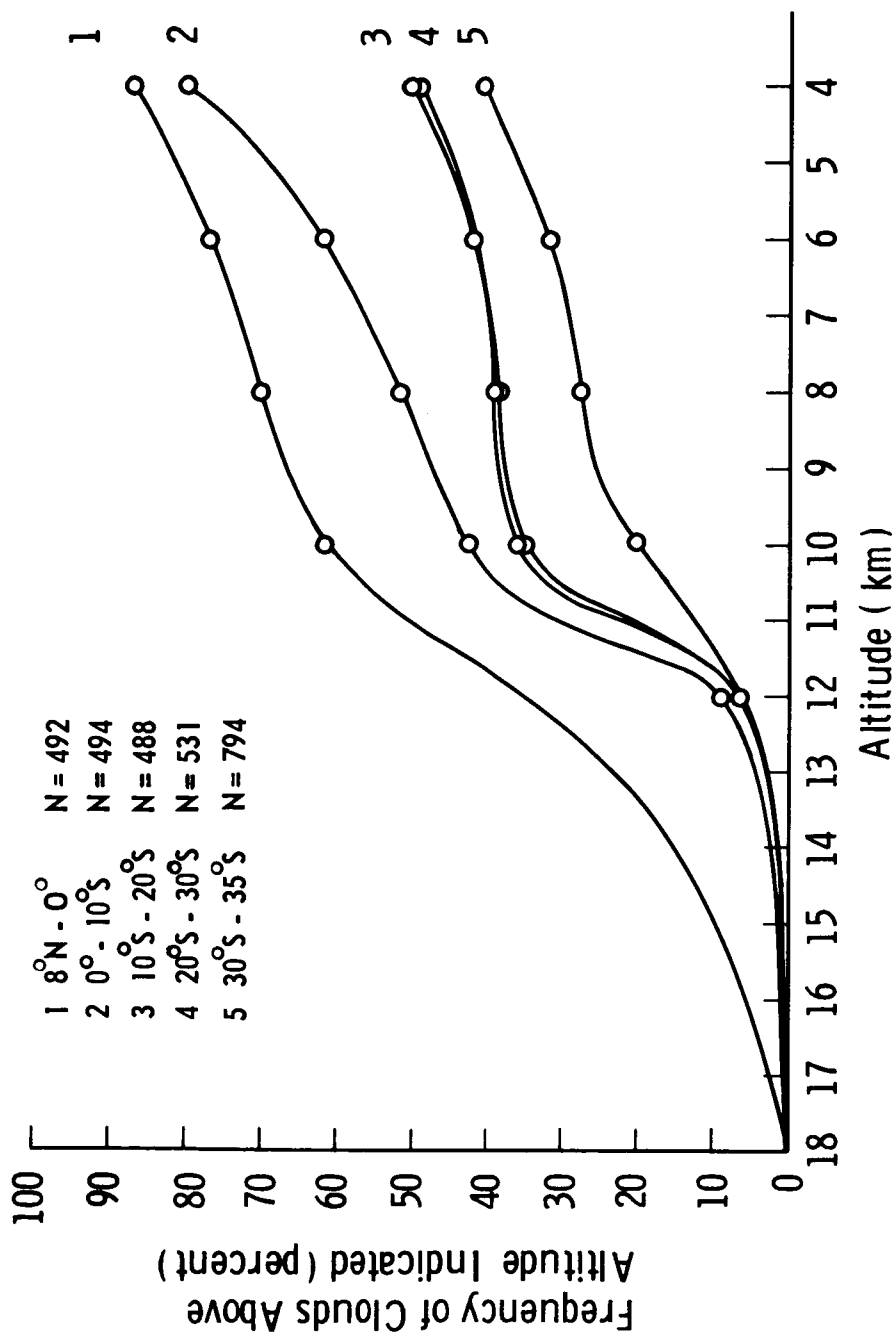
Fig. 49. Vertical distribution of cloud observations for the latitudinal zones indicated. The number of reports taken in daylight is shown by "N."
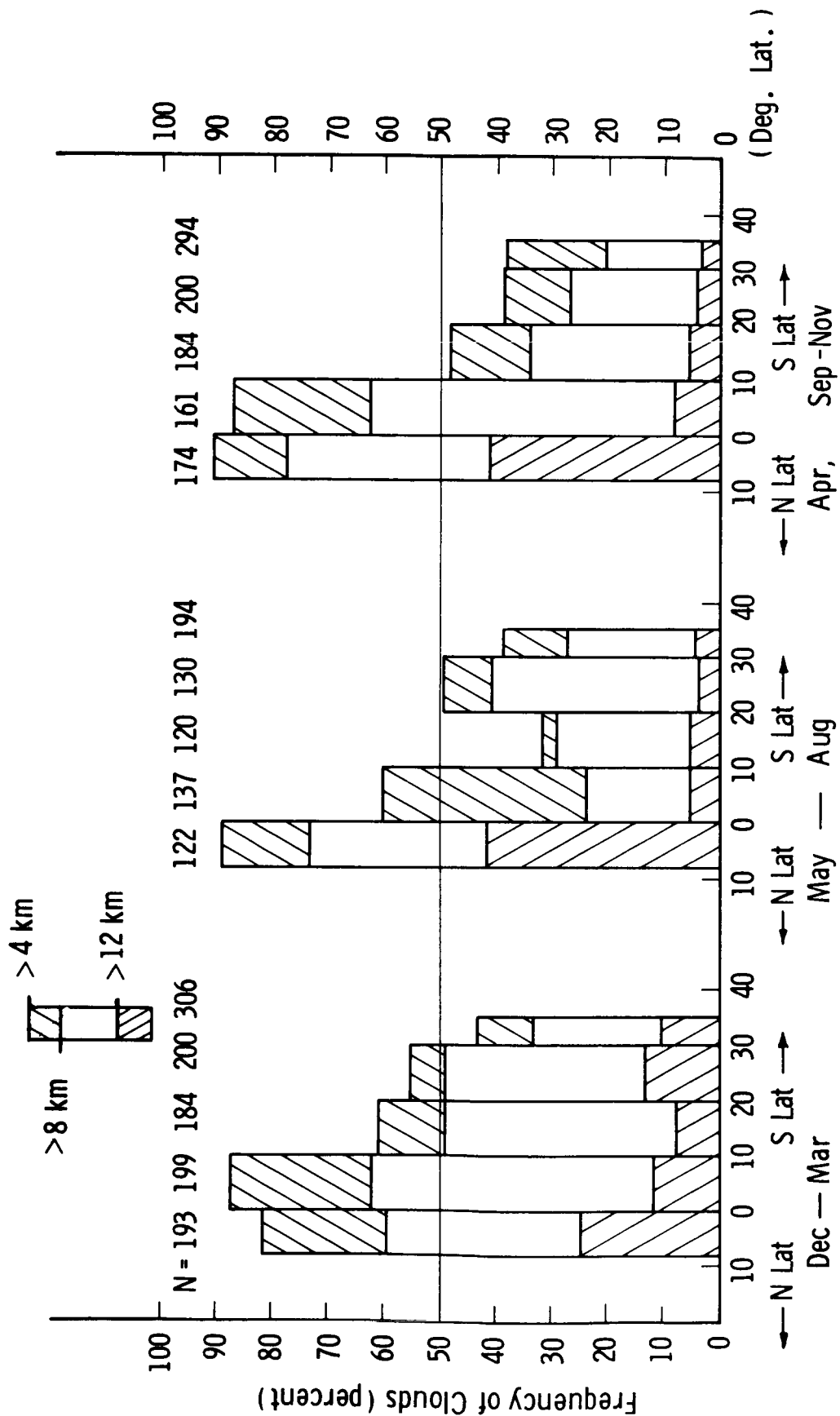
Fig. 50. Seasonal variation of reported cloudiness related to altitude and latitude zones.

The principal features of Fig. 50 are the are the dearth of cloud cover south of the equator above 12 km and the relative minima generally found in winter from $0°$ to $20°S$. Summer high-level cloudiness exceeds that of winter in all zones from $8°N$ to $35°S$, and the transition seasons are similar to summer near the equator. High frequencies around the equator are associated with the Inter-tropical Convergence Zone, which is frequently active within the $10°N$ - $0°$ belt throughout the year and occasionally in the $0°$ - $10°S$ zone in the December-March period. The 50-% line drawn across this graph corresponds to an altitude of about 10 km in equatorial latitudes much of the time, and a lesser altitude of 4 or 5 km at $15°S$ to $35°S$.

Possible systematic errors in visual observations of clouds may well raise some doubt about the graphical results presented here. For example, bias would be present in reports of nil cloudiness when no observation was actually made. Observer bias would also seem to explain the humps near 10 km in the curves of Fig. 49, since jet cruising levels are at 10 ± 2 km. This altitude is well below the tropopause barrier to clouds in these latitudes, so the result probably discloses a tendency to underestimate vertical distances from aircraft to clouds. No attempt was made to correct supposed underestimation bias.

Another systematic error in the data concerns the occasional absence of a written cloud report. Such missing data may well occur more frequently when clouds are absent, but if so, the rejection of blank reports would tend to counteract the erroneous reporting of nil cloudiness. Our procedure was to reject all blank or largely incomplete reports, which amounted to one-quarter of the total, and to rely in part upon several years of experience in the South American region.

No great amount of representativeness in these results is claimed for other longitudes, because the airline routes (Fig. 48) lie near the Andes Mountains, mostly on the lee side in the equatorial easterlies and the subtropical westerlies (Buenos Aires-Lima). The terrain effects may also cause some diurnal bias in the data due to the flight schedules: consistently a trip southbound from Panama started in the predawn twilight, and a trip northbound from Buenos Aires started during evening twilight. Each trip required 8-9 hours, including stops, to traverse all segments indicated in Fig. 48.

A number of night observations from the northbound trips were available south of $12°S$. These data were processed identically to the daytime data and they are presented for comparison in Fig. 51, where three of the nonseasonal curves in Fig. 49 are repeated. The frequency of observed cloud cover is lower at night in all segments by factors of 2 to 6 below 12 km. Since darkness makes accurate observation more difficult, some of this contrast should be attributed to systematic underestimation of cloud cover. In fact, the contrast between curves 3 and 5 over land is no greater than the contrast for the other segments, which are partly over water; and observer bias may be more important than nocturnal dissipation of clouds over land. As both effects act in the same direction, further conclusions will not be drawn from the comparison.
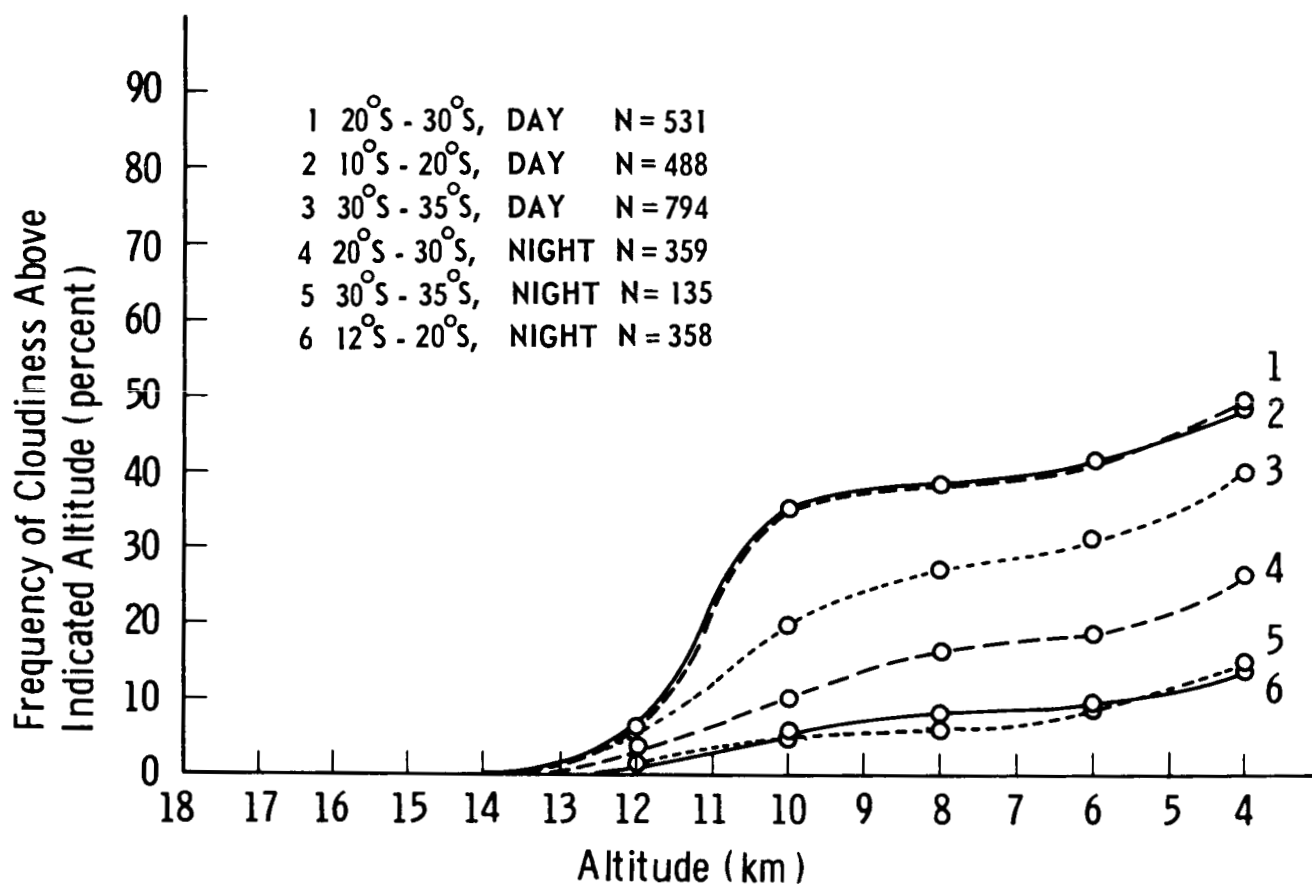
Fig. 51. Comparison of daytime and nighttime cloud frequencies over the latitudinal zones indicated. "N" is the number of cloud reports.

The following general statements summarize the principal results of this study which may be obtained regardless of systematic observational error:

a. The frequency of clouds above 4 km at 60-80°W. Long. decreases southward from 8°N to 35°S. With minor exceptions, this is true seasonally as well as in the mean condition.

b. Summer high-level cloudiness exceeds that of winter between 8°N and 35°S in these longitudes, but the transition seasons near the equator are comparable to summer.

c. Where nocturnal observations are available, as in the zone from 12°S to 35°S, the frequency of observed nighttime cloudiness is less than in daytime by factors of 2 to 6. An undetermined part of this difference is due to partial dissipation of cumuliform clouds in the hours of darkness over land areas.

The results of this preliminary work indicate that stars being tracked downward through the atmosphere will usually become obstructed by clouds within a 20-degree zone centered on the equator. The altitude at which this interruption of the grazing ray occurs will often lie between 10 km and 15 km, and little data will be obtained below 5 km. Beyond 10°S, however, the incidence of high clouds decreases greatly, and the chance of obtaining information from as low as 10 km is well over 50-50 in all seasons.

The kind of information obtained in the South American region should be supplemented by information obtained from airlines operating in other regions. To secure these data, a special pilot report form has been designed and put to use in the eastern Pacific region.

VII. CONCLUSIONS

The requirements of a satellite star-tracker have been fairly well established by the analyses presented in this report. Using the proposed signal-to-noise ratios and tracking accuracy requirements, the preliminary design of the star-tracking equipment is being undertaken.

The ability to design a suitable star-tracking system utilizing presently available equipment and techniques will prove the feasibility of the refraction method. Present information on engineering systems leads us to feel optimistic about the prospects of so doing.

Following this design, an orderly and economical plan will be proposed for implementing the method with hardware, culminating with an orbital test.

REFERENCES

1. Allen, C. W., *Astrophysical Quantities*, Second Edition, University of London, The Athlone Press, p. 192, 1963.

2. Altshuler, T. L., Document No. 615D199, General Electric M.S.V.D., Philadelphia, Pa., Fig. 18, December 1961.

3. Arking, A., The latitudinal distribution of cloud cover from TIROS photographs, *Science*, 143, 569-572, February 1964.

4. Clapp. Philip F., Global cloud cover for seasons using TIROS nephanalysis, *Monthly Weather Review*, 92, 495-507, November 1964.

5. Elvey, C. T., and Roach, F. E., *Astrophysical Journal*, 85, 231, 1937.

6. Fischbach, F. F. et al., *Atmospheric Sounding by Satellite Measurements of Stellar Refraction*, The University of Michigan ORA Report 04963-2-T, December 1962.

7. Gillett, F. C., Huch, W. F., Ney, E. P., and Cooper, Gordon, Photographic observations of the airglow layer, *Journal of Geophysical Research*, 69, 2867, July 1, 1964.

8. Hays, P. B., and Fischbach, F. F., *Analytic Solution for Atmospheric Density from Satellite Measurements of Stellar Refraction*, The University of Michigan ORA Report 04963-3-T, January 1963.

9. Jones, L. S., Fischbach, F. F., and Peterson, J. W., *Atmospheric Measurements from Satellite Observations of Stellar Refraction*, The University of Michigan ORA Report 04963-1-T, January 1962.

10. Kallmann-Bijl, H., Boyd, R. L., Lagow, H., Poloshov, S. M., and Priester, W., *Cospar International Reference Atmosphere*, CIRA 1961, North-Holland Publishing Company, Amsterdam, 1961.

11. Koomen, M. J., Gulledge, Irene S., Packer, D. M., and Tousey, R., Night airglow observations from orbiting spacecraft compared with measurements from rockets, *Science*, 140, 1087, 7 June 1963.

12. Landsberg, H., Climatology, Section XII, 928-997, in *Handbook of Meteorology*, F. A. Berry, Jr., E. Bollay, and N. R. Beers, McGraw-Hill Book Company, Inc., New York, 1068 pp., 1945.

13. Ramsey, R. C., Spectral irradiance from stars and planets, above the atmosphere, from 0.1 to 100.0 microns, *Applied Optics*, 1, July, 1964.

14. Rasool, S. I., Cloud heights and nighttime cloud cover from TIROS radiation data, *Journal of the Atmospheric Sciences*, 21, 152-156, March 1964.

15. Roach, F. E., and Megill, L. R., Integrated starlight over the sky, *Astrophysical Journal*, 133, 228-242, 1961.